SYNTHESIS AND CHARACTERIZATION OF CERAMIC OXIDE IONIC CONDUCTORS FOR SOLID OXIDE FUEL CELL APPLICATION

Thesis submitted to

THE UNIVERSITY OF KERALA

for the degree of

DOCTOR OF PHILOSOPHY IN PHYSICS

under the

FACULTY OF SCIENCE

by

VAISAKHAN THAMPI D S

NATIONAL INSTITUTE FOR INTERDISCIPLINARY SCIENCE AND TECHNOLOGY (NIIST)

COUNCIL OF SCIENTIFIC AND INDUSTRIAL RESEARCH (CSIR)

THIRUVANANTHAPURAM-695 019

KERALA, INDIA

2016

DECLARATION

I hereby declare that the Ph.D. thesis entitled **"Synthesis and Characterization of Ceramic Oxide Ionic Conductors for Solid Oxide Fuel Cell Application"** is an independent work carried out by me at the Materials Science and Technology Division, National Institute for Interdisciplinary Science and Technology (NIIST-CSIR), Thiruvananthapuram, under the supervision of **Dr. P. Prabhakar Rao** and it has not been submitted anywhere else for any other degree, diploma or title.

Vaisakhan Thampi D. S.

Thiruvananthapuram
February, 2016

NATIONAL INSTITUTE FOR INTERDISCIPLINARY SCIENCE AND TECHNOLOGY (NIIST)

Council of Scientific & Industrial Research
(Formerly Regional Research Laboratory)
Industrial Estate P.O., Trivandrum - 695 019
Kerala, INDIA

ISO 9001 REGISTERED
DNV
MGMT. SYS.
RvA C 024
DNV Certification B.V., The Netherlands

Dr. P. Prabhakar Rao
Chief Scientist & Head
Materials Science and Technology Division

Tel: 91-471-2515 311
E-mail: padala_rao@yahoo.com

CERTIFICATE

This is to certify that the work embodied in the thesis entitled "**Synthesis and Characterization of Ceramic Oxide Ionic Conductors for Solid Oxide Fuel Cell Application**" has been carried out by Mr. Vaisakhan Thampi D. S. under my supervision at the Materials Science and Technology Division of National Institute for Interdisciplinary Science and Technology (NIIST-CSIR), Thiruvananthapuram and the same has not been submitted elsewhere for any other degree.

Dr. P. Prabhakar Rao
(Thesis supervisor)

Thiruvananthapuram
February, 2016

ACKNOWLEDGEMENTS

Although mine is the only name that appears on the cover page, the contents and the feasibility of this thesis have significant contributions from a great many people. I always had a passion for science and wanted to be part of how it is being done, at least once in my life. That was a pristine experience indeed; recognizing a problem, tackling it, trying to solve it and adding something new to the existing knowledgebase. Of course there were challenges, and that is what makes up research. Now when I am consolidating my PhD research as a dissertation here, I owe my gratitude to all those people who have made this possible.

Most of all I want to thank my research supervisor, Dr. P. Prabhakar Rao, who was kind enough to accept me as one of his students. Being a sincere person dedicated very much to doing good science, he gave me immense freedom to explore the subject on my own. His keen observations and challenging arguments helped me a lot in refining my ideas, and discussions with him gave me a lot more insights.

The first person to welcome me to my institute was late Dr. Peter Koshy, former head of the section, who was crucial in giving a very good first-impression about my research environment, which boosted my confidence. I recollect his memories in this context with gratitude.

I must thank Dr. Ajayaghosh, Director, and Dr. Suresh Das, former Director, NIIST-CSIR, for facilitating my research work and for the appreciation they have shown to me.

The former heads of the Materials Science and Technology Division, Dr. K. G. K. Warrier, Dr. M. T. Sebastian and Dr. M. L. P. Reddy were always supportive and I use this occasion to express my gratitude for the same.

I'm thankful to Dr. V. K. Vaidyan who led the annual assessment of my research, for his comments that helped a lot in its improvement.

Mr. M. R. Chandran and Mrs. Lucy Paul were very helpful in carrying out the scanning electron microscopy studies. I am grateful to them for the same and also for the warm personal relationship they shared with me.

I sincerely acknowledge the help given by Mr. Kiran Mohan and Mr. C. K. Chandrakanth in electron microscopic analysis of my samples.

I am grateful to all the former and present colleagues in my section, especially, Mr. M. R. Nair and Mr. V. Sreekantan for their support. I also remember with gratitude, my fellow students including Dr. Sibi K. S., Dr. Deepa M., Dr. Sandhya Kumari, Dr. Radhakrishnan A. N., Dr. Mariyam Thomas, Mr. Mahesh S. K., Mrs. Sumi S., Mrs. Sameera S., Mrs. Reshmi V. R., Dr. Linda Francis, Mrs. Divya S., Ms. Sreena T. S., Ms. Athra K V Raj, Mrs. Soumya, Ms. Suchithra, Ms. Renju, Ms. Ajuthara, Ms. Aswathy, Mr. Pruthiviraj, Mr. Shanoj and Ms. Haritha, for making the environment active and vibrant. They have always helped me, either by softening the challenges or by making me stronger to face them.

My sincere gratitude also goes to Sree Chitra Tirunal Institute for Medical Sciences & Technology and Department of Optoelectronics- University of Kerala for extending the Raman spectroscopy facility to my research.

I use this occasion to acknowledge the financial assistance in the form of Junior and Senior Research Fellowships provided to me by the University Grants Commission (UGC) and instrumentation facilities provided by Council of Scientific and Industrial Research (CSIR).

Formalities aside, there are people who have played key roles in my completing this research work. They stood by me, showed no inhibition in running

to me whenever I was in need, and in some way or other became a reason for the very existence of this thesis. Words will not be enough to express my indebtedness to them and I feel naming them in a formal way will be inappropriate.

My family gave me full freedom to pursue the career I liked. Never had I heard a voice from them which said I should not go in a direction I chose. This dissertation will not have been possible without them. I am deeply thankful to my family, including my parents, sister and especially my best friend and wife, Lekshmi.

–Vaisakhan Thampi

CONTENTS

List of Tables

List of Figures

List of Abbreviations

AFC	Alkaline Fuel Cell
DMFC	Direct Methanol Fuel Cell
EIS	Electrochemical Impedance Spectroscopy
FCC	Face Centred Cubic
FT	Fourier Transform
FWHM	Full Width at Half Maximum
GDC	Gadolinium Doped Ceria
HRTEM	High Resolution Transmission Electron Microscope
ICDD	International Centre for Diffraction Data
IS	Impedance Spectroscopy
IT-SOFC	Intermediate Temperature Solid Oxide Fuel Cell
LAMOX	$La_2Mo_2O_9$ based oxides
LSGM	Lanthanum Strontium Gallium Manganite
LSM	Lanthanum Strontium Manganite
MCFC	Molten Carbonate Fuel Cell
NASA	National Aeronautics and Space Administration
PAFC	Phosphoric Acid Fuel Cell
PEMFC	Proton Exchange Membrane Fuel Cell
RE	Rare Earth
SAED	Selected Area Electron Diffraction
SEM	Scanning Electron Microscope
SOFC	Solid Oxide Fuel Cells
ScSZ	Scandia Stabilized Zirconia
TEC	Thermal Expansion Coefficient
TEM	Transmission Electron Microscope
TMA	Thermo Mechanical Analysis
XRD	X–Ray Diffraction
YSZ	Yttria Stabilized Zirconia

PREFACE

Solid Oxide Fuel Cell (SOFC) is an electrochemical device showing promise as an efficient non-conventional energy resource. Of the four fundamental parts of an SOFC *viz* electrolyte, cathode, anode and interconnects, nature of the electrolyte is very important. In addition to being chemically and thermally stable, the electrolyte must have high oxygen-ion conductivity and it forms the heart of an SOFC. Development of efficient electrolytes that show good conductivity at lower operating temperatures is gaining much attention these days. The characteristics of solid electrolytes depend on various factors such as crystal structure, composition, nature of constituent atoms *etc.* and hence they are very important from a research perspective.

The present research work focuses on understanding the correlations between various structural features and the electrical properties of some potential electrolyte materials. The first chapter gives an introductory note on solid oxide fuel cells in general and specifically highlights the importance of electrolyte. An account of the currently used electrolyte materials along with the challenges in material selection is also included.

In chapter-2, an investigation on the effect of cation substitution on a fluorite-type material with a stoichiometry of $(1-x)Gd_2Zr_2O_7$-$xCaZrO_3$ is discussed. The aliovalent substitution of Gd^{3+} by Ca^{2+} allowed creation of more oxygen vacancies in the lattice of these compositions. This resulted into a progressive decrease in lattice parameter and an increase in thermal expansion coefficient. The induced oxygen vacancies provided a lower energy barrier for ionic diffusion and hence led to an increase in conductivity.

Chapter-3 discusses a contrast between independent substitutions by two cations in $Gd_2(Zr_{1-x}M_x)O_{7-\delta}$ (M= Sc and Y; x = 0, 0.1, 0.2, 0.3, 0.4) system.

Despite being in the same group of elements, the two substituent cations differed in their influence on the parent lattice. Both aliovalent substitutions introduced oxygen vacancies. Larger ionic radius of Y^{3+} forced the lattice to expand which along with the increased anion defects lowered the energy barrier for charge transport. Whereas, in Sc-substituted compositions, oxygen vacancies dominated over ionic size causing the lattice to contract and their cooperative behavior turned out to be disadvantageous for long range conduction process. The changes in rigidity of the inter-ionic bonds and the lattice volume introduced by the substituent cations also influenced the thermal expansion behavior of the materials.

Influence of Ce-substitution on the structural and electrical properties of $Sm_2Zr_{2-x}Ce_xO_7$ (x= 0, 0.1, 0.2, 0.3, 0.4, 0.5) system is analyzed in Chapter-4. Addition of Ce ions into the $Sm_2Zr_2O_7$ lattice induced structural disorder to both cationic and anionic sublattices, gradually transforming the unit cell from an ordered pyrochlore to a defect fluorite structure. Substitution of bigger Ce ions to the Zr sites leads to an increase in lattice parameter and a decrease in thermal expansion coefficient of the material. The ionic disorder led to decreased energy barrier for the thermally activated conduction process thereby increasing the overall conductivity of the materials. Beyond x = 0.4, the ion-ion interaction in the disordered lattice began to dominate, leading to increased activation energy and decreased total conductivity. The results demonstrate that the thermal expansion of these oxides is predominantly influenced by the B – O bond energy than the Madelung binding energy.

In chapter-5, simultaneous substitution by two cations and its effects on the structure and electrical properties of a pyrochlore-type composition, $(Sm,Zr)_{2-x}(Sc,Ce)_xO_7$ is discussed. The substitution leads to a contraction of lattice,

simultaneously accompanied by a structural disorder from pyrochlore to defect fluorite structure. Disorder enhanced the conductivity to a certain extent and beyond that the lattice contraction increased the cooperative behavior among the ions leading to decreased conductivity. Thermal expansion also decreased with substitution.

The 6th chapter briefs the relevant conclusions that can be drawn from the overall analysis of the present research work. The future scope, including attempts for further improvement in properties and more characterizations for throwing light to further physical parameters, is also discussed in this chapter.

CHAPTER 1

****

Energy Materials and Solid Oxide Electrolytes

****

This chapter introduces solid oxide fuel cells as a promising candidate for renewable energy production from the viewpoint of materials science. Basic principle of operation, various physical components, their respective material requirements and the challenges in materialization are discussed. While highlighting the importance of solid oxide electrolytes, which is the focus of this thesis, a brief review of the current research scenario in this topic is also presented. Special emphasis is on pyrochlore/fluorite type materials and their crystal structure and electrical properties are discussed.

1.1. Introduction

Energy is what drives our civilization. Tremendous population growth and industrial revolution has triggered a surge in the global energy demand in recent decades. This in turn, has driven significant amount of research in fundamental and applied science towards developing new and efficient renewable resources of energy. Most of the renewable energy resources are utilized for electricity generation in addition to transportation, air and water cooling/heating etc. Reports say that they contributed more than 20% of the total electricity generation during the last years [IEA 2011]. This points towards the fact that research and development in this direction requires constant attention from the scientific community. So much is under way and a new stream of research usually labelled 'energy materials' has already attained thrust.

We are surrounded by a myriad of materials, both natural and artificial, found in anything from kitchen utensils to spacecrafts. The intellectual origin of materials science dates back to the origin of human civilization itself. Despite being addressed with a relatively new name - 'materials science', it is one of the oldest forms of applied science. The phrases like 'Stone Age', 'Bronze Age', 'Iron Age' etc. used in connection with human prehistory are evident endorsements to this fact. The basis of materials science lies in understanding the structure of materials and applying that knowledge in tuning their properties and performance. Growing from traditional examples like metals and ceramics, the materials world has absorbed advanced candidates like semiconductors, superconductors, nanomaterials, biomaterials, etc.

'Energy materials' is a relatively newly coined term that covers materials that are to be used for energy conversion and storage applications. In a scenario where multiple geophysical and social pressures are demanding a shift from

conventional energy resources to renewable and sustainable ones, these materials are gaining more and more attention from engineers and researchers alike. For any green energy technology, whether it is photovoltaic solar energy harvesting, photocatalytic water splitting, fuel cells, hydrogen storage or energy storage, material performance lies in the heart of each of them. The present research work is focused on a class of materials that are potential candidates to be used as electrolytes in solid oxide fuel cells (SOFC), a promising technology for green energy generation. Basics of fuel cells, the importance of electrolyte in its operation, the mechanism and desirable characteristics for its optimum performance along with a general survey of the current research scenario in this field are discussed in this chapter.

1.2. Fuel Cells

A fuel cell, as the name suggests, is essentially an electrochemical cell that can be driven continuously to provide electrical energy through the supply of a fuel. It can be conceived as a cross between a battery, where direct conversion of chemical energy to electrical energy takes place, and a heat engine, which is a continuously fueled device. It is sometimes referred to as electrochemical engine [Brett *et al.* 2008]. Fuel cell is one of the oldest electrical energy conversion technologies whose conception and development dates back to the middle of the 19th century. The underlying principle was discovered by Prof. Christian Schönbein and the fuel cell as a technological invention was developed by one of his colleagues, Sir. William Grove [Carrette *et al.* 2001]. However, despite the attractive prospects fuel cells had to offer, a serious follow up to its invention was not taken up by the scientific community. It was obvious since the primary non-renewable energy resources were so abundant and cheap those days and the world had just witnessed an industrial revolution. By the beginning of 20th century, increased dependence on electricity warranted more research to be

invested in methods to convert chemical energy into electrical energy. Another important concern that popped up was the environmental consequences of the use of fossil fuels for generation of electricity and powering motor vehicle and industrial machineries. The first commercial application of fuel cells thus came a century after its invention when NASA started using them to power their space probes and satellites. Now they have been identified to help us reducing the dependence on fossil fuels thereby stopping to add hazardous by-products to the environment. They are being in use as primary and backup power sources in many industries, commercial establishments and apartments especially in areas far from the conventional power grids. There are fuel cell-powered automobiles, computers etc. already in market.

There are many types of fuel cells, all of them having an anode, a cathode and an electrolyte. The basic chemical process is the natural combination of fuel with oxygen, but by restricting the pathways of charge carrying species. The ions are always drawn through the electrolyte and the electrons are always driven between the electrodes through an external circuit which can be harvested as useful electricity. They are very similar to batteries in their operation, but unlike batteries they do not run down and will be working as far as there is supply of fuel and oxidant. The main difference between various types of fuel cells is the nature of electrolyte used. It allows the appropriate ions, and them alone, to pass between the electrodes. Most of the fuel cells use the chemical combination of hydrogen and oxygen which produces water as the reaction product and it highlights their environmental friendliness. It should also be noted that this is a chemical combination rather than combustion, which is free from the conventional Carnot limit, which help to achieve an appreciable efficiency. Apart from the high efficiency, low noise, low environmental impact, very good load

following capacity etc. are expected to revolutionize the power generation industry.

Fuel cells are classified according to the electrolytes they choose to employ. Alkaline Fuel Cells (AFC), Polymer Electrolyte Membrane Fuel Cells (PEMFC), Direct Methanol Fuel Cells (DMFC), Phosphoric Acid Fuel Cells (PAFC) etc. are generally called low-temperature fuel cells due to their lower operating temperatures, which are typically below 250 °C. Whereas, Solid Oxide Fuel Cells (SOFC) and Molten Carbonate Fuel Cells (MCFC) operate in a temperature range of 600–1000 °C and are considered to be high-temperature fuel cells. A list of major fuel cell types with their characteristic features is presented in Table 1-1 which is adapted with credits from literature. [Stambouli and Traversa 2002]

Table 1-1: Various types of fuel cells and their characteristics

Types of fuel cell	Electrolyte	Operating Temperature	Fuel	Oxidant	Efficiency
Alkaline (AFC)	Potassium hydroxide (KOH)	50–200 °C	Pure hydrogen, or hydrazine	O_2/Air	50–55%
Direct methanol (DMFC)	Polymer	60–200 °C	Liquid methanol	O_2/Air	40–55%
Phosphoric acid (PAFC)	Phosphoric acid	160–210 °C	Hydrogen from hydrocarbons	O_2/Air	40–50%
Sulfuric acid (SAFC)	Sulfuric acid	80–90 °C	Alcohol or impure hydrogen	O_2/Air	40–50%
Proton-exchange membrane (PEMFC)	Polymer, proton exchange membrane	50–80 °C	Less pure hydrogen from hydrocarbons or methanol	O_2/Air	40–50%
Molten carbonate(MCFC)	Molten salt such as nitrate, sulphate, carbonates	630–650 °C	Hydrogen, carbon monoxide, natural gas, propane, marine diesel	CO_2/O_2/Air	50–60%
Solid oxide (SOFC)	Ceramic as stabilised zirconia and doped perovskite	600–1000 °C	Natural gas or propane	O_2/Air	45–60%
Protonic ceramic (PCFC)	Thin membrane of barium cerium oxide	600–700 °C	Hydrocarbons	O_2/Air	45–60%

The discussions in this thesis mostly pertain to the material requirement of a solid oxide fuel cell which uses a hard solid oxide, mostly a ceramic, as its electrolyte.

1.3. Solid Oxide Fuel Cells

A solid oxide fuel cell (SOFC) is one of the most promising candidates among the various classes of fuel cell which are under research and development. It fundamentally sandwiches a hard ceramic electrolyte between two porous electrodes. Anode acts as the fuel electrode and cathode acts as the air (oxygen) electrode. SOFC operate at high temperatures, typically as high as 1000 °C. Oxygen is reduced to oxide ions at the cathode which then passes through the electrolyte to the anode and reacts with fuel.

The features which highlight SOFC among the various classes of fuel cells are many:

- High energy efficiency, i.e., fuel input to electrical output ratio
- Flexibility in the choice of fuels, including traditional hydrocarbon fuels
- Suitability of application in the distributed generation market.
- Low noise generation due to the absence of moving parts
- Economic feasibility of component selection due to absence of noble metals
- Easiness in electrolyte management, since corrosive and difficult-to-handle liquid electrolytes are absent.
- Extremely low emissions which reduce environmental impact
- Long life expectancy

[Stambouli and Traversa 2002]

From the materials standpoint, SOFC components are very demanding primarily due to their high operating temperatures. Solid electrolytes do not possess appreciable ionic conductivity at low temperatures and this necessitates the SOFC to be operated only at high temperature. However this is not as severe a disadvantage as it may seem to be. It helps to achieve good fuel-flexibility since this evolved heat can be used to internally reform the hydrocarbon fuels, which in low-temperature fuel cells is usually a complex and expensive additional task. Internal fuel reforming in fuel cells also help reduce emission levels of carbon monoxide which will be further oxidized to carbon dioxide. The high temperature also enhances electrocatalysis avoiding the use of precious metals. Another aspect is the cogeneration capability, where the additional heat is used in combined production of electricity, most probably, by driving a gas turbine. This obviously increases the overall efficiency of power production, stretching it to around 70–80%.

All the components used by SOFC are solid materials. Due to this the cells show excellent durability without much deterioration since solid materials exhibit low diffusion and reaction rates. This also eliminates issues like electrolyte loss maintenance, electrode corrosion etc. which are usually found in other fuel cells using liquid electrolytes.

1.3.1. Basic principle and operation

A solid oxide fuel cell works on the basis of very simple principles, and despite the engineering difficulties, the basic operation is also very simple. The schematic operational diagram of a single SOFC unit is shown in Figure 1-1.

A thin dense electrolyte (figure is not to scale) with good ionic conductivity and ideally zero electronic conductivity is sandwiched between

anode and cathode. Both electrodes are porous so as to allow the supply of gaseous reactants in the cell unit. Fuel, which is usually reformed hydrocarbon or hydrogen, is supplied to the anode side. An electromotive force is developed across the electrolyte due to the difference in chemical potential of oxygen between the cathode and the anode.

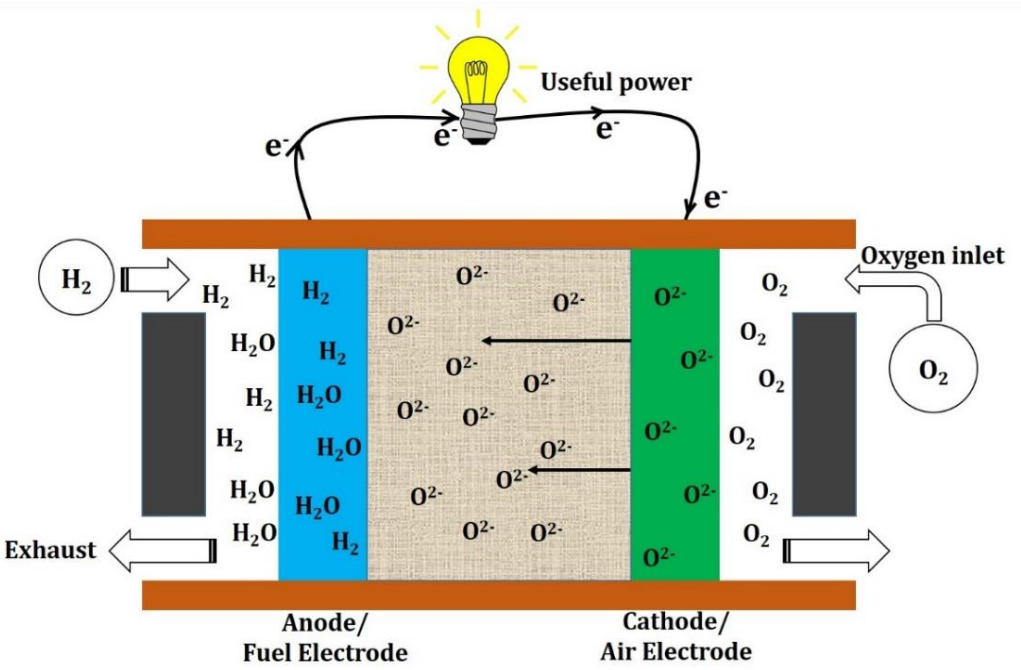

Figure 1-1: Schematic of a Solid Oxide Fuel Cell

At the cathode, the molecular oxygen is reduced to oxygen anions and then delivered to the electrolyte:

$$O_2(g) + 4e^- \rightarrow 2O^{2-} \qquad (1.1)$$

Whereas at anode, the oxygen ions are consumed by hydrogen at the electrolyte interface producing water and releasing electrons:

$$H_2(g) + O^{2-} \rightarrow H_2O\ (g) + 2e^- \qquad (1.2)$$

These electrons flow to the cathode through an external circuit, where from we extract the energy released as useful output power. The electrons will

be further used to reduce oxygen at the cathode. Ideally, the production of electrons is guided by potential given by Nernst equation:

$$E = E^0 + \left(\frac{RT}{2F}\right) \ln \left[\frac{P(H_{2\ anode}) P(O_{2\ cathode})^{1/2}}{P(H_2O_{anode})}\right] \quad (1.3)$$

Ideally, the open circuit voltage (E_{ocv}) of the fuel cell is given by the free energy change associated with the fuel oxidation reaction, given by $E_{ocv} = -\Delta G/nF$ (n = number of electrons transferred, F = Faraday constant). This value if we calculate for a general single cell would come around 1.1–1.2 V. But in practice, there will be dissipative reduction in this potential which will reduce the drive of current. Resistance of the electrolyte, potential losses in cathode and anode etc. are some of the factors that play to reduce the potential. However the dissipated energy invariably becomes heat and helps to maintain the cell at its high operating temperature. At present, SOFC units are rated at a voltage of ~0.7 V per cell.

1.3.2. SOFC design

As mentioned earlier, the voltage output of a single SOFC unit is too small for most practical applications. Hence they are always used in the form of stacks containing multiple units interconnected to give out workable electric power output. Although many different design concepts are there with varying geometry, power density *etc*., the two most common ones are (i) tubular design and (ii) planar design.

The tubular design, envisaged and popularized by Siemens-Westinghouse Company, has cell components deposited in the form of thin layers on the cathode tube. Typical dimensions of various tubes are: 15 – 20 mm in diameter, ~1.5 mm in wall thickness and 0.6 – 1 m in length [Badwal and Foger 1996]. This design has a self-sealing structure and the oxidant is injected through

a coaxial ceramic injector. This improves thermal stability and then removes the need for good thermal-resistant sealants. The tubular design itself is split into two variants, one where the gas flow is along the axis of the tube and other where the flow is perpendicular to the axis. Although tubular design is advantageous in many ways, lower power densities and expensive fabrication techniques are referred to as its major drawbacks.

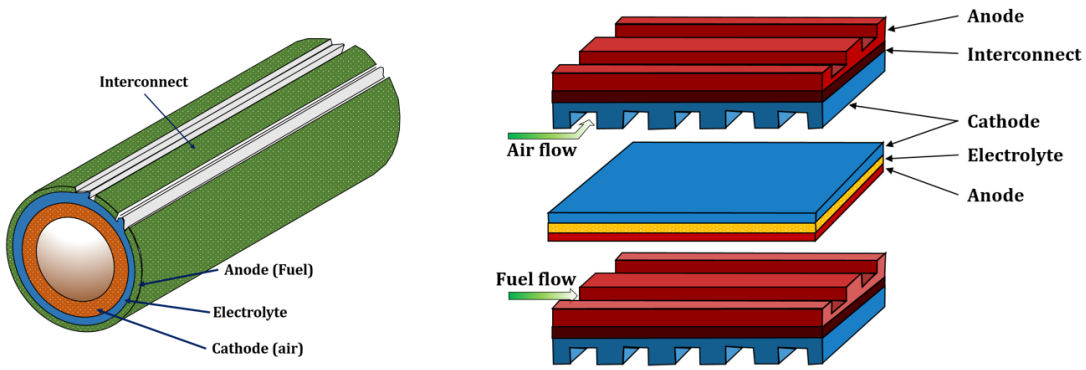

Figure 1-2: Common design concepts of an SOFC stack; tubular (left) and planar (right) designs

Planar design, or flat-plate design, is the most well-known among other fuel cell classes. Much more economical than tubular design, it is expected to possess the potential to deliver the cheapest SOFC unit. They have shorter current paths and are much more convenient than tubular design to be stacked together. Here the components are fabricated individually and stacked together and sealed with a high-temperature sealant. Electrode/electrolyte laminates are produced by deposition of electrodes onto sintered electrolytes and interconnector plates with gas channels are stable metal alloys with good thermal stability or ceramic materials. Several different variants of the planar design with different manufacturing techniques are available. This design has good power densities

and offers cheaper fabrication capability. Finding suitable sealant and interconnect materials are the major challenges in this case.

Other design concepts like monolithic design, mono block layer build concept etc. are currently under development.

1.3.3. Components and material requirements

Taking into account the nature and circumstances of operation of a solid oxide fuel cell, the selection of materials for various SOFC components poses severe demands [Minh 1993]. We have discussed, a fuel cell unit consists of two electrodes, an electrolyte and interconnect as the major structural components. Each of these serves specific function in the working of a fuel cell and therefore they should meet precise requirements. Structural, morphological, chemical and dimensional stabilities are a must for all of them since they are subjected to highly oxidizing and/or reducing environments. Proper conducting properties, whether it is ionic or electronic, and chemical compatibility with other components are also required. In order to avoid separation or cracking during operation or fabrication, the cell components should possess similar thermal expansion properties. Apart from all these high strength and toughness properties, fabricability, low cost etc. are also taken into consideration during materials selection. A component-specific overview of the materials requirements for various specific fuel cell components is briefed as following:

1.3.3.1. Electrolyte

Electrolyte is called the heart of a solid oxide fuel cell, and it has a major impact on the cell performance. The whole idea of SOFC is based on the concept of an oxygen ion conducting electrolyte through which the O^{2-} ions diffuse between the electrodes giving out the electrical voltage. The operating temperature of a fuel cell is decided by the nature of electrolyte we choose to

deploy. An ideal solid oxide electrolyte should possess high ionic conductivity (typically >1 × 10^{-3} Scm^{-1}) and no electronic conductivity [Brett*, et al.* 2008]. Apart from the chemical and thermal stability in high temperature operation, it should have closely matching thermal expansion coefficient with the electrodes and contacting components. To get high ionic diffusion and negligible reactant cross-over, it should possess a dense morphology. It is usually made as thin as possible to avoid ohmic losses within the electrolyte.

Since the present thesis is focusing on electrolyte materials and their physical characteristics, a more detailed discussion on the science and contemporary status of research in that area is required, which will be dealt with in forthcoming sections.

1.3.3.2. Anode

Anode is working in highly reducing atmosphere of the fuel flow. Moreover, it should be non-oxidized since the composition of the fuel changes during the operation of the cell. It should perform electro-oxidation of fuel catalyzing reaction and should have good electronic conductivity for efficient transport of electrons [Jiang and Chan 2004]. Metals can be utilized to this purpose. However, considering the operating condition and materials-cost, nickel is usually the common choice among the metals. Although cobalt, ruthenium *etc.* can also be used for the purpose, cost is a limiting factor for their use. Nickel is also an excellent electrocatalyst for the oxidation of hydrogen. In order to facilitate the gaseous supply of fuel, porosity is a requirement for anode materials which of course has to be maintained at high operating temperatures. This is generally done by dispersing nickel with the electrolyte material to form a cermet. This would avoid the sintering of nickel particles at high temperature thereby maintaining the porosity. Thermal expansion matching with the electrolyte material can also be achieved by this [Ormerod 2003]. This cermet

optimizes the three-phase boundary at which the ionic and electronic conducting phases in a fuel cell coexist [Brandon and Brett 2006]. Most commonly used cermet material is a composite of nickel and yttria-stabilized-zirconia. Since Ni has a tendency to promote carbon formation while using hydrocarbon fuels, there are researches oriented towards using ceramics instead of cermets as anode materials [Atkinson *et al.* 2004]. Certain perovskite-type materials are reported to be promising in this respect [Tao and Irvine 2003].

1.3.3.3. Cathode

The cathode operates in an oxidizing environment and, like anode, it should also possess good electronic conductivity and porous structure in addition to the stability requirements in high temperature. Reduction of molecular oxygen, ionic transport to the electrolyte, and managing the electrical current are the prime functions of cathode in the cell. Considering these requirements, noble metals or electronically conducting ceramic oxides are usually sought after for this purpose. But obviously noble metals are economically more demanding and are not preferred over the other. There are numerous oxide materials reported with promising properties [Lion and Worrell 1989]. Strontium doped lanthanum manganite (LSM, $La_{1-x}Sr_xMnO_3$) is the commonly used cathode material in zirconia based fuel cells. The electronic conductivity of $LaMnO_3$ is enhanced by doping with lower valent cations. Extent of doping dictates the electronic conductivity and also the thermal expansion coefficient. Certain perovskite-type materials have also been investigated for cathode applications [Juhl *et al.* 1996]. Much interest is now invested in lowering the operating temperature of SOFC and in that venture cathode may be the component that requires serious attention. At lower operating temperature, the polarization losses in the cell become appreciable due to the lowering of associated reaction kinetics. Composites involving typical cathode materials and electrolytes are expected to be a viable

method for developing effective intermediate temperature cathodes. Promising results in compositions like [(Sm,Sr)$CoCO_{3}$,(Ba,Sr)(Co,Fe)O_{3-d}], $La_{n+1}Ni_{n}O_{3n+1}$, ($GdBaCoO_{5+d}$) etc. are reported [Skinner 2001].

1.3.3.4. Interconnects

Interconnect has two important functions in a solid oxide fuel cell; to act as electrical contacts between two adjacent cell units and to properly distribute the gaseous reactants to their respective electrodes. One side of it will be a highly oxidizing environment whilst the other side will be a reducing one which raises serious chemical stability concerns for the selection of interconnect materials. It should be impermeable and must not react with cathode or anode at high temperature. For effective removal of heat from the electrodes, interconnects should possess high thermal conductivity. This is essential for homogenous temperature distribution within the fuel cell stacks. Apart from these, good mechanical strength, corrosion resistance, fabricability and low cost are essential requirements for a practical interconnect material. Ceramics, high-performance alloys and ferritic stainless steel are three main classes of materials used in this aspect. Doped $LaCrO_3$ is the most common ceramic candidate, typical dopants being Sr and Ca. For intermediate temperature fuel cells, ferritic steel components are good choices [Steele and Heinzel 2001]. Although metallic interconnects are comparatively cheaper, their applicability is limited in high temperature operations.

1.4. Solid Oxide Electrolytes

Electrolyte is perhaps the most important component in a fuel cell unit, which is sometimes even called the 'Heart of an SOFC' [Fergus 2006]. It is the selection of electrolyte that distinguishes a particular fuel cell from various kinds, and also the major element to decide the operating temperature.

A solid electrolyte is the conductor of a particular kind of ionic species, which is O^{2-} ions in the case of solid oxide fuel cells. They pass an ionic current inside the cell, which equals an electronic current that flows through an external circuit. The electromotive force that drives the external electronic current between the electrodes is created by chemical reactions that happen on different sides of the electrolyte. Obviously, electrolytes should have high ionic conductivity to reduce cell impedance and negligible electronic conductivity to prevent leakage currents. The compatibility with other cell components, especially with regard to chemical and thermal expansion properties, is also a crucial consideration. An electrolyte works in a very challenging environment: hydrogen or hydrocarbons on the anode side and oxygen on the cathode side, that too at high temperature. A major thrust in electrolyte research nowadays is in reducing the operating temperature to 600 °C – 800 °C which, despite the fuel flexibility, will relax certain stringent requirements in general material selection criteria in fuel cell fabrication [Massimiliano Lo Faro 2009]. Attaining high ionic conductivity at intermediate temperatures, for chemical systems with compatible physical characteristics with other fuel cell component materials is the major motive that is driving contemporary research in this area.

1.4.1. Conduction mechanism

Transport of one or more types of ions across the material is essential for ionic conductivity. In an ideal crystalline material, ions are arranged in perfectly regular pattern and are connected by interionic bonds. Due to this the ions cannot move freely within the bulk of the crystal, but can only vibrate about their fixed equilibrium positions. But in real crystals, which are at temperatures higher than absolute zero, some amount of defects will always be present. The degree of defects may differ from material to material, and for the same material may also differ from temperature to temperature. The ideal crystal arrangement at

absolute zero correspond to the minimum of potential energy. However with increase in temperature, the total thermodynamical free energy will begin to get contribution from the entropy term. In an effort to minimize the free energy, the system will try to increase entropy which will lead to creation of more defects in the lattice. The defects are mostly Schottky-type or Frenkel-type, which are collectively called point defects [West 1984]. Schottky defects are formed when a pair of oppositely charged ions go missing from the lattice, while Frenkel defects are characterized by a single ion moving to an interstitial site leaving its normal site vacant. Both of these lead to formation of vacancies in the lattice, and an ion in the immediate neighborhood can jump to occupy this vacant site. This hopping leaves a new vacancy, which can now host a new ion. This can act as a mechanism of ionic transport and is called vacancy migration. Similarly, interstitial migration can also act as an ionic transport mechanism [Kumar and Yashonath 2006].

A theoretical treatment of the ionic transport mechanism in ionic conductors was done by J. A. Kilner [Kilner 2000] wherein he throws light on the temperature dependence of conductivity. The relationship between ionic self-diffusion coefficient and ionic mobility is given by the Einstein relation,

$$\mu = \frac{qD}{kT} \tag{1.4}$$

where μ is the mobility, D is the self-diffusion coefficient, q is the charge, k is the Boltzmann constant and T is the absolute temperature. The random walk theory in 3D lattice gives an expression for self-diffusion coefficient,

$$D = \frac{z}{6} f(1-c) a_0^2 v_0 \exp\left\{-\frac{\Delta G_m}{kT}\right\} \tag{1.5}$$

Here, c is the fraction of occupied sites, z is the number of equivalent neighboring sites, a_0 is the distance between equivalent sites, v_0 is a characteristic lattice frequency, and ΔG_m is the free energy of migration. f is

called the correlation factor which represents the deviation from randomness of the atomic jumps whose value depends on the nature of lattice.

Defining a term γ such that,

$$\gamma = \frac{z}{6} f exp\left(\frac{\Delta S_m}{k}\right) \tag{1.6}$$

where ΔS_m is the migration entropy, connected with the free energy and migration enthalpy (ΔH_m) by the relation,

$$\Delta G_m = \Delta H_m - T\Delta S_m \tag{1.7}$$

will give the new expression for mobility,

$$\mu = \frac{q}{kT}\gamma(1-c)a_0^2 v_0 \exp\left\{-\frac{\Delta H_m}{kT}\right\} \tag{1.8}$$

The classical relation connecting mobility and conductivity is given by,

$$\sigma = nq\mu \tag{1.9}$$

Here, n is the volume concentration of mobile ions. In this context, if $N$is the total number of equivalent sites,

$$\sigma = N\frac{q}{kT}\gamma c(1-c)a_0^2 v_0 \exp\left\{-\frac{\Delta H_m}{kT}\right\} \tag{1.10}$$

Now, $(1-c)$ can be equated with the fraction of mobile oxygen vacancies, $[V_{\ddot{O}}]$ for oxide ionic conductors. Therefore,

$$\sigma = N\frac{q}{kT}\gamma[V_{\ddot{O}}]_s(1-[V_{\ddot{O}}]_s)a_0^2 v_0 \exp\left\{-\frac{\Delta H_m}{kT}\right\} \tag{1.11}$$

This expression can be compared with the empirical relationship of conductivity, or the Arrhenius equation,

$$\sigma = \frac{\sigma_0}{T}\exp\left(-\frac{E_a}{kT}\right) \tag{1.12}$$

In the Arrhenius equation, the parameter σ_0 is the pre-exponential coefficient which incorporates all the factors that influence the ionic conductivity, other than activation energy. For most of the oxygen conductors the term c will

be temperature dependent. Taking that into account, we can see that most of the parameters that appear in the expression for conductivity are constants that do not vary substantially from oxide to oxide [Kilner 2000]. That means high density of mobile ions, availability of vacancies and good connectivity among the sites facilitating conduction channels with low activation energy (E_a) are the most important parameters that decide the conductivity property of oxide ionic conductors.

1.4.2. General survey of electrolyte materials

From the previous discussion, it is clear that the key requirement for an electrolyte material is to have high ionic conductivity and zero or little electronic conductivity. Control and amount of charge carrier species within the material is very critical. Tailoring the transport properties through structural and compositional tuning are widely reported [Garcia-Barriocanal *et al.* 2009]. The chemical and thermal stability, compatibility of physical characteristics with other components, etc. are also considered. Attempts to reduce the operating temperature, *i.e.*, to achieve high conductivity at intermediate temperature (500 – 800 °C), is also a major concern [Brett*, et al.* 2008]. A survey of various class of materials that are already reported hitherto in the literature is presented in this section.

1.4.2.1. Zirconia-based electrolytes

The most commonly used solid electrolyte in SOFC technology, yttria stabilized zirconia (YSZ), belongs to this class. Stabilized zirconia is a good choice due to its high ionic conductivity. Pure zirconia (ZrO_2) is not a good conductor, and moreover, at room temperature it has a monoclinic structure and mostly act as an electronic conductor. It transforms to tetragonal form on heating, at 1170 °C. On further heating, it again transforms to a cubic phase at 2350 °C which will be stable up to its melting point 2680 °C [Badwal and Ciacchi 2000]. These phase

transitions are accompanied by volume changes, which is not appropriate for a solid oxide electrolyte. In order to stabilize zirconia, dopants such as MgO, Y_2O_3, Sc_2O_3 *etc.* are added. For the most commonly used system, which is used in an operating temperature of 1000 °C, around 8.5 mol% of Y_2O_3 is used to stabilize zirconia in cubic phase and around 2 – 3 mol% of Y_2O_3 is used to stabilize it in tetragonal phase [Badwal 1992, Scott 1975]. There are theoretical proofs that oxide ionic conductivity is enhanced if all the oxygen ions in the lattice have similar energies, which points towards favoring a higher symmetry thus giving upper hand to cubic structures [Mogensen *et al.* 2004]. In addition to stabilizing the crystal structure, yttria also serves to create oxygen vacancies thereby increasing the ionic conductivity. With increase in dopant concentration, conductivity increases, reaches a maximum at around ~8 mol% and then decreases. The decrease at high concentrations is due to the association of point defect which decreases the mobility of charge carrying species [Nomura *et al.* 2000].

Scandia doped zirconia (ScSZ) shows higher conductivity than YSZ which is explained on the basis of comparatively smaller size mismatch between zirconium and scandium cations than that between zirconium and yttrium cations. This reduces the defect association energy and enhances the ionic mobility [Fergus 2003]. But still ScSZ is not preferred over YSZ for practical use due to some disadvantages. It has higher activation energies at lower temperatures, which leads to lower conductivity at lower temperatures. Also, for higher scandia mol%, it tends to transform to a rhombohedral structure which has a lower conductivity [Weller *et al.* 2004]. Due to slow cation diffusion kinetics, this system shows difficulty in achieving an equilibrium phase assembly [Thornber *et al.* 1970]. Attempts to prevent this phase change have been made by limiting the Scandia content or by co-doping with other oxides also [Chiba *et al.*

1996, Sarat *et al.* 2006]. YSZ and ScSZ have similar mechanical properties [Yamamoto *et al.* 1995]. Investigations carried out towards improving toughness and strength by adding oxides like alumina or niobates were success to some extent although they caused slight reduction in the conductivity [Mori *et al.* 1994].

An enhancement in electrical properties by additional doping on Sc- and Y-substituted zirconia is also reported in literature. Co-doping with calcium introduced oxygen sublattice distortions leading to decreased activation energy in YSZ thereby increasing the conductivity [Bućko 2006]. Bismuth oxide also increased the conducting properties of ScSZ [Sarat*, et al.* 2006]. Effect of alumina has been found to be detrimental at some instances, and advantageous at some other. In cases where alumina was found to scavenge silica, it was found to be advantageous for the conducting properties [Mori*, et al.* 1994], while in those cases where alumina led to defect associations it affected the conduction adversely [Guo 2001]. Cerium showed high saturation point in enhancing the conductivity of YSZ, where the defect association was not much pronounced [Lee *et al.* 2001].

1.4.2.2. Ceria-based electrolytes

Ceria is another popular solid electrolyte used in SOFC. It shows higher conductivity compared to zirconia at lower temperatures. Pure ceria (CeO_{2-x}) shows almost same partial conductivity for oxide ion, electron and hole diffusion. But the ionic conduction is significantly improved by impurities such as Na_2O, CaO and SrO [Panhans and Blumenthal 1993]. Doped ceria-based fuel cell units are reported to deliver four times the power delivered by zirconia-based cell due to very low cathode polarization resistance [Dalslet *et al.* 2006]. But in spite of this, ceria electrolytes show appreciable amount of electronic conductivity at lower oxygen partial pressures and is considered to be one of their major

drawbacks [Dalslet*, et al.* 2006, Kharton *et al.* 2004]. The most efficient dopants that enhance the conductivity of ceria are gadolinium and samarium due to the ionic size match [David A. Andersson 2006, Schwarz 2006, Yahiro *et al.* 1989]. In an investigation of effect of rare-earth doping in ceria by Yahiro *et al.*, $Ce_{0.8}Sm_{0.2}O_{1.9}$ was found to show the highest electrical conductivity [Yahiro*, et al.* 1989]. A similar trend was also reported elsewhere in an independent study involving a larger number of rare earth ions [Inaba and Tagawa 1996]. As in the case of zirconia compositions, while attempting to tailor conduction properties by doping, conductivity increases with doping to a maximum and then decreases [Seo *et al.* 2006].

As candidates for dopants, other ions like lanthanum [Shimonosono *et al.* 2005, Suda *et al.* 2006], yttrium [HartmanovÁ *et al.* 2005, Kharton*, et al.* 2004], neodymium [Sameshima *et al.* 2006], niobium [Yashiro *et al.* 2004], erbium [Kuharuangrong 2007], ytterbium [Hong *et al.* 1998] *etc.* are also tried. But the conductivity enhancement introduced by these were typically below that of Gd and Sm [Pikalova *et al.* 2011]. Co-doping strategy has been employed for ceria electrolytes too, as was done with zirconia. Co-doping with praseodymium and samarium in Gd-doped ceria enhanced the electrical conductivity, praseodymium being more effective between the two [Torrens *et al.* 2004]. Co-doping strategy with samarium and yttrium is also reported to be advantageous [Sha *et al.* 2007]. The positive effect of doping does not just come as a direct influence on electrical properties, but may also happen indirectly, for example, by enhancing sintering properties [Mori *et al.* 2006, Yoshida and Inagaki 2006]. Co-doping by cobalt is reported to have improved the sintering behavior of Gd-doped ceria which in turn have increased the conductivity [Hari Prasad *et al.* 2012]. The solid solution formation, densification and mechanical properties of Gd and Sm doped ceria are also reported by various authors [Reddy and Karan 2005, Reis *et al.* 2011].

The main issues when doped ceria is used as fuel cell electrolytes arise from the partial reduction of Ce^{4+} to Ce^{3+} [Mogensen *et al.* 2000]. This gives an internal n-type electronic conduction which acts as a leakage current. Another after-effect of this reduction is the expansion of the lattice due to difference in ionic radii between tetravalent and trivalent cerium ions which can deteriorate the mechanical strength [Gödickemeier and Gauckler 1998]. Considering that doped ceria has higher conductivity than zirconia based electrolytes at lower temperatures, and that they possess electronic conductivity at higher temperatures, ceria based electrolytes are viable only for low-temperature operation. They also have superior chemical stability with cathode materials [Ralph *et al.* 2001].

1.4.2.3. Perovskite-type electrolytes

Perovskites are a class of materials with a general formula ABO_3 and space group Pm3m [Kendall *et al.* 1995]. Although idealized perovskite structure is devoid of oxygen vacancies, it is possible to incorporate plenty of them by cation substitution and therefore high ionic conductivity can be achieved. Depending on the nature and extent of substitution perovskite compounds show wide range of ionic conductivity values, from essentially zero to even exceeding that of doped zirconia.

Doped lanthanum gallate is one of the most promising solid oxide electrolyte in the perovskite class [Ishihara *et al.* 1994, Ishihara *et al.* 1995]. $LaGaO_3$ can be doped with strontium and magnesium, $La_{1-x}Sr_xGa_{1-y}Mg_yO_3$ (LSGM) to achieve high conductivity at intermediate temperature [Joshi *et al.* 2004]. LSGM compositions have conductivity higher than YSZ or ScSZ, or similar to doped ceria. However they do not have easily reducible ion like the Ce^{4+}, and are more useful in lower oxygen partial pressures. Attempts to enhance the conducting properties of LSGM by doping with transition metals like cobalt

[Ishihara *et al.* 2004], iron [Enoki *et al.* 2006], aluminium [Yasuda *et al.* 2000] etc. are reported. Although cobalt and iron enhance the conductivity, they also decrease hole conductivity which is not advantageous to fuel cell performance. By balancing various parameters like electrolyte thickness and hole conductivity, efficient fuel cells with cobalt doped LSGM electrolyte have been produced [Inagaki *et al.* 2006]. Nickel is also reported to have a similar influence as that of cobalt in LSGM compositions [Yaremchenko *et al.* 2006]. Some disadvantages of LSGM electrolytes are the possible volatilization of gallium oxide, formation of secondary phases during processing, reactivity with perovskite-type electrodes, and comparatively high cost of gallium [Djurado and Labeau 1998, Stevenson *et al.* 1998].

Another type of perovskite materials which attracted interest is cation substituted $LaAlO_3$ [Hayashi *et al.* 1999]. Although they have relatively low cost, moderate thermal expansion and high stability, their conductivity values are not so promising. Attempts to enhance this conductivity by doping with metals like strontium [Nomura and Tanase 1997], gallium [Ishihara*, et al.* 1994] are also reported which shows an influence of substitution on conductivity to some extent on consideration of ionic sizes. Other perovskites like $LnGaO_3$ (Ln = Nd, La) [Ishihara *et al.* 1996], $GdAlO_3$ [Sinha *et al.* 2008] *etc.* are also investigated in this respect. Perovskite-related structures like Ln_2NiO_{4+d} (Ln = La, Nd, Pr) where conduction is carried out through interstitial oxygen transport showed significant amount of electronic conductivity [Zhou *et al.* 2009]. However the feasibility of being used in a practical fuel cell needs a lot of further studies.

1.4.2.4. Bismuth oxide based electrolytes

Pure bismuth oxide has two thermodynamically stable polymorphs, α-Bi_2O_3 which is stable below 730 °C and δ-Bi_2O_3 which is stable above 730 °C up to its melting point 825 °C [Azad *et al.* 1994]. α-phase has a monoclinic structure

while the δ-phase crystallizes in a cubic fluorite structure. δ-Bi_2O_3 exhibits very high conductivity due to the presence of oxygen vacancies, which is attributed to the high polarizability of Bi^{3+} ions [Battle *et al.* 1986]. However the very narrow range of temperature over which this high conductivity phase is stable and the volume change associated with the phase transition makes it practically impossible to be used in fuel cell. Addition of dopants is proved to be useful for stabilizing Bi_2O_3 in δ-phase at lower temperature. In some cases the doping leads to transformation into a more conducting rhombohedral phase. However this conductivity is a strong function of oxygen partial pressure in gas phase [Takahashi *et al.* 1972]. Stabilization of bismuth oxide phase at lower temperature has been achieved by substitution of bismuth with rare-earth dopants such as Y, Dy or Er and their combination with higher valency cations such as W or Nb [Kharton*, et al.* 2004]. But however this can reduce ionic conductivity. Bi_2O_3-based materials are practically very difficult to use due to many disadvantages like instability in reducing atmosphere, volatilization at moderate temperatures, poor mechanical performance, high corrosion activity *etc.*

1.4.2.5. Apatite-type electrolytes

Apatite-type materials have a general composition of $M_{10}(XO_4)_6O_{2\pm y}$, where M is a rare-earth or alkaline-earth cation, X is a p-block element and *y* is the amount of oxygen non-stoichiometry [Kendrick *et al.* 2007]. The interest in these type of materials gained attention when fast oxide ion conductivity is reported in $Ln_{9.33}(SiO_4)_6O_2$ (Ln = lanthanide cation) [Nakayama *et al.* 1995]. Si- and Ge-based lanthanum apatites with a hexagonal symmetry are the best among these compositions reported until now [Nakayama *et al.* 1995]. A marked difference apatites show from ceria or zirconia systems is that their high conductivity is not materialized by vacancy-hopping mechanism, but by

interstitial oxygen ion transport. They show very high oxygen transference numbers for a wide range of oxygen partial pressure [Leon-Reina *et al.* 2004]. Although several possibilities of improving ionic transport and chemical properties have been explored, range of oxygen non-stoichiometry is comparatively very narrow [Kendrick, *et al.* 2007]. However, the apatite structure can accommodate a wide range of cation dopants which facilitate large local distortions and lattice volume changes. Lower valent dopants usually improve conductivity while isovalent ones suppress it due to trapping of interstitial oxygen ions. In cation-doped germinate apatites oxygen excess did not enhance the conductivity due to lower symmetry in triclinic structure which caused the oxygen to be tightly bound [Pramana *et al.* 2007]. However, attempts to stabilize these compositions in hexagonal phase by doping with Y, as in $La_8Y_2Ge_6O_{27}$ helped achieving good conductivity at low temperatures [Kendrick and Slater 2008]. Although testing of apatite electrolytes in fuel cells is already underway, there are still many aspects of these materials that need exploration [Marrero-López *et al.* 2010]. Since sintering of apatites require high temperatures, typically higher than 1600 °C, it poses limitations to their practical application [Shaula *et al.* 2006].

1.4.2.6. LAMOX-based electrolytes

LAMOX is a class of fast oxide-ion conducting compounds with a base composition $La_2Mo_2O_9$ [Lacorre *et al.* 2000]. It exhibits two phases, one α-phase with a monoclinic structure and another β-phase that has a cubic phase. The β-phase which forms at a temperature of above 580 °C exhibits good conductivity as high as 6×10^{-2} Scm^{-1} at 800 °C. In the cubic phase, there are three oxygen sites two of which are partially occupied with high thermal displacement parameters. This substantial disorder in the oxygen sub-lattice is considered to be the reason for high oxygen conductivity. Despite its attractive conducting properties, the

structure transition accompanied by significant volume strain and the stability issues in reducing atmospheres make pure LAMOX a poor choice as practical electrolyte. The cubic phase can be stabilized at room temperature without much compromise in conductivity by doping LAMOX with alkaline or alkaline earth cations on the La site [Georges *et al.* 2003, Tealdi *et al.* 2008, Wang *et al.* 2005]. But at the same time, reduction of LAMOX readily in dilute hydrogen leading to eventual decomposition has also been demonstrated [Goutenoire *et al.* 1999]. In addition to this, high chemical reactivity and thermal expansion coefficient also remain as a challenge in the use of LAMOX as electrolytes [Jacobson 2010].

1.4.2.7. Gallium oxide-based electrolytes

Oxide compositions containing GaO_4 tetrahedral units are reported to show high oxygen ion conduction [Kuang *et al.* 2008]. Variation of La/Ba ratio in $LaBaGaO_4$ compound introduces oxygen vacancies in the lattice which leads to the formation of Ga_2O_7 groups combining two GaO_4 units. The transfer of oxygen ions between neighboring tetrahedra by breaking the Ga_2O_7 groups is what facilitates the long range ionic diffusion [Kendrick *et al.* 2007]. This is an unusual kind of transport mechanism and seemingly similar high conductivity may be possible in compounds with flexible structural networks. $LaSrGa_3O_7$-based system with a melilite structure is reported with an interstitial oxide ionic conductivity [Kuang*, et al.* 2008]. Although the parent compound is not a good conductor, tailoring La/Sr ratio can enhance the conductivity. Flexibility of structural network in which the coordination of Ga ions can change readily is a common feature of gallium-based conductors. However, the synthesis of these materials is challenging and special care is needed to get a single-phase.

Apart from all these types of compositions, certain other classes like Brownmillerite, Aurivillius *etc.* are also reported in literature [Abraham *et al.* 1988, Goodenough *et al.* 1990, Kendall*, et al.* 1995]. There is another important

class of materials which we have not discussed yet– cubic pyrochlores. Pyrochlore structure is closely related to the cubic fluorite structure where zirconia and ceria based electrolytes belong to. The chemical systems investigated in the present research work belong to either fluorite or pyrochlore structure and hence a detailed discussion on these structures and their inter-relation will be made in coming sections. A survey of pyrochlore/fluorite structured solid electrolytes will also be presented.

1.4.3. Search for electrolytes – Relevance of the present work

The discussion on solid oxide fuel cells establishes it clearly that electrolyte is the crucial component that decides the fabrication and operation of a fuel cell unit. Almost 70% of the global energy consumption depends on conventional fossil fuels like coal, oil, natural gas etc. Considering the irrefutable facts that global energy demand is raising as never before and at the same time fossil fuels are getting exhausted, our future depends literally on our ability to find alternate energy resources. The concomitant environmental hazards posed by the extensive use of fossil fuels makes the situation more sombre. Fuel cells, especially solid oxide fuel cells, offer a clean prospect of renewable energy. It has attracted much interest from the scientist and engineer community towards them. Due to the peculiar and stringent material requirements for the various components in an SOFC, concerted efforts are required for improving the performance of each of them.

The present research work involves a search for new solid oxide electrolyte materials to be used for fuel cell applications. As the survey of electrolyte materials presented in the earlier section implies, a lot of parameters have to be considered and optimized for the effective use of a particular material as a practical electrolyte. Very many aspects like structure, lattice parameter(s), lattice volume, nature of ions, lattice defects like vacancies and interstitials, bond

strength, thermal expansion behavior, structure transition etc. are reported evidently to have an effect on the properties of a solid electrolyte. Despite extensive research, there does not exist any general rule with which we can design and synthesize the best electrolyte materials. Only certain classes of materials which shows promising physical and chemical characteristics have been identified. Moreover, since the various components of a solid oxide fuel cell should possess certain matching physical properties, there are limitations migrating to entirely new ceramic systems too.

The present thesis focuses on fluorite and pyrochlore structured materials. A few novel chemical systems have been synthesized and their properties were investigated in detail keeping in mind a goal of achieving the best conduction properties. Attempts to recognize the crucial factors that affect the electrolyte behavior, and to find the correlation between various structural characteristics and electrical conductivity have been made.

1.4.4. Pyrochlore and Fluorite crystal structures

Pyrochlores and fluorites are two structural classes of materials whose crystal structures are interconnected. These generic structure names come from isostructural minerals of the respective names. Pyrochlore mineral, which has a chemical composition of $(Na,Ca)_2Nb_2O_6(OH,F)$, is one of the common ores of niobium metal. It derives its name from the Greek words '*pyro*' (for fire) and '*chlore*' (for green) since it turned green on ignition [Mineralogy 2010]. Fluorite structure is named after the well-known halide mineral, calcium fluoride (CaF_2), which crystallizes in an isometric cubic habit [Anthony 2011]. Photographic images of pyrochlore and fluorite minerals is shown in Figure 1-3.

Pyrochlore structured materials have a general compositional formula of $A_2B_2O_6O'$ with $Fd\bar{3}m$ space group while fluorite structured compositions have a

general formula of AO_2 with space group $Fm\bar{3}m$. Pyrochlore is often considered a superstructure of fluorite, with an ordered cationic distribution in two different sites and an absence of one in every eight anions. Structural transformation among these phases are commonly observed with change in temperature, pressure, chemical composition *etc*. [Wuensch *et al.* 2000].

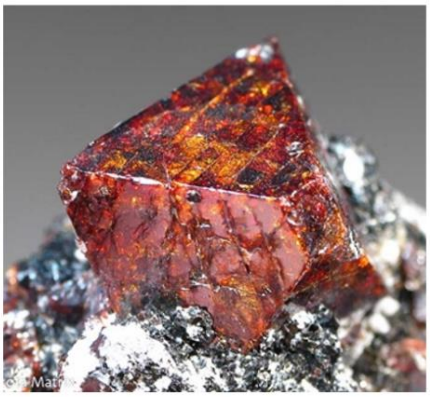

A pyrochlore mineral specimen
(Courtesy: Dakota Matrix Minerals)

A fluorite crystal on mica matrix
(Courtesy: Wikipedia)

Figure 1-3: Photographs of the pyrochlore and fluorite mineral samples

1.4.4.1. Fluorite structure

In an ideal fluorite structure, there are only two crystallographically different ionic sites, one occupied by cations and the other by anions. The cations constitute a face-centred lattice and are coordinated cubically by eight anions. Anions are coordinated by four cations which form a tetrahedron around each of them. The Figure 1-4 shows the schematic representation of one unit cell of an ideal fluorite lattice.

There are four formula units of AO_2 in a fluorite unit cell (Z = 4). The eight-coordinated cations have O_h site symmetry and the four-coordinated anions have T_d site symmetry [Glerup *et al.* 2001]. Fluorite-structure can accommodate gross non-stoichiometry in its composition, like partial incorporation of aliovalent cations in 4*a* site, there by becoming a 'defect-fluorite'

phase with general form $A_{1-x}B_xO_{2-y}$ or similar. In defect fluorites, cation sublattice is completely occupied while the anion deficiency is often accommodated as vacant lattice sites.

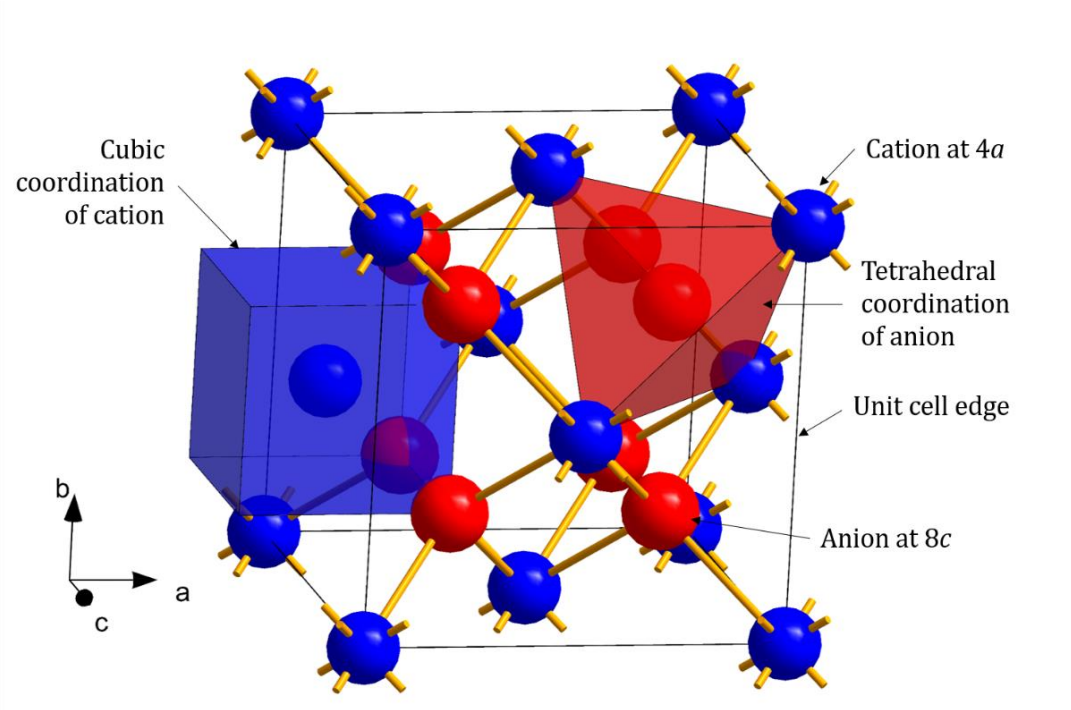

Figure 1-4: Unit cell of a fluorite lattice. Blue spheres represent cations, red spheres represent anions and the polyhedra represent the coordination environments of both.

1.4.4.2. Pyrochlore structure

Pyrochlore is considered an ordered superstructure of an anion-deficient fluorite structure. It is obtained by doubling the cation sites and removing one-eighth of the anions. Like the fluorite lattice, pyrochlore also has a cubit unit cell but with double the lattice parameter including eight formula units (Z = 8). The various ions in the general formula $A_2B_2O_7$ are distributed in crystallographically different sites. One-eighth of the pyrochlore unit cell is illustrated in Figure 1-5. Although the selection of origin is arbitrary, most of the existing literature on pyrochlores takes the B-cation as the origin, denoted by the Wyckoff symbol 16*c*. This thesis also shall be following the same convention

throughout. Here, the A-cations occupy 16*d* site (0.5, 0.5, 0.5). Both of these sites have D_{3d} site symmetry. Anions are distributed into three different Wyckoff equipoints; the 48*f* (*x*, 0.125, 0.125), which has two A- and two B- nearest neighbours, the 8*a* (0.125, 0.125, 0.125), which has four B nearest neighbours and the 8*b* (0.375, 0.375, 0.375), which has four A nearest neighbours.

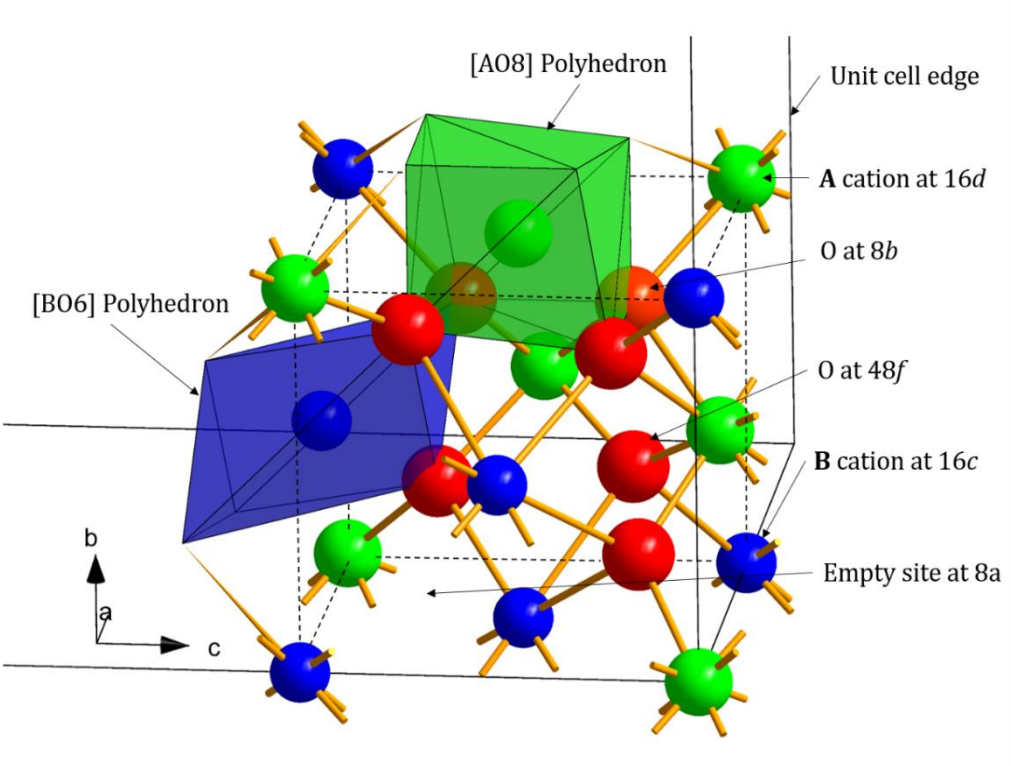

Figure 1-5: One-eighth of a pyrochlore unit cell. Blue and green spheres represent cations, red spheres represent anions and the polyhedra represent the coordination environments.

There are two types of cation coordination polyhedra. The A-cations are located within scalenohedra (distorted cube) formed by eight oxygen ions and the B-cations within trigonal antiprisms formed by six oxygen ions. It can be seen that while coming from fluorite to pyrochlore structure, loss of an anion reduces the coordination of B-site from eight to six. The eight anions in the 8*b* sites are coordinated by four A-cations whereas all the other anions (in 48*f* site) are each coordinated by two A-cations and two B-cations. The 8*a* sites act as 'vacancies'

which facilitates the transport of ions in the crystal. However these sites do not belong to either the anionic or cationic sublattice, but are merely the interstices in pyrochlore lattice. While comparing with the ideal fluorite structure, the 8*a* sites coincide with anion sites and hence they are conventionally thought of as anion vacancies [Hartmann *et al.* 2011]. All the atoms in an ideal pyrochlore are on special positions, except the 48*f* oxygen which has a variable *x*-coordinate. Thus the lattice parameter and oxygen *x*-parameter are sufficient to describe an ideal pyrochlore structure [Ewing *et al.* 2004]. As the 48*f* oxygen shifts to accommodate cations of different sites, the *x*-parameter varies resulting into a change in shape of the coordination polyhedra. For *x* = 0.375, A-site polyhedra will be a regular cube and the B-site polyhedron will be a trigonally flattened octahedron. In that case the structure would essentially become a defect-fluorite. For *x* = 0.3125, A-site forms a distorted trigonal scalenohedron around it and the material attains an ideal fluorite structure [Minervini *et al.* 2000].

The stability of pyrochlore structure is often expressed in terms of the ratio between radii of the cations occupying A- and B-sites. The ratio ($\frac{r_A}{r_B}$), where r_A represents the average ionic radius of the cation/cations occupying the A-site and $r_B$represents the same for B-site, often conveys an idea about the structure in which a composition is likely to stabilize [Zhang *et al.* 2005]. Pyrochlore structure is favoured for cationic arrangements in which the radius ratio falls in between 1.46 and 1.78 [Minervini*, et al.* 2000, Subramanian *et al.* 1983]. Due to this, most of the known pyrochlore compositions are (3+, 4+)-type since a lot of A^{3+} and B^{4+} cations have suitable ionic radii for satisfying this criterion.

1.4.4.3. Order-disorder Structure transition

We have discussed that pyrochlore and fluorite are two closely connected crystal structures. Between these two, pyrochlore has more number

of crystallographically different lattice sites and is considered to be an ordered phase. Fluorite on the other hand is a disordered structure with only two different equipoints, each for cation and anion. Since the order in pyrochlore is strongly dependent on the size difference between the cations involved, *viz*, the radius ratio, it is much prone to a transition to its disordered parent structure of fluorite. A number of useful properties of these materials are connected to this order-disorder structure transitions.

According to Minervini *et al.*, who analysed the stability field of pyrochlore formation using atomistic simulations, the stability range can be divided into four regions. Compounds with positive reaction enthalpies can never form pyrochlore compounds with $A_2B_2O_7$ form. The pyrochlore formation is favored in a disorder enthalpy above ~2.6 eV. Compounds within an intermediate transition region form as defect-fluorites. Compounds with very large radius ratio, *i.e.* large A-cation and small B-cation, prefers to have non-cubic unit cells [Minervini*, et al.* 2000]. When pyrochlore structure transforms to a fluorite/defect-fluorite structure, the disordering process happens independently for both cations and anions. Also there are reports that these independent disordering processes have different rates [Wuensch*, et al.* 2000]. As we have seen, the 48*f*-oxygen has a variable *x*-coordinate. Since the 8*a* site is normally vacant in an ideal pyrochlore structure, and therefore the 48*f*-oxygen tends to shift towards the two nearby B-cations, leading to a decrease in *x*-parameter. But when the difference in size between two cations decreases, the 16*c* and 16*d* Wyckoff positions begin to get occupied by random A- and B- cations. The 8*a* site begins to get occupied, which would prevent the shift of 48*f* oxygen towards it. This will increase the oxygen x-parameter, which acts as an indicator of lattice disordering. This disorder disrupts the distinction between many lattice planes, and will lead to the decreased efficiency of x-ray scattering from them.

This will be evident in the x-ray diffraction pattern of these samples as diminishing and finally disappearing of certain peaks, which are conventionally called superlattice peaks. Monitoring the intensity of superlattice peaks can thus be used as the simplest method for distinguishing lattice disorder in pyrochlore compounds.

Cations are responsible for most of the x-ray scattering from a crystal. Therefore x-ray diffraction is not sensitive to order or disorder in the anionic sublattice. For that we can use Raman spectroscopy which depends on the vibrations of cation-anion bonds. A factor group analysis would show that cubic pyrochlores possess six Raman active modes whose irreducible representations are given as [Poulsen *et al.* 2000],

$$\Gamma(\text{Raman}) = A_{1g} + E_g + 4T_g$$

Pyrochlores belong to a factor group O_h, with D_{3d}, C_{2v} and T_d being the respective site symmetries of cations, 48*f* oxygen and 8*b* oxygen. The force fields used for the calculation are essentially transferable among various pyrochlore compositions, and hence a comparison with earlier results will suffice to assign vibrational bands to the observed peaks [Vandenborre *et al.* 1983]. On the other hand, in fluorite structure with $Fm\bar{3}m$ space group A-cations have a site symmetry of O_h and for oxygen it is T_d. Hence all the O ions in a fluorite structure are in crystallographically identical lattice sites. Due to this the Raman spectrum of a fluorite structure is reduced to a broad continuum of density of states. Only one Raman active mode (T_{2g}) is known in a fluorite structure. This difference in Raman spectra is very instrumental in probing the order-disorder transitions in pyrochlore-related systems. Unlike X-ray diffraction, it has an advantage of being sensitive to the anionic sublattice also [Glerup, *et al.* 2001].

The order-disorder transitions can be driven by many factors. Sometimes heating of materials to a sufficiently high temperature can cause a transformation from pyrochlore to fluorite structure. For example, pyrochlore-type $Gd_2Zr_2O_7$ transforms into defect-fluorite when heated to 1575 °C. For $Sm_2Zr_2O_7$ and $Nd_2Zr_2O_7$, the respective transition temperatures are 2000 °C and 2300 °C [Jacobson 2010]. Another way of inducing disorder is to irradiate pyrochlore samples with ion-beam. Such transitions are mostly reported in rare-earth zirconate pyrochlores [Kendall*, et al.* 1995, Tuller 1992]. Pressure can also drive structure transitions. $Gd_2Zr_2O_7$ is prone to change to a monoclinic phase with respect to change in pressure [Massimiliano Lo Faro 2009, Zhang *et al.* 2007]. In spite of all these, the most common way of inducing disorder is to directly tailor the radius ratio of cations by varying the composition.

Isovalent and aliovalent substitutions are widely reported to accompany order-disorder transitions with significant influence on different physical properties. Substitution of Zr by Ti in $Y_2(Zr_yTi_{1-y})_2O_7$ induced lattice disorder which enhanced the oxygen ion conductivity [Wuensch*, et al.* 2000]. Incorporation of Tb in Gd-site of pyrochlore-type $Gd_2Zr_2O_7$, showed a transition to fluorite phase and detailed investigations suggest that at some stages both phases can coexist [Reynolds *et al.* 2013]. Order-disorder transitions in rare earth zirconates with cation substitution and its influence on the electrical and thermal properties are widely reported [B.P. Mandal *et al.* 2008, Mandal *et al.* 2007, Mandal *et al.* 2010, Sayed *et al.* 2012]. Disordering in $(Sm_{1-x}Yb_x)_2Zr_2O_7$ is reported to give rise to unconventional thermal conducting properties [Wan *et al.* 2011].

1.4.5. Conduction in pyrochlore crystals

The conduction mechanism in pyrochlore-type crystals is through the ionic migration of oxygen through the 48*f* sites. All of the oxygen sites in pyrochlore have other oxygen sites as their second nearest neighbors. The second

nearest neighbors of 8*a* and 8*b* sites are always 48*f* sites. None of them offers a diffusion path since they do not form a continuous network. But while considering the 48*f* site, the second nearest neighbours being 8*a*, 8*b* and other 48*f* sites, have a continuous network around which would facilitate a vacancy hopping mechanism for oxygen ions [Moon and Tuller 1988]. Also the defect formation energy for a vacancy on 48*f* is lower than that for one in 8*a* sites. Thus the commonly proposed mechanism of ionic diffusion involves thermally generated oxygen vacancies in 48*f* sites shifting oxide ions into the systematically vacant 8*b* site. In the case of cation disorder, as in pyrochlore-to-fluorite transitions, the environments of 48*f* and 8*b* oxygen sites become similar leading to a decrease in anion Frenkel defect formation energy. Thus disorder facilitates more intrinsic defect formation which can help conduction process.

Conduction mechanism in all manner obeys the Arrhenius equation of thermally activated process. The conductivity can increase by decrease in activation energy, or by increase in number of charge carriers or by both. In this light the ionic conduction in pyrochlores can be classified into two types: Intrinsic ionic conduction and extrinsic ionic conduction.

Anion disorder in pyrochlores happens by generation of vacancies in 48*f* oxygen sites. The conductivity in these materials can be significantly enhanced by increasing the oxygen vacancy concentration. Moon *et. al.*, reported a dramatic increase in conductivity in $Gd_2(Zr_xTi_{1-x})_2O_7$ pyrochlore system due to increased charge carriers [West 1984]. Defect concentrations due to anionic disorder was also very advantageous to $Y_2(Zr_yTi_{1-y})_2O_7$ system where conductivity increased by more than order of magnitude [Heremans *et al.* 1995]. This study also confirmed the role of 48*f* oxygen in the migration mechanism of ions. In both these studies, there was no appreciable change in the activation energy. The ionic conductivity

can also be improved extrinsically by acceptor doping. Kramer reported an enhancement in conductivity to about two orders of magnitude by doping in $(Gd_{1-x}Ca_x)_2Ti_2O_7$ pyrochlore [Kilner 2000].

1.4.6. Preface to the current thesis

The present research work is an attempt to synthesize and characterize a few chemical systems that can be used as a practical solid electrolyte. Focus has been given particularly to zirconate compositions that crystallize either in a fluorite or a pyrochlore structure. The order-to-disorder structure transitions between pyrochlore and fluorite structures were also studied. The design of compositions was such that one or more of cation sites in an already established chemical system, *viz* a rare earth zirconate, gets partially substituted. The extent of substitution was varied continuously so that the accompanying change in crystal structure and electrical properties could be monitored. Changes in structural characteristics and those in the electrical conducting properties were correlated. Attempt to recognize the important physical parameters that are to be taken into account while developing an effective ionic conductor was made. Investigations on different chemical systems are discussed in the coming four chapters. A brief review of existing investigations in similar premises is presented in the introduction part of each chapter. The major conclusions are then summarized in the sixth chapter. Future scope of the work, including attempts for further improvement in properties and more characterizations for throwing light on further physical aspects, is also discussed.

CHAPTER 2

****

Induced Oxygen Vacancies and their Effect on the Structural and Electrical properties of Fluorite-type $CaZrO_3$-$Gd_2Zr_2O_7$ system

****

Chemical compositions with a stoichiometry involving x% of $CaZrO_3$ and (100-x)% of $Gd_2Zr_2O_7$ (x = 10, 20, 33.3, 40) are prepared. The correlation between crystal structure and electrical properties were investigated through various characterization techniques. The aliovalent substitution of Gd^{3+} by Ca^{2+} allowed creation of more oxygen vacancies in the lattice of these compositions. This resulted into a progressive decrease in lattice parameter and an increase in thermal expansion coefficient. The induced oxygen vacancies provided a lower energy barrier for ionic diffusion and hence led to an increase in conductivity. Presence of $CaZrO_3$ impurity phase in one of the samples was found to be detrimental to conductivity.

Vaisakhan Thampi, Prabhakar Rao Padala and A. N. Radhakrishnan, "Induced Oxygen vacancies and their effect on the Structural and Electrical properties of a Fluorite-type $CaZrO_3$–$Gd_2Zr_2O_7$ system", ***New Journal of Chemistry***, 39, 1469–1476 (2015)

2.1. Introduction

Rare earth zirconates of the type $RE_2Zr_2O_7$ are being explored extensively as potential candidates to be used as solid oxide electrolytes. Moreover, they are found to exhibit a lot of interesting properties thanks to their high melting point, thermal stability, thermal expansion coefficient *etc.* [Liu *et al.* 2010, Liu *et al.* 2011, Liu *et al.* 2010, Shlyakhtina and Shcherbakova 2012]. They possess a defect pyrochlore or defect fluorite type crystal structure which are capable of accommodating comparatively large amount of oxygen non-stoichiometry helpful for effective ionic diffusion in a solid electrolyte. Many attempts to enhance their ionic conductivity by doping with aliovalent or isovalent elements to RE or Zr sites have been reported [Kharton *et al.* 2003, Kumar *et al.* 2005, Moreno *et al.* 2006, Porat *et al.* 1997, Radhakrishnan *et al.* 2011].

Among the various zirconate systems reported, $Gd_2Zr_2O_7$ is found to be a very good candidate owing to its high electrical conductivity [Liu *et al.* 2012, Liu *et al.* 2008, Xia *et al.* 2010]. From crystallographic point of view, it is known to exist in two different space groups depending on the conditions of preparation [Lee *et al.* 2009]. If annealed at a temperature above 1773 K, it attains an anion-deficient fluorite structure with space group $Fm\bar{3}m$, whereas below 1773 K, it normally exists as a disordered pyrochlore with space group $Fd\bar{3}m$ [Lee, *et al.* 2009]. An investigation on the effect of Eu^{3+} substitution in place Gd^{3+} done by Xia *et al.* [Xia, *et al.* 2010] showed that the ionic conductivity of $Gd_2Zr_2O_7$ increases with increase in Eu^{3+} content. A similar substitution of Gd^{3+} with Sm^{3+} in $Gd_{2-x}Sm_xZr_2O_7$ system was studied by Liu *et al.* and they found $GdSmZr_2O_7$ (x = 1) to be the best among them in terms of ionic conductivity [Liu, *et al.* 2012, Liu, *et al.* 2008]. Later they studied the effect of CaO addition in the $GdSm_{1-x}Ca_xZr_2O_7$ ($0 \leq x \leq 0.20$) system [Liu *et al.* 2012] and reported that addition of CaO could increase

the ionic conductivity of the system up to x = 0.10. But, towards higher concentrations, CaO was found to decrease the conductivity of the system by enhancing the formation of $CaZrO_3$ secondary phase. Xia *et al.* had already studied the effect of CaO on $(Sm_{1-x}Ca_x)_2Zr_2O_7$ system [Xia *et al.* 2009] and reported that formation of poorly conducting $CaZrO_3$ phase is detrimental to the ionic conductivity of the system. Aliovalent substitutions can cause interstitial or vacant anionic sites in order for the requirement of electroneutrality and this can crucially influence various physical properties of the materials [Inaba and Tagawa 1996, Mogensen*, et al.* 2000, Sayed *et al.* 2012, Shlyakhtina *et al.* 2014]. Inducing oxygen vacancies can create an easy pathway for ionic diffusion through a crystal lattice thereby making it a better conductor. This is also reported to influence the thermal expansion behaviour of solid oxide materials [J. W. Stevenson *et al.* 2000, Masashi Mori *et al.* 2000, Wang *et al.* 2004]. Hence it should be inferred that addition of divalent Ca can influence the ionic conductivity positively, provided it does not lead to the formation of poorly conducting secondary phases.

Here in this work an attempt to add more Ca^{2+} to $Gd_2Zr_2O_7$ without the formation of secondary phases has been made. Solid solutions were prepared by proposing a stoichiometry of $x CaZrO_3–(1-x)Gd_2Zr_2O_7$ and their structural and electrical characteristics were investigated.

2.2. Experimental

For brevity, the proposed chemical systems in the present chapter will be designated as GZ, CGZ 10, CGZ 20, CGZ 33 and CGZ 40 where GZ stands for $Gd_2Zr_2O_7$ and the numeral following CGZ represents the value of the particular percentage (x) in $x\%CaZrO_3 – (100-x)\%Gd_2Zr_2O_7$ stoichiometry (x = 10, 20, 33.3, 40). It is also emphasized that the term '$CaZrO_3$' in the stoichiometry is used only

to indicate the proportion of cations and the perovskite-type $CaZrO_3$ phase as such was not involved in any stage of the synthesis process.

Conventional solid-state reaction route was adopted in this work for the synthesis of solid materials. Commercially available $CaCO_3$ (Acros, 99.9%), Gd_2O_3 (Aldrich, 99.9%) and ZrO_2 (Aldrich, 99%) were chosen as the starting materials. The dried powders of the reactants were weighed stoichiometrically and the starting mixture was mixed thoroughly in an agate mortar in acetone medium with intermittent drying to attain maximum homogeneity. The mixtures in pellet form were calcined at first at a temperature of 1573 K for 6 hours. The calcined pellets were ground to fine powder, again made to pellets and were reheated to 1873 K for 6 hours. Dense pellets were prepared by pressureless sintering of pellets at 1923 K for 24 hours. The green pellets for sintering were made by uniaxial compaction of powder samples at a pressure of 25 MPa.

The phase composition of sintered samples at room temperature was analysed using an X-ray diffractometer (X'pert Pro, PANalytical) employing Cu Kα radiation with a wavelength of 1.5406 Å. XRD data were recorded in the 2θ range from 10° to 90°. Morphological study was done using a scanning electron microscope (JEOL JSM-5600LV) and a transmission electron microscope (TEM, TECNAI 30G2 S-TWIN, The Netherlands). Finely powdered samples dispersed in acetone by ultrasonication were drop-cast onto carbon-coated copper grids for TEM study. Lattice thermal expansion behaviour was investigated by high-temperature X-ray diffraction analysis (Anton Paar HTK-attachment) Electrical characterization of the sintered pellets was carried out using an impedance analyser (Solartron SI 1260) with a dielectric interface (Solartron 1296), the measurement being done in air in a frequency range from 1 Hz to 1 MHz, from 473 K to 1023 K in intervals of 50 degrees. Electroding was facilitated by painting

silver paste over the flat polished surfaces of the cylindrical pellets. Silver wires were used to connect the samples to the frequency response analyser *via* the dielectric interface.

2.3. Results and Discussion

The proposed chemical compositions consisted of *x*% of $CaZrO_3$ and *(100-x)*% of $Gd_2Zr_2O_3$ in their stoichiometry; *x* being 0, 10, 20, 33 and 40 for different samples. Such a stoichiometry assumed substitution of Gd^{3+} by Ca^{2+} due to their similar ionic radii and the difference in valence of these two ions could introduce anionic vacancies in the lattice. The solid state reaction route yielded powder samples which were then made into pellets and sintered at 1923 K. For structural studies like X-ray diffraction and transmission electron microscopy the sintered samples were ground to form fine powder, while the pellets as such were used for scanning electron microscopy and impedance spectroscopy studies.

2.3.1. Crystal structure

X-ray diffraction study of powdered samples was primarily used to investigate the crystal structure of the samples. The peak patterns, in general, were found to be typical of the cubic fluorite structure (ICDD pattern code: 00-016-0799). The CGZ 40 composition showed minor secondary phase reflections that are not characteristic of cubic fluorites. These impurity peaks, indicated by asterisks in Figure 2-1, were corresponding to the perovskite type structure of $CaZrO_3$. It implied a limit up to which $CaZrO_3$ can be stoichiometrically added to $Gd_2Zr_2O_7$ without compromising the phase purity of the crystal lattice.

A close examination of the qualitative aspects of the patterns shows a shift of peaks towards higher angles with increase in amount of $CaZrO_3$, as evident in the right panel of Figure 2-1 which is an expanded view of the (200) reflection. The figure also indicates that the CGZ 40 sample falls off this trend

which should obviously be due to the considerable amount of impurity phase formation.

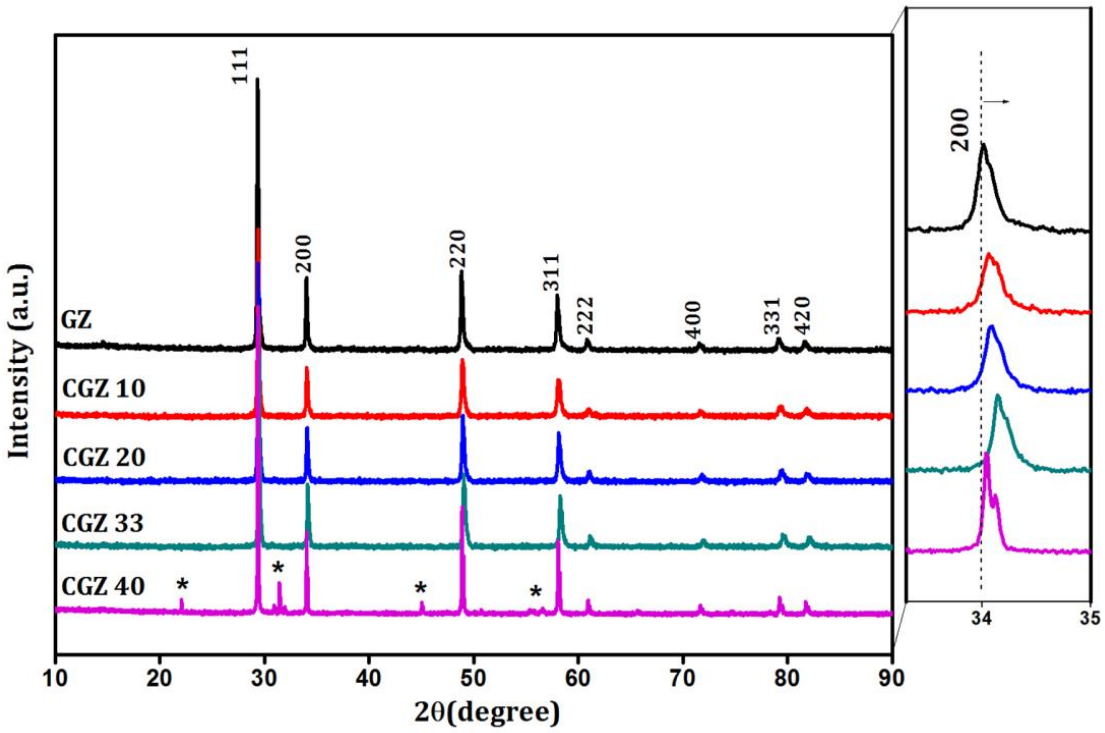

Figure 2-1: Powder X-ray diffraction patterns of various CGZ samples. Side panel shows the expanded view of the (200) reflection at ~34°

For a detailed analysis of the powder X-ray diffraction results, Rietveld simulation and refinement was carried out using commercially available X'pert Highscore plus software. The standard ICDD file matching the observed peak pattern and the stoichiometry proposed for the preparation of samples were used to construct starting models for the simulation and are listed in the Table 2-1. A pseudo-Voigt profile function was used to fit the diffraction pattern. The Caglioti parameters and asymmetry parameters determining the shape of diffraction peaks were refined along with the flat background polynomial and one of the coefficients. Various refined parameters from the best-fit output of Rietveld analysis are listed in Table 2-2.

Table 2-1: Starting model for Rietveld simulation of CGZ samples

Sample	GZ	CGZ 10	CGZ 20	CGZ 33
Space group	$Fm\bar{3}m$	$Fm\bar{3}m$	$Fm\bar{3}m$	$Fm\bar{3}m$
Lattice constant	5.2	5.2	5.2	5.2
Wyckoff positions:				
Ca	-	4a	4a	4a
Gd, Zr	4a	4a	4a	4a
O	8c	8c	8c	8c
Site Occupancy:				
Ca	0	0.026	0.056	0.100
Gd	0.500	0.474	0.444	0.400
Zr	0.500	0.500	0.500	0.500
O	0.875	0.870	0.860	0.850

Table 2-2: Refined values of various parameters from Rietveld analysis

Sample	GZ	CGZ 10	CGZ 20	CGZ 33
Phase	Fluorite	Fluorite	Fluorite	Fluorite
Unit cell	Cubic	Cubic	Cubic	Cubic
Space group	$Fm\bar{3}m$	$Fm\bar{3}m$	$Fm\bar{3}m$	$Fm\bar{3}m$
Lattice constant, *a* (Å)	5.26897(8)	5.26237(8)	5.25662(6)	5.24707(6)
Flat background	177.7967	159.2650	161.3220	160.8333
Coefficient 1	-28.3843	-1.1223	-5.4340	-4.9942
U	0.1545	0.3508	0.1099	0.1001
V	-0.0257	-0.0736	0.0245	0.0251
W	0.0074	0.0144	-0.0019	-0.0026
R_p (%)	6.58	6.70	6.10	6.10
R_{exp} (%)	6.85	7.43	7.37	7.36
R_{wp} (%)	8.76	8.87	7.87	7.96
GOF	1.63	1.42	1.13	1.16

It can be seen that the lattice parameter decreased progressively with increasing amount of $CaZrO_3$ added, as shown in Figure 2-2. This trend is counterintuitive considering the ionic radii of the various cationic species

involved. Under eight-coordination, as in the case of fluorite-type structures, the ionic radii of Ca^{2+}, Gd^{3+} and Zr^{4+} are 1.12 Å, 1.053 Å and 0.84 Å respectively [Shannon 1976]. The Ca ions can thus be assumed to occupy the Gd site due to their similar ionic radii. The introduction of larger Ca ions in place of Gd ions is expected to expand the lattice in accordance with Vegard's law [Vegard 1921] which is a commonly observed trend in many similar substitutions [Díaz-Guillén *et al.* 2009, Sayed *et al.* 2012, Xia *et al.* 2011]. Here in the present system, the decrease in the fundamental lattice vector of the system can be attributed to the Coulomb considerations when a trivalent cation is substituted by a divalent one. The condition of charge neutrality would require a few oxygen ions to be removed, in effect introducing anion vacancies in the lattice that would in turn lead to a lattice contraction.

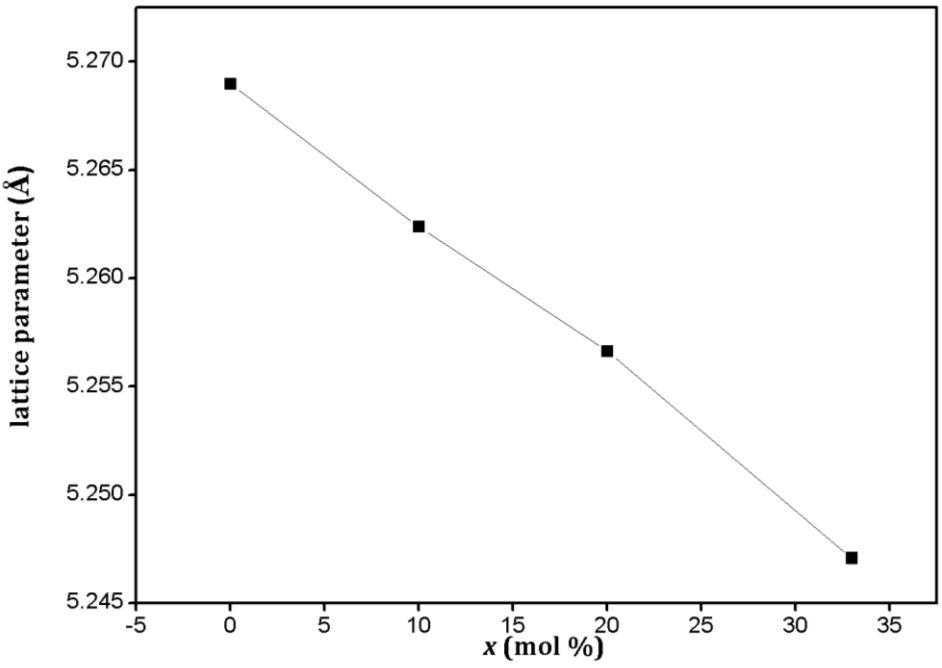

Figure 2-2: Variation of lattice parameter with mol% of $CaZrO_3$

From stoichiometry, it could be found that, for the upper limit of substitution (x = 33.3%), Ca ions occupy around 20% of the sites previously

occupied by Gd ions. Zr^{4+} ions are known to have a tendency to get coordinated by more than six oxygen ions and this in turn is reported as the reason for Zr-containing compositions to have a stronger tendency to form and retain a defect fluorite structure [Seifert *et al.* 1995]. A perovskite-type structure like $CaZrO_3$ has only six-coordinated B cations and so its formation as a secondary phase will not be favoured much. This makes it possible to add more Ca^{2+} to the lattice without the formation of secondary $CaZrO_3$ phase in this case, thereby increasing the vacancy concentration. Hence it could be inferred that the effect of oxygen vacancies is dominating over that of ionic size in determining the lattice volume of the present system, as was reported by Sayed *et al*. in a similar chemical system [Sayed, *et al.* 2012].

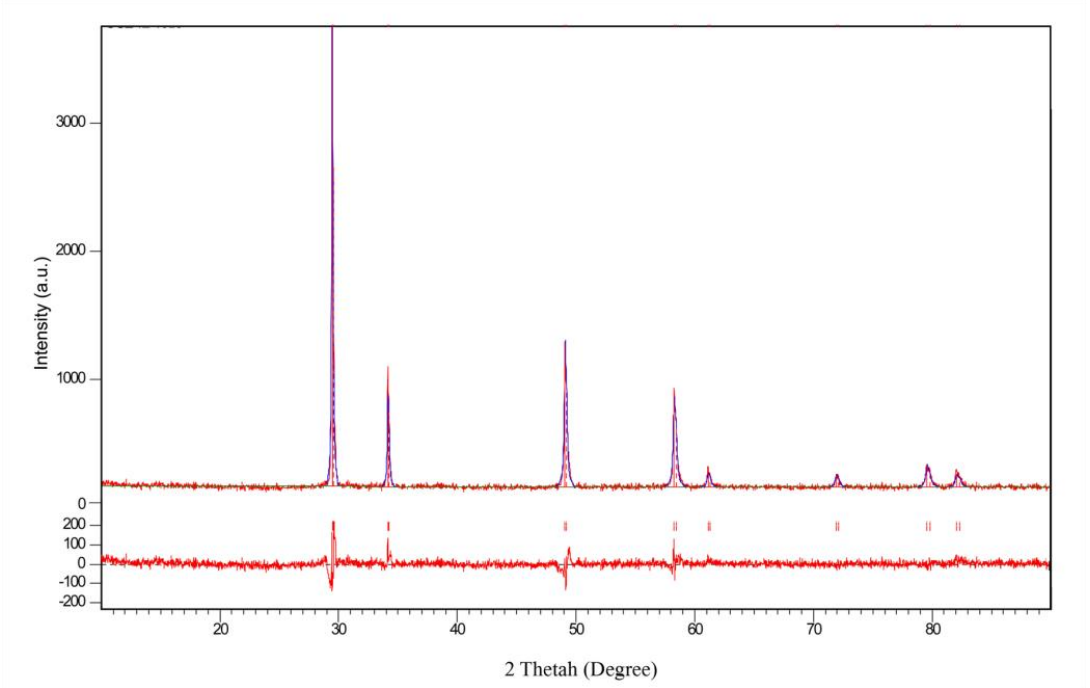

Figure 2-3: Graphical output of Rietveld analysis of representative sample CGZ 33

Beyond the solubility limit, the Ca ions tend to take part in the formation of $CaZrO_3$ secondary phase without creating oxygen vacancies in the lattice and hence the fluorite phase attains a larger lattice parameter. Although a good

Rietveld refinement for CGZ 40 could not be achieved due to the presence of $CaZrO_3$ impurity peaks, this can be qualitatively observed in Figure 2-1 where the (200) peak swerve away from the trend beyond 33%. The result of refinement of a representative sample (CGZ 33) along with the difference plot is shown in Figure 2-3 which shows that the refinement leads to good agreement between calculated and observed patterns.

2.3.2. Morphology

The morphology of the sintered pellets was analysed using scanning electron microscopy technique. The SEM images of the surfaces of various pellet samples are shown in Figure 2-4.

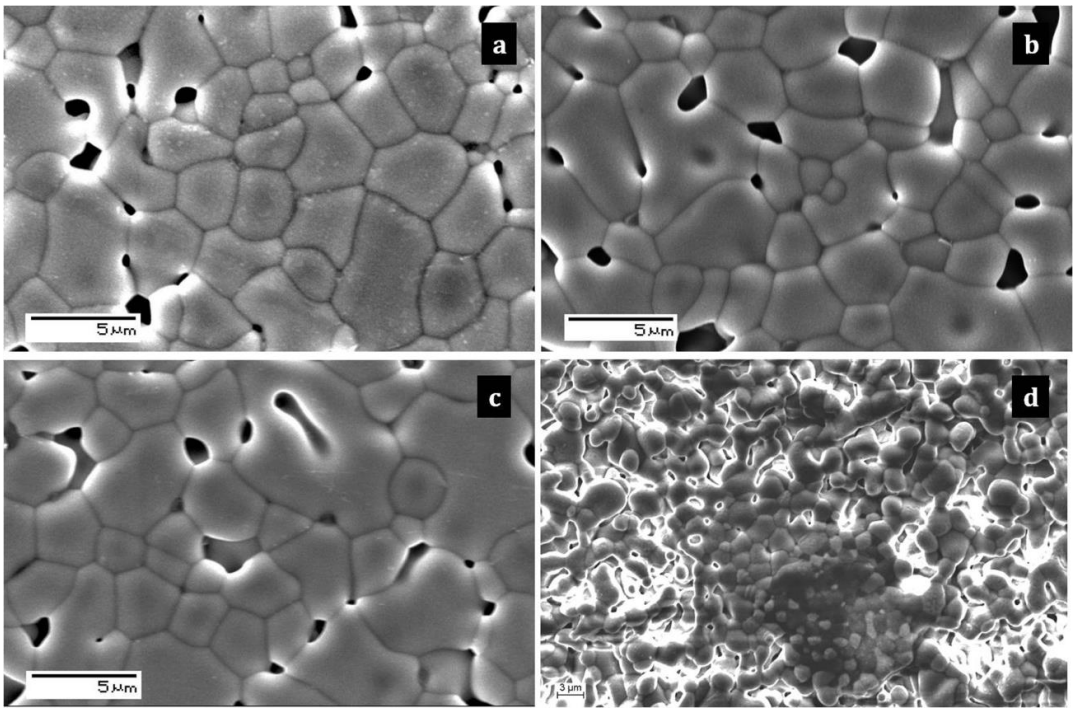

Figure 2-4: Scanning electron micrographs of the surface of various sample pellets (a) CGZ 10 (b) CGZ 20 (c) CGZ 33 (d) CGZ 40 (unpolished)

The polycrystalline samples are seen to possess grains that are typically in micrometer range of size. Surface of CGZ 40 shows regions that are slightly different in morphology from the surroundings. Distinct grain boundaries can

also be seen along with some amount of porosity. The bulk density of various samples were found to be around 82% of their theoretical densities.

The crystalline nature in small micro-domains can be observed with the aid of transmission electron microscopy whereas powder X-ray diffraction gives an idea about the average crystalline nature. The TEM images of the representative samples are shown in Figure 2-5.

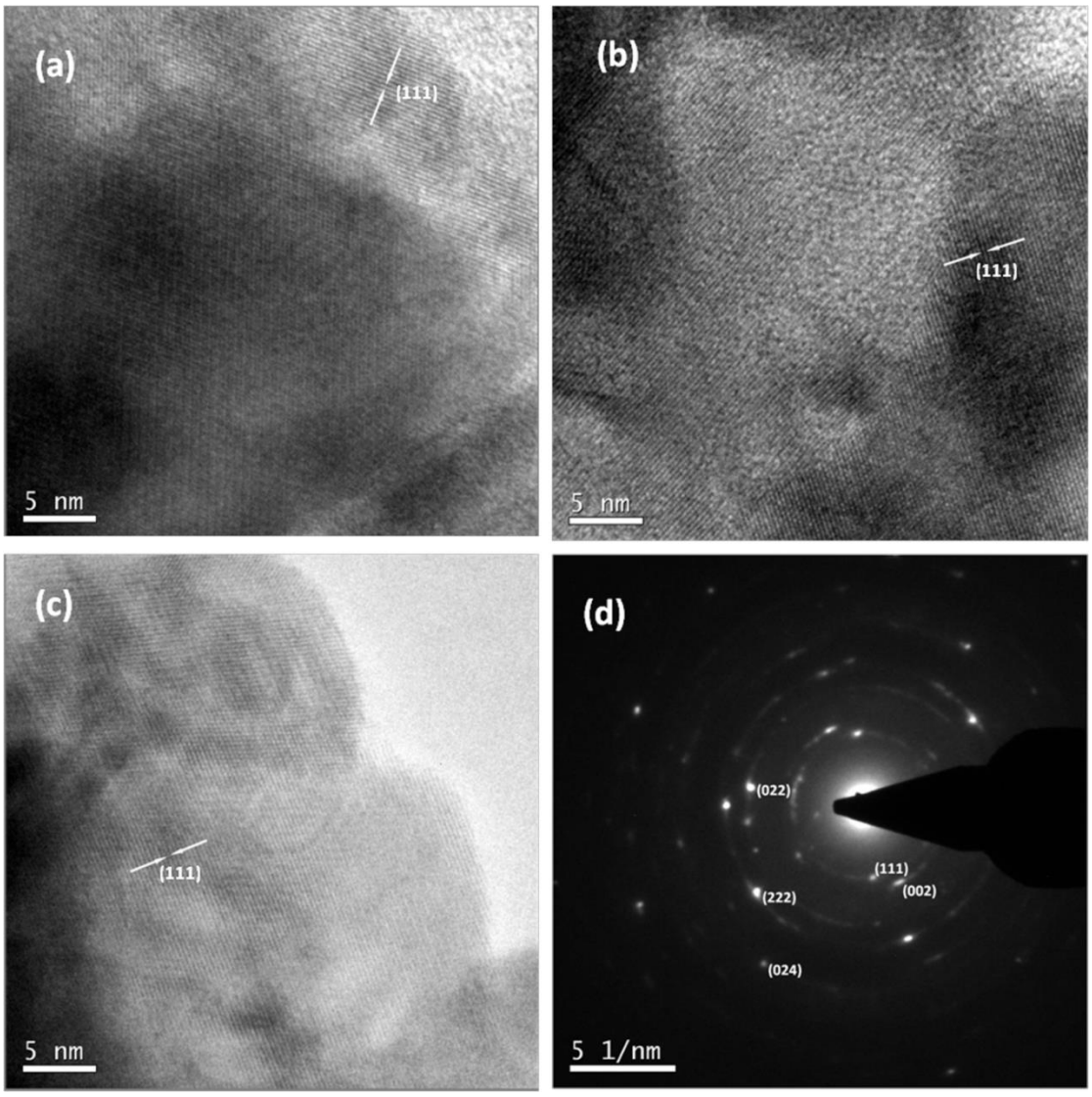

Figure 2-5: The high resolution TEM images of various samples sintered at 1923 K for 24 hours (a) CGZ 10 (b) CGZ 20 (c) CGZ 33 (d) SAED pattern of CGZ 33

The high resolution images of the lattice clearly showed the (111) Miller planes of a fluorite structure which have a spacing of 0.303 nm. The selected area electron diffraction (SAED) pattern of the representative sample (CGZ 33) showed diffraction rings characteristic of a typical polycrystalline material. The bright spots associated with the rings could be indexed with (002), (022), (222) and (024) Miller indices the planes corresponding to which could not be distinguished in the HR images of the morphology.

2.3.3. Thermal expansion

A study of response of a crystal lattice to change in temperature can throw light on to some more aspects of its structural characteristics.

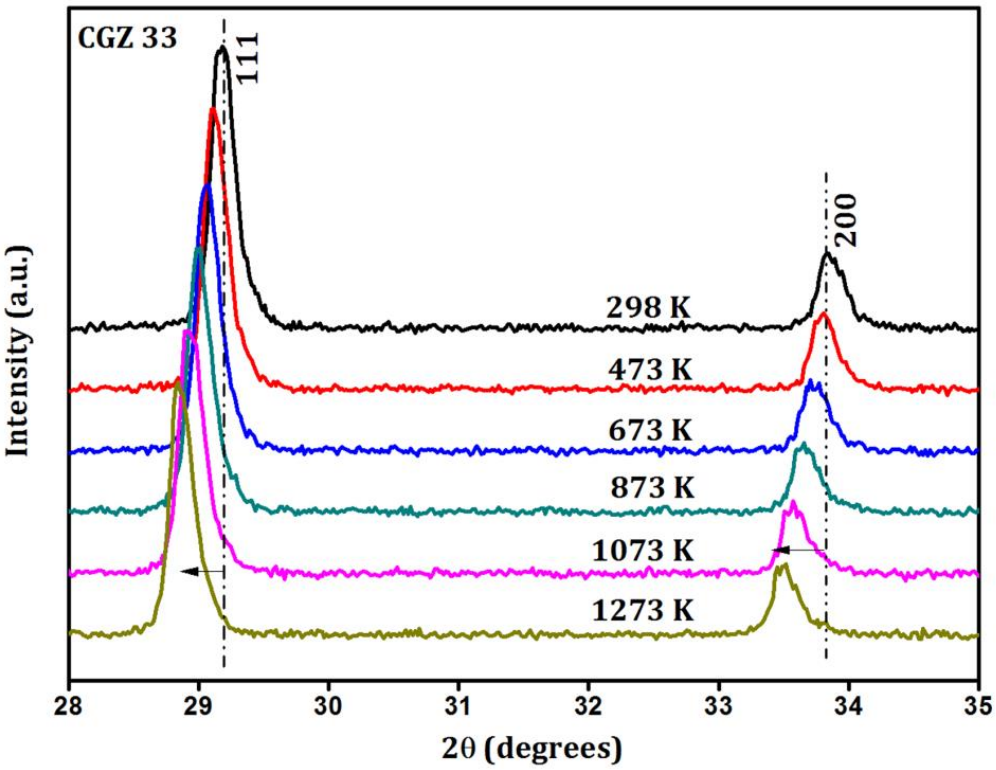

Figure 2-6: Powder XRD pattern of CGZ 33 at various temperatures (only two reflections being shown for legibility)

The lattice thermal expansion behaviour of the samples was studied by high-temperature X-ray diffraction in a temperature range from ambient

temperature to 1273 K at regular intervals of 200 K. The evolution of XRD pattern of a representative sample CGZ 33 with increase in temperature is shown in Figure 2-6. For legibility, only two peaks have been chosen to display. It can be observed that as the temperature increases, the reflections progressively move towards lower angles implying a corresponding expansion of the crystal lattice. It is to be inferred that all the samples showed the typical behaviour of a real anharmonic lattice wherein the pressure of the phonon gas is temperature dependant, which is the ultimate reason for thermal expansion. It could also be observed that all the samples retained their crystal structure at all temperatures without undergoing any temperature-induced structural transition.

The XRD patterns of each sample at all temperatures were analysed by Le-Bail fitting method carried out in commercially available X'Pert HighScore plus software and the values of lattice parameter were thus calculated from the fitting. The lattice parameter of each sample showed a linear increase with increase in temperature as was already evident in the qualitative inspection of their X-ray diffraction patterns. The lattice thermal expansion coefficients were calculated from the plots of lattice parameter against absolute temperature using the equation,

$$\alpha = \frac{1}{a_{298}} \frac{da}{dT} \, K^{-1} \tag{2.1}$$

Here α is the lattice thermal expansion coefficient, a_{298} is the value of lattice parameter at ambient temperature (298 K) and $\frac{da}{dT}$ is the slope of linear fit of increase in lattice parameter with increase in temperature. The variation of lattice thermal expansion coefficient is shown in Figure 2-7 where it can be seen that it increases with increase in mol percentage of $CaZrO_3$ present.

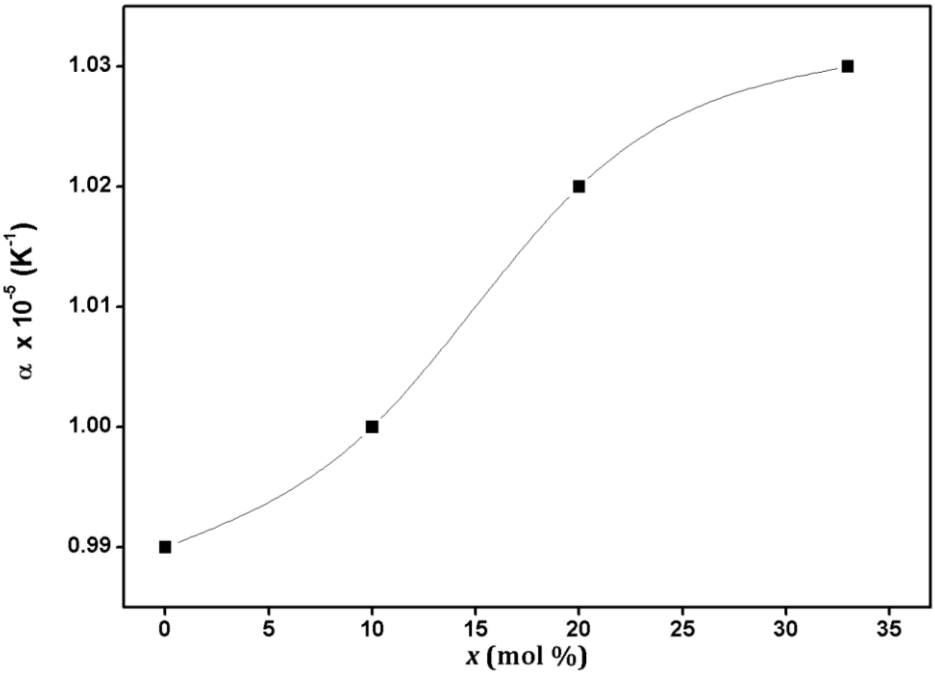

Figure 2-7: Variation of thermal expansion coefficient with mol% of $CaZrO_3$

It is widely reported that generation of oxygen vacancies is often accompanied by an increase in thermal expansion coefficient [Hayashi *et al.* 2000, J. W. Stevenson, *et al.* 2000, Masashi Mori, *et al.* 2000, Wang, *et al.* 2004]. The same can be assumed to be a crucial factor in deciding the trend seen in Figure 2-7 too, since the effect of oxygen vacancies has already been evident in the discussion on lattice parameter in an earlier section.

2.3.4. Electrical properties

The electrical characteristics were probed via ac impedance spectroscopy technique by investigating the response of sintered pellets to a small ac stimulus (100 mV). The real and imaginary parts of ac impedance as a function of frequency was measured in the temperature range of 473 K to 1023 K and a frequency range of 1 Hz to 1 MHz. The sintered pellets had a density of around 85% of the theoretical density. The typical semicircle response of CGZ 33 for the impedance function is shown in Figure 2-8. Two distinct semi-circular arcs

could be observed for all the samples in intermediate temperatures, each of them corresponding to two different mechanism of ionic transport within the material.

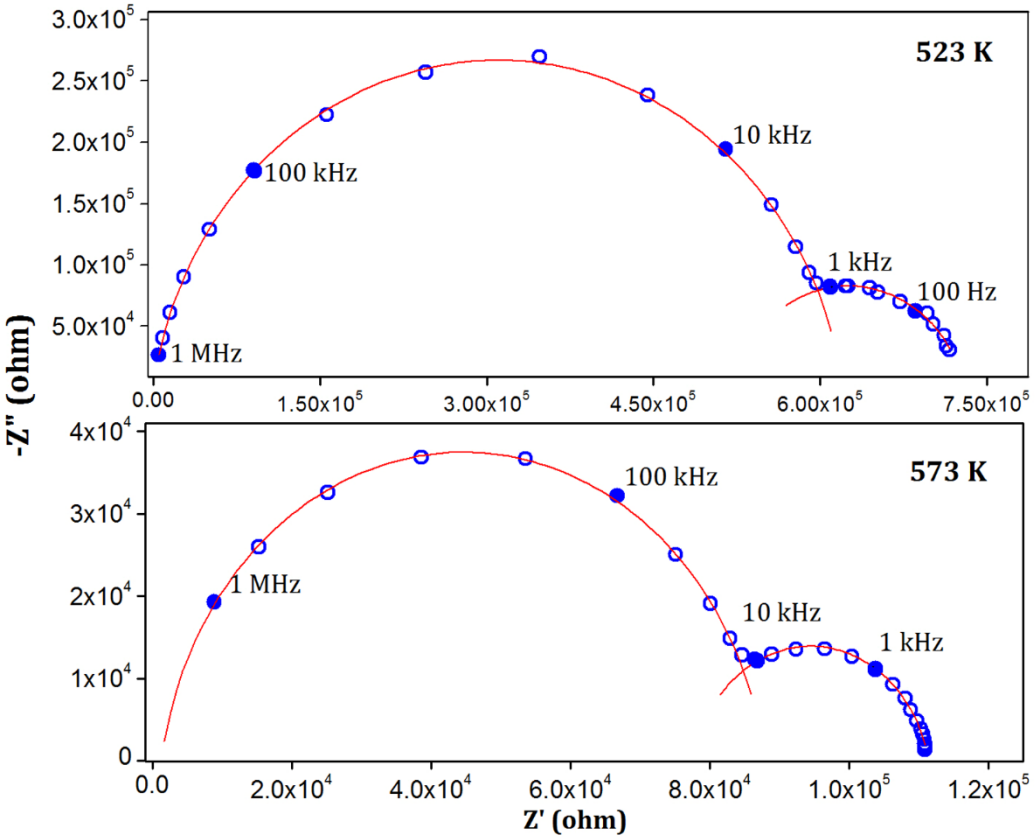

Figure 2-8: Complex plane representation of ac impedance of CGZ 33 at two temperatures

By calculating the capacitance associated with a particular arc, we can have an idea about the mechanism responsible for it. At the grain boundaries, where there is larger probability of charges being accumulated, the capacitance typically falls in the nanofarad (*nF*) range and within the grains it is only in picofarads (*pF*) [Liu, *et al.* 2010]. The intercepts of the arcs with the real axis would yield the value of resistance, R from which the conductivity of the materials can be calculated using the relation,

$$\sigma = \frac{l}{RA} \qquad (2.2)$$

where σ is the conductivity, *l* is the thickness of the pellet and A is the electroding surface area. At higher temperatures mostly only a vertical spike could be seen making it difficult to resolve the bulk and grain boundary contributions. This is a typical behaviour for ionic conducting materials and is a result of the high electrode blocking capacitance which usually falls in the microfarad region [Huggins 2002, Kotobukia *et al.* 2010, Rangasamy *et al.* 2012, Sumaletha Narayanan 2011]. Hence only the total resistance which is the sum of grain and grain boundary resistances was considered to derive the values of conductivity.

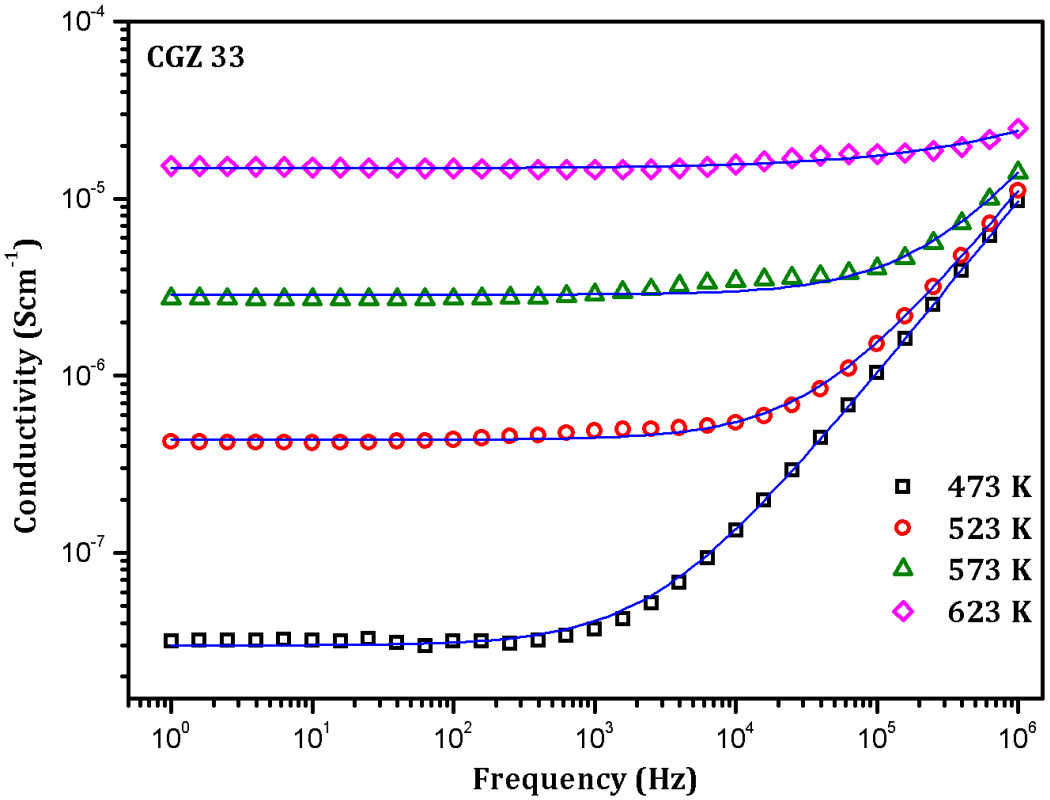

Figure 2-9: Dispersion of ac conductivity of CGZ 33 at different temperatures

Figure 2-9 shows the variation of ac conductivity of CGZ 33 with the applied frequency for a few different temperatures. The plots are characterized by the presence of a frequency-independent plateau and a frequency-dependant

positive slope region of conductivity dispersion. This can be found to obey the Jonscher's power law equation [Jonscher 1977] expressed as,

$$\sigma(\omega) = \sigma_0 + A\omega^n \tag{2.3}$$

where σ_0 is the frequency-independent conductivity (dc conductivity), A is a temperature-dependent constant determined by the strength of polarizability, and n ($0 \leq n \leq 1$) is a constant that depends on the degree of interaction between the mobile ions and the lattice and also on the temperature. This trend of conductivity is an indication that the conduction mechanism in these materials is through the hopping of ions presumably through the vacant sites introduced in the lattice. It can be seen that the frequency at which dispersion begins to dominate shifts towards higher frequencies when the temperature increases. This may be correlated with the jump relaxation model, according to which the increase in hopping frequency of the carrier species with increase in temperature causes the dispersion to dominate in higher frequencies [Funke 1997, Kumar Baral and Sankaranarayanan 2010].

Although the frequency dependent properties of a solid can be expressed in terms of many parameters, complex impedance (Z^*) and the electric modulus (M^*) are generally preferred for materials showing more long range conductivity than dielectric behaviour. Electric modulus is the inverse of dielectric permittivity (ε^*) and can be expressed as,

$$M^* = j\omega C_0 Z^* = M' + jM'' \tag{2.4}$$

where C_0 is the capacitance, Z^* is the complex impedance, $M'$and M'' are the real and imaginary components of the electric modulus respectively [Kumar Baral and Sankaranarayanan 2010].

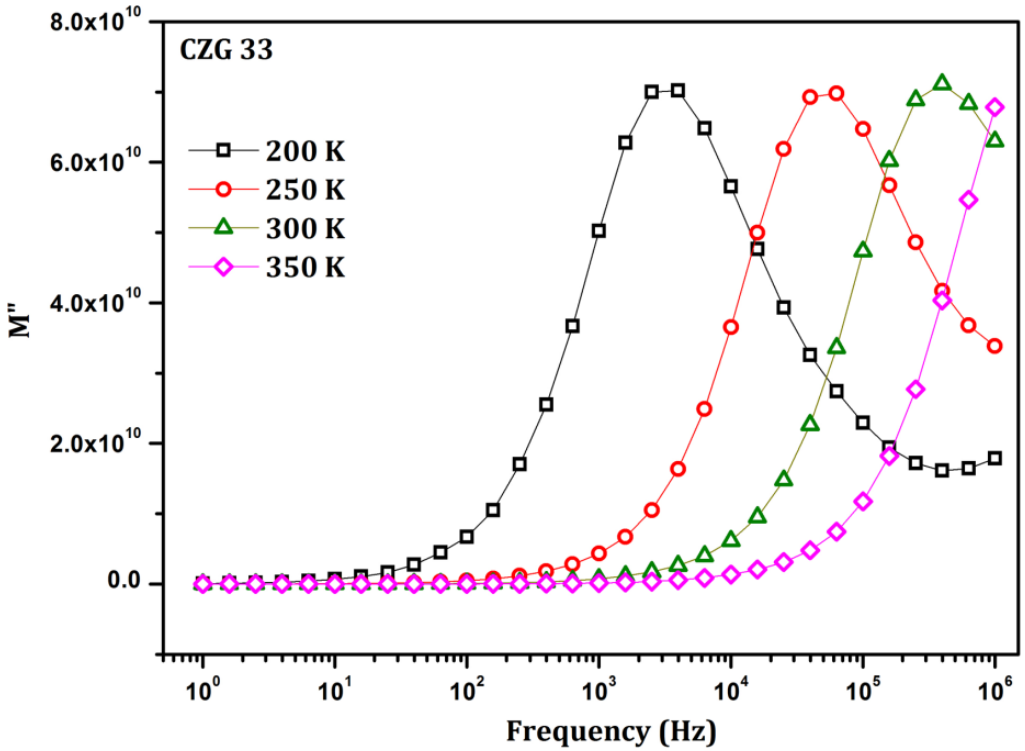

Figure 2-10: Relaxation of imaginary part of the electric modulus at different intermediate temperatures

Figure 2-10 shows a plot of imaginary part of electric modulus against frequency. At the low frequency region, value of modulus tends to be zero for all temperatures since it does not receive any significant contribution from the electrode polarization effect. *M"* also shows characteristic peaks at a particular frequency which shifts towards higher frequencies as the temperature is increased. A peak in any dielectric function with respect to frequency is an indication of a relaxation behaviour, the position of which would depend on which function we choose to plot [Andrew 1999]. This behaviour is a commonly reported one in oxide ionic conductors [A. K. Baral 2009, Baral and Sankaranarayanan 2009, Sarkar and Nicholson 1989] and can be attributed to the charge re-orientation relaxation of ions involving the vacancies. The shift of this peak towards high frequencies with increase in temperature indicates that the

process is thermally activated, the same being also apparent in the decrease in radii of the complex impedance arcs with increase in temperature. Thus the thermally activated ion hopping process can be thought to be responsible for the overall conductivity of these materials.

The temperature dependence of the total conductivity is usually described by the Arrhenius equation,

$$\sigma = \frac{\sigma_0}{T} \exp\left(-\frac{E_a}{kT}\right) \qquad (2.5)$$

where σ is the conductivity, σ_0 is the pre-exponential part corresponding to the availability of effective charge carriers in the system, E_a is the activation energy for the thermally activated conduction, T is the absolute temperature and k is the Boltzmann constant.

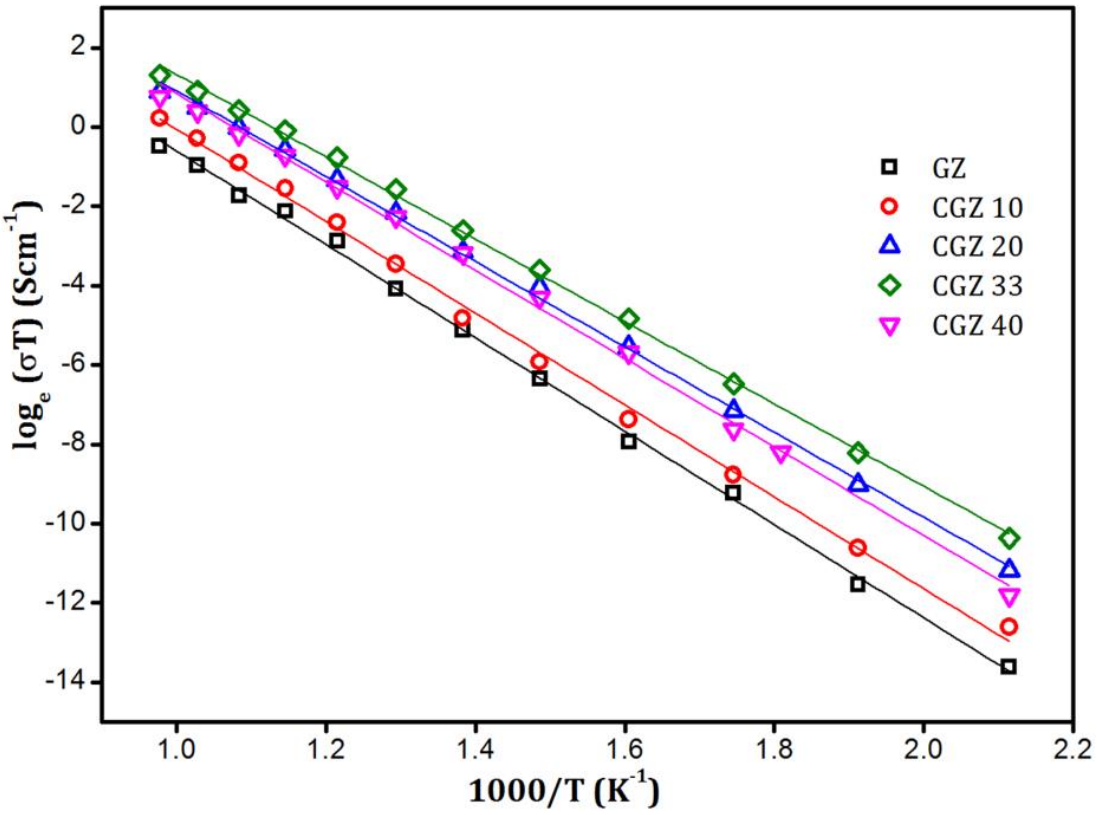

Figure 2-11 Arrhenius plots of various samples along with their linear fits

Figure 2-11 shows a plot of $\log_e(\sigma T)$ against 1000/T, the straight lines being the least squares mathematical fits of the points. These straight line fits show the correspondence of conductivity data with the linearized form of the Arrhenius equation and it delineates the fact that the conduction mechanism in the present study is a thermally activated one. The activation energy can be deduced from the slopes of the Arrhenius fits. Variation of conductivity at 1023 K and the activation energy plotted against the mol% of $CaZrO_3$ is shown in Figure 2-12 and Figure 2-13 respectively. With an increase in *x*, the activation energy for conduction decreases resulting in an almost linear increase of conductivity up to *x* = 33.3%. Beyond this limit the activation energy increases and the conductivity decreases. This shows that the conducting property is enhanced by the oxygen vacancies introduced in the lattice by the Ca ions thereby providing a lower energy barrier for the ionic diffusion.

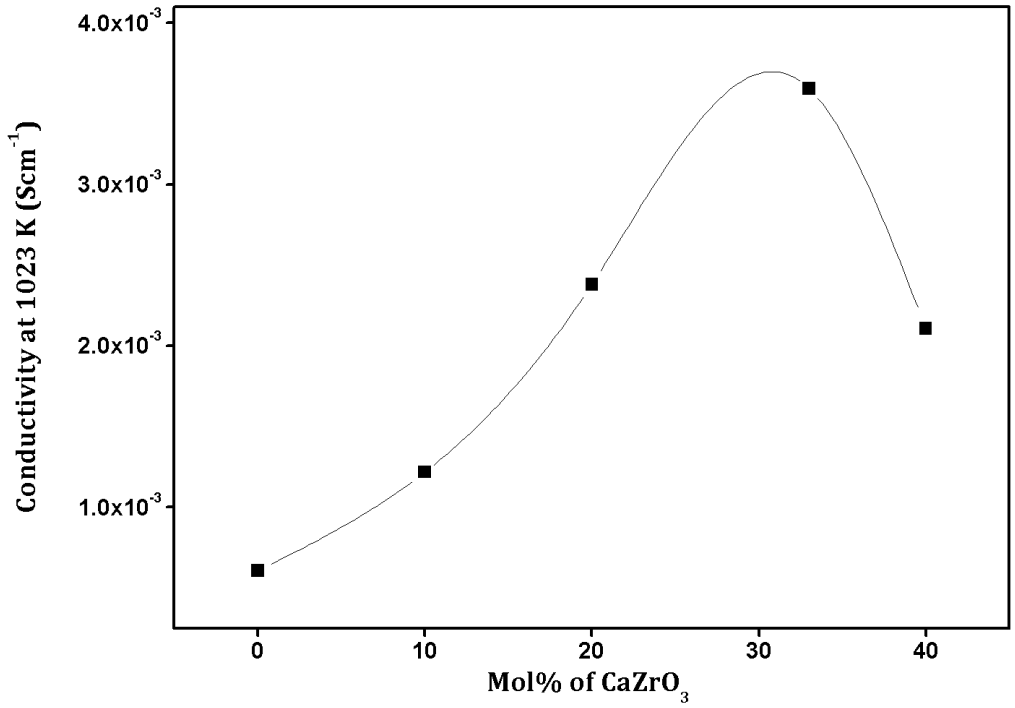

Figure 2-12: Variation of conductivity at 1023 K with mol% of $CaZrO_3$

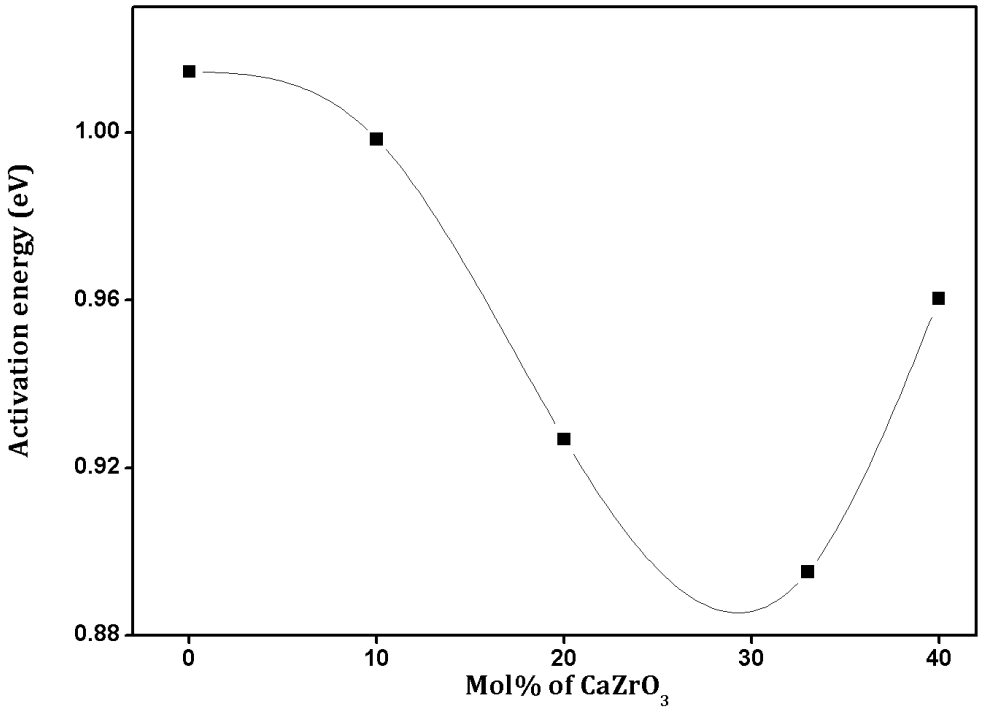

Figure 2-13: Variation of activation energy with mol% of $CaZrO_3$

The setback in enhancement in conductivity beyond a limit can be attributed to the presence of poorly conducting $CaZrO_3$ secondary phase which would create a higher energy barrier as implied by the increase in activation energy for x = 40%. The maximum value of conductivity obtained in this study is 3.59×10^{-3} Scm^{-1} at 1023 K.

2.4. Conclusion

$CaZrO_3$-$Gd_2Zr_2O_7$ solid solutions were crystallized into a cubic fluorite structure. The effect of substitution was to create oxygen vacancies within the lattice that lead to a progressive contraction in the lattice parameter, dominating over the effect of difference in ionic radii. The increase in thermal expansion coefficient also implied the dominance of oxygen vacancies. The thermally activated conduction process in these materials was found to follow Arrhenius behaviour and an analysis of dielectric functions was found to indicate an ionic

hopping mechanism leading to long range conductivity. The ionic conductivity was enhanced by the substitution due to the lower energy barriers introduced by the oxygen vacancies towards the charge transport. Presence of $CaZrO_3$ secondary phase was seen to be detrimental to conduction process and thus within the limit of solubility, $CaZrO_3$ enhances the electrical conductivity of $Gd_2Zr_2O_7$.

CHAPTER 3

****

Influence of Aliovalent Cation Substitution on Structural and Electrical properties of $Gd_2(Zr_{1-x}M_x)_2O_{7-\delta}$ (M = Sc, Y) system

****

Independent substitutions by two cations in compositions of the form $Gd_2(Zr_{1-x}M_x)_2O_{7-\delta}$ (M = Sc and Y; x = 0, 0.1, 0.2, 0.3, 0.4) were investigated. Despite being in the same group of elements, the two substituent cations introduced oxygen vacancies with contrasting influence on the parent lattice and ionic conductivity. Larger ionic radius of Y^{3+} forced the lattice to expand which along with the increased anion defects lowered the energy barrier for charge transport enhancing the ionic conductivity. Whereas, in Sc-substituted compositions, oxygen vacancies dominated over ionic size causing the lattice to contract and their cooperative behaviour turned out to be disadvantageous for long range conduction process. The changes in rigidity of the inter-ionic bonds and the lattice volume introduced by the substituent cations also influenced the thermal expansion of the materials. This demonstrates that the influence of oxygen vacancies on the ionic conductivity is also dependent on the size of aliovalent substituent ion.

Vaisakhan Thampi D. S., Prabhakar Rao Padala, Renju U. A., "Influence of Aliovalent Cation substitution on structural and electrical properties of $Gd_2(Zr_{1-x}M_x)_2O_{7-\delta}$ (M = Sc, Y) system", ***RSC Advances***, 5, 88675 – 88685 (2015)

3.1. Introduction

On the backdrop of diminishing energy resources, a quest for efficient solid oxide electrolyte materials to be used for fuel cell applications have been going on since the last few decades. Electrolyte is the heart of a solid oxide fuel cell [Carrette*, et al.* 2001]. Since fuel cells constitute a promising category of non-conventional energy resources, material development for them, especially electrolytes, has gained much attention [Badwal and Foger 1996, Figueiredo and Marques 2013]. The electrolyte materials should possess some specific features like high electrical conductivity, adequate thermal and mechanical properties like strength, creep*, etc.*, thermodynamic and structural stability [Badwal and Ciacchi 2000]. Apart from this, properties like thermal expansion should match with the other fuel cell components, which poses limitations in changing to completely new ceramic systems [Carrette*, et al.* 2001].

Various zirconate ceramics having a general formula $A_2B_2O_7$ have been studied extensively in this respect wherein attempts to enhance the electrical properties have been made by means of substitution or addition of foreign cations in already known chemical systems [Burggraaf *et al.* 1981, Kutty *et al.* 1995, Pirzada *et al.* 2001, van Dijk *et al.* 1985, Wilde and Catlow 1998]. These zirconate compositions mostly crystallize in either a pyrochlore-type or a fluorite-type lattice depending on the difference in size between the two cations [Shimamura *et al.* 2007]. The larger the ionic size difference, higher will be the structural order within the lattice and the ordering or disordering transitions between the two structures induced by cation-substitution are found to have considerable influence on the electrical properties of these compounds [Radhakrishnan*, et al.* 2011, Subramanian *et al.* 1983, Vaisakhan Thampi *et al.* 2014]. Among the various zirconate systems reviewed, $Gd_2Zr_2O_7$ is reported to be one of the best with respect to the electrical characteristics [Liu *et al.* 2009,

Xia*, et al.* 2011, Xia*, et al.* 2010]. It is known to exist both in fluorite and pyrochlore structures with various preparation conditions [Lee*, et al.* 2009]. There have also been many attempts to tailor the properties of this chemical system with varying results, some being positive and some negative [Liu*, et al.* 2010, Liu*, et al.* 2008, Liu*, et al.* 2009, Xia*, et al.* 2011, Xia*, et al.* 2010, Zhan-Guo *et al.* 2009]. Substitution of Gd^{3+} by Sm^{3+} and then co-substitution by Ca^{2+} had positive effects on the properties of parent composition [Liu*, et al.* 2012, Liu*, et al.* 2008]. Substitution by Eu^{3+} also was helpful for improved electrical properties [Xia*, et al.* 2010]. Nb^{5+} while substituting Zr^{4+} led to an enhancement in the electrical conductivity whereas Ce^{4+} and Mo^{6+} in that place were found to bring it down [Liu*, et al.* 2010, Xia *et al.* 2010, Xia*, et al.* 2011]. In most of these studies, there were certain optimum levels of substitution that corresponded to the maximum value of conductivity, which depended on many other factors like lattice order, lattice volume, point defects, *etc.* Thus, despite extensive attempts, there does not exist any general rule that can guide to the best direction to achieve desired properties.

Since defect-fluorite structures involve more than one type of cations, they can inherently contain some amount of order. Most of the aforementioned substitution attempts are focused on the A-cation site. Here in the present work two cations, Sc^{3+} and Y^{3+}, were independently chosen to substitute the Zr^{4+} partially in the B-site of $Gd_2Zr_2O_7$. The differences in ionic size can influence the crystal order and the lattice volume. That, along with the difference in valence, was expected to influence various physical properties. Crystal structure and electrical properties were given prime focus in the present investigation. The independent substitution would help to contrast between ions and to understand the various mechanisms distinctly.

3.2. Experimental

Solid solutions of general formula $Gd_2(Zr_{1-x}M_x)_2O_{7-\delta}$ (M = Sc, Y; x = 0, 0.1, 0.2, 0.3, 0.4) were prepared. Conventional solid state reaction route involving choice of oxides of the cations as reactants and wet mixing followed by heat treatment was adopted for the synthesis of the samples. Homogenous mixture of Gd_2O_3 (Aldrich, 99.9%), ZrO_2 (Aldrich, 99%), Sc_2O_3 (Alfa Aesar, 99.99%) and Y_2O_3 (Sigma-Aldrich, 99.99%) weighed according to stoichiometry was calcined at 1573 K and recalcined at 1873 K, both for 6 h each. The product powders were then made to green pellets with a hydraulic press applying uniaxial compaction at 2.5 MPa. The pellets were then sintered at 1923 K for 24 h.

The prime tool to investigate structural features was an X-ray diffractometer (X'Pert Pro, PANalytical) making use of Cu-Kα radiation of wavelength 1.54 Å. The diffractograms were recorded in a 2θ range of 10° to 90°. FT-Raman spectra of samples were obtained by exciting with an argon laser of wavelength 784 nm using a Labram HR 800 spectrometer (Horiba Scientific). Morphological features were examined through electron microscopic technique, namely a scanning electron microscope (SEM, model: JEOL JSM-5600LV) and a transmission electron microscope (TEM, TECNAI 30G2 S-TWIN, the Netherlands), which were also helpful in confirming the crystallinity of prepared samples. The response of the crystals to high temperature was analysed through high-temperature X-ray diffraction (Anton-Paar High-temperature attachment to XRD). Impedance spectroscopy was used to probe the electrical properties. Cylindrical pellets were subjected to two-point impedance measurement using an impedance analyser (Solartron SI 1260) through a dielectric interface (Solartron 1296). Electroding was done at polished end-faces painted with silver-paste and the measurement frequency was varied from 1 MHz to 1 Hz, in a temperature range of 473 K to 1023 K.

3.3. Results and Discussion

In coming sections, the Sc^{3+} and Y^{3+} substituted samples of the form $Gd_2(Zr_{1-x}M_x)_2O_{7-\delta}$ (M = Sc, Y; x = 0, 0.1, 0.2, 0.3, 0.4) will be respectively labelled with the codes GZS and GZY with a numeral representing the value of x for each sample. GZ will stand for $Gd_2Zr_2O_7$.

3.3.1. Crystal structure

3.3.1.1. X-ray diffraction

Powder X-ray diffraction was made use of to understand the maximum feasibility of solid solution formation and to analyse the crystal structure of the synthesized materials. Sharp X-ray reflections could be seen in the recorded diffraction pattern that indicated the crystalline nature of the samples. A comparison with standard ICDD powder pattern No. 01-080-0471 showed that all the single phase compositions crystallized in a cubic fluorite-type structure with $Fm\bar{3}m$ space group.

In the cubic fluorite-type crystals, the cations constitute a face centered lattice and are cubically coordinated by eight anions. The anions, whereas, are coordinated by four cations which form a tetrahedron about each of them. The crystallographically different lattice positions are designated by Wyckoff notations 4*a* (0, 0, 0) and 8*c* (0.25, 0.25, 0.25) occupied respectively by cations and anions. In $Gd_2Zr_2O_7$, which is considered to be a defect fluorite-type crystal, the Gd and Zr ions are disordered over an FCC lattice. The XRD patterns of the $Gd_2(Zr_{1-x}M_x)_2O_{7-\delta}$ compositions are shown in Figure 3-1 and Figure 3-2. It could be observed that the $Gd_2Zr_2O_7$ lattice accommodated the aliovalent M ion (M = Sc^{3+}, Y^{3+}) in the Zr^{4+} site to a fairly good extent of x = 0.3. Although both Sc^{3+} and Y^{3+} showed maximum solubility in solid solution formation at x = 0.3, a close observation of the peak patterns showed that the overall influence the substitution had on the crystal structure was different from one another.

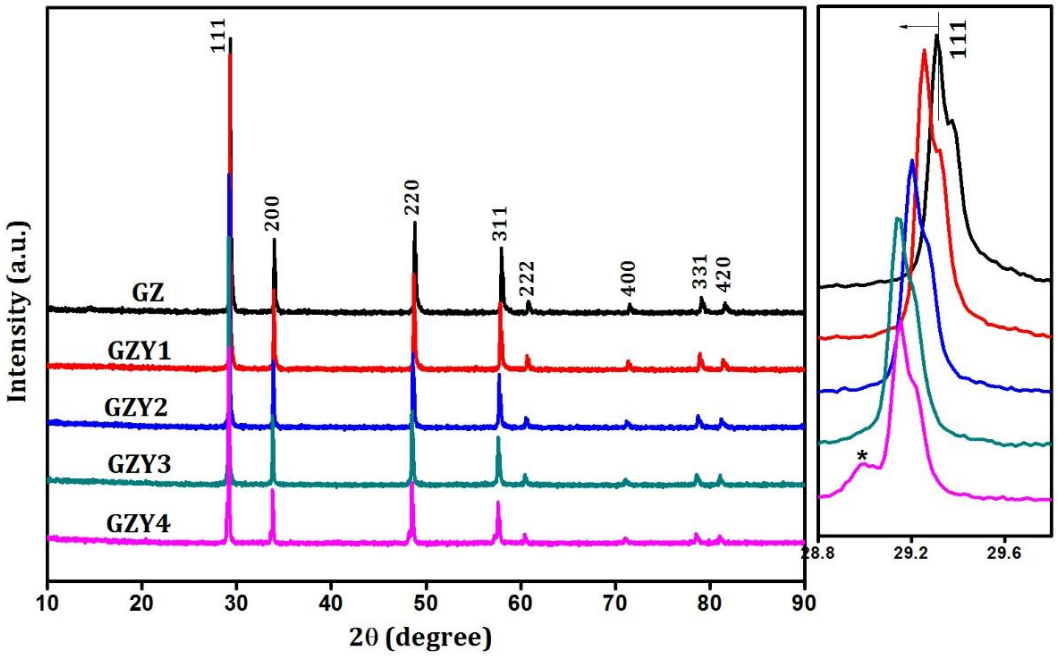

Figure 3-1: Powder X-ray diffraction patterns of $Gd_2(Zr_{1-x}Y_x)_2O_{7-\delta}$. Side panel shows the expanded view of (111) peak.

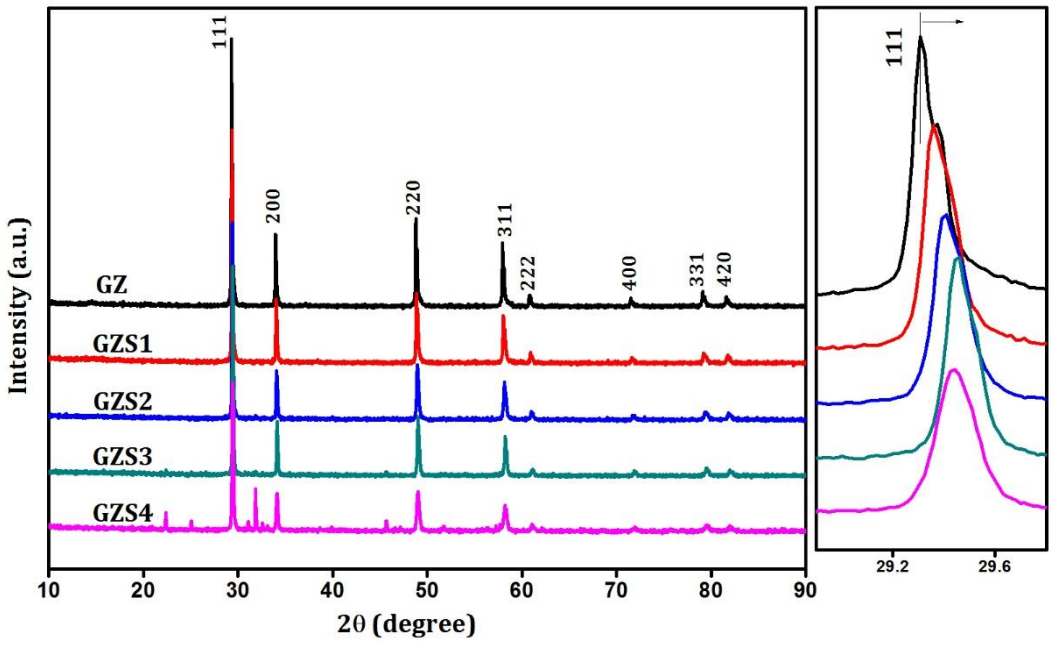

Figure 3-2: Powder X-ray diffraction patterns of $Gd_2(Zr_{1-x}Sc_x)_2O_{7-\delta}$. Side panel shows the expanded view of (111) peak.

With substitution of Zr^{4+} by Y^{3+}, the X-ray reflections were found to shift towards lower angles as seen in the side panel of Figure 3-1, indicating an increase in the interplanar spacing of various miller planes. But the trend observed for substitution by Sc^{3+} was different, and there the reflections moved towards higher angles (as in Figure 3-2) with increasing amount of substitution. In both cases there was no appreciable change in the width of diffraction peaks.

A more detailed and quantitative analysis of the XRD data was carried out by Rietveld simulation and refinement method using commercially available X'pert Highscore plus software. A standard peak-matching procedure with the ICDD crystal structure database helped constructing starting models for pattern simulation, with the stoichiometry providing an intuitive idea about the ionic occupancies. Fitting of diffraction peaks demanded a pseudo-Voigt line profile function which is essentially a linear combination of Gaussian and Lorentzian functions. The Caglioti parameters, flat background and two background function coefficients were chosen for refinement along with the unit cell identities. Various refinement parameters including the agreement indices are listed in Table 3-1.

It can be observed from the result of Rietveld refinement that the influence on the fundamental lattice vector of the $Gd_2Zr_2O_7$ lattice is different for Sc and Y ions. While considering the lattice volume in substitution processes, the most commonly reported influence comes from the radius of the substituent ion. According to Vegard's law[Vegard 1921], a larger ion substituting a smaller ion is expected to increase the lattice volume and vice versa. The ionic radii of Gd^{3+}, Zr^{4+}, Sc^{3+} and Y^{3+} under the eight-coordination condition in a fluorite type lattice are 1.053 Å, 0.84 Å, 0.87 Å and 1.019 Å respectively.[Shannon 1976] Although both these substituent cations are larger in radius than Zr^{4+}, substitution by Sc^{3+} decreases the effective lattice parameter while substitution by Y^{3+} increases it.

Table 3-1: Refined parameters from Rietveld analysis

Sample	**GZ**	**GZY1**	**GZY2**	**GZY3**	**GZY4**	**GZS1**	**GZS2**	**GZS3**
Unit cell	Cubic	Cubic	Cubic	Cubic	Cubic	Cubic	Cubic	Cubic
Space group	$Fm\bar{3}m$	$Fm\bar{3}m$	$Fm\bar{3}m$	$Fm\bar{3}m$	$Fm\bar{3}m$	$Fm\bar{3}m$	$Fm\bar{3}m$	$Fm\bar{3}m$
Flat background	186.9829	194.1553	177.678	179.4647	161.7568	176.7341	166.3954	168.047
Coefficient 1	-21.3647	-26.3029	-24.3479	-26.1509	-17.2779	-30.1538	-28.4476	-29.2692
Coefficient 2	22.45977	23.73738	34.15881	34.80234	35.35935	30.7739	25.92725	26.53172
Scale Factor	0.000181	0.000187	0.000158	0.000161	0.000133	0.000181	0.000175	0.000164
Lattice parameter [Å]	5.2729(1)	5.2831(1)	5.2932(1)	5.3011(1)	5.3028(2)	5.2659(1)	5.2581(1)	5.2516(1)
U	0.035581	0.0379	0.057153	0.142995	0.082256	0.097383	0.093578	0.056999
V	-0.0019	-0.00205	-0.00735	-0.06603	-0.02238	-0.02184	0.017424	0.016612
W	0.003596	0.003063	0.004667	0.013923	0.006291	0.007278	-0.00019	0.001149
Peak Shape 1	0.875262	0.651668	0.510645	0.661708	1.031867	0.587736	0.478828	0.195308
Peak Shape 2	0.00502	0.006852	0.007872	0.00552	0.003654	0.007718	0.007572	0.012047
R_p	6.45	6.23	6.15	6.02	6.91	6.04	5.48	5.84
R_{exp}	6.76	6.63	6.88	6.84	7.21	6.89	7.15	7.13
R_{wp}	9.2	8.65	7.93	7.64	8.97	7.9	7.01	7.43
GOF	1.87	1.7	1.32	1.24	1.54	1.31	1.96	1.08

For Y^{3+} substitution, the incorporation of larger ions into the 4*a* sites previously occupied by smaller Zr^{4+} ions forces the lattice to expand. This is evident in Figure 3-3 where there is a linear increase in the lattice parameter with increase in Y^{3+} substitution. For the GZY4 sample, the peak is seen to swerve from this trend. This may be because, beyond the limit of solubility, substituent ions tend to form other impurity phases without causing much strain to the parent lattice. The last data point of the lattice parameter plot in Figure 3-3 illustrates this, where the increase in lattice parameter beyond $x = 0.3$ is comparatively very less.

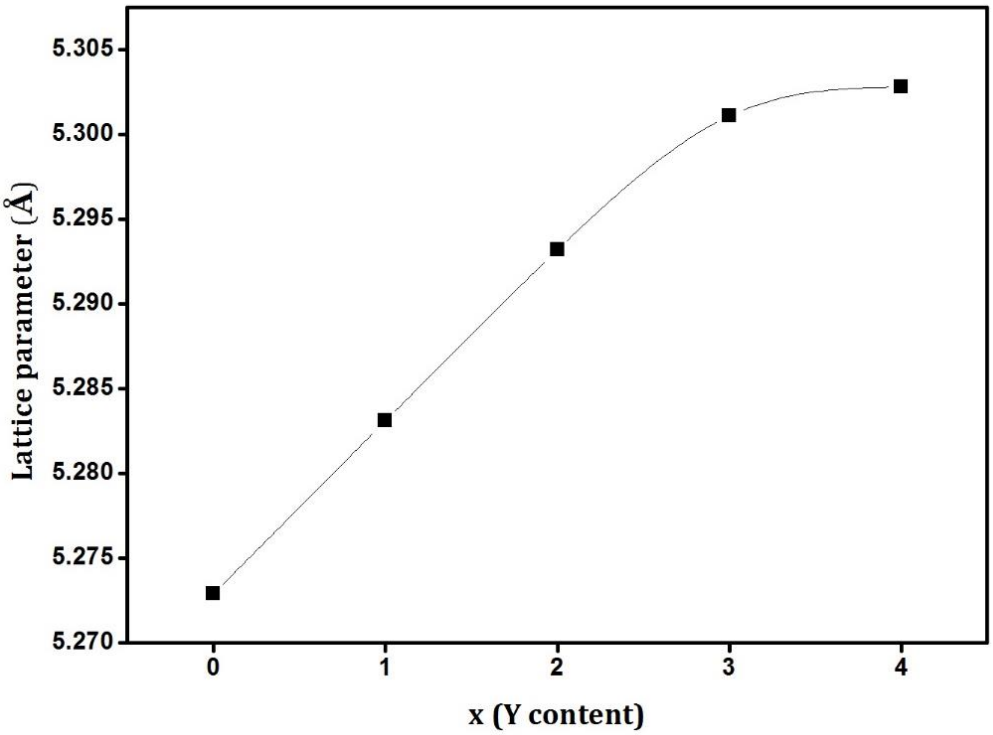

Figure 3-3: Variation of lattice parameter with substitution for GZY series

On the contrary, the lattice parameter is decreasing substitution by Sc^{3+} as evident in Figure 3-4. This may be attributed to the effect of Schottky defects in the anionic sublattice caused by aliovalent substitution. When tetravalent Zr is

substituted by trivalent Sc, oxygen vacancies will be created in the lattice for electrostatic balance.

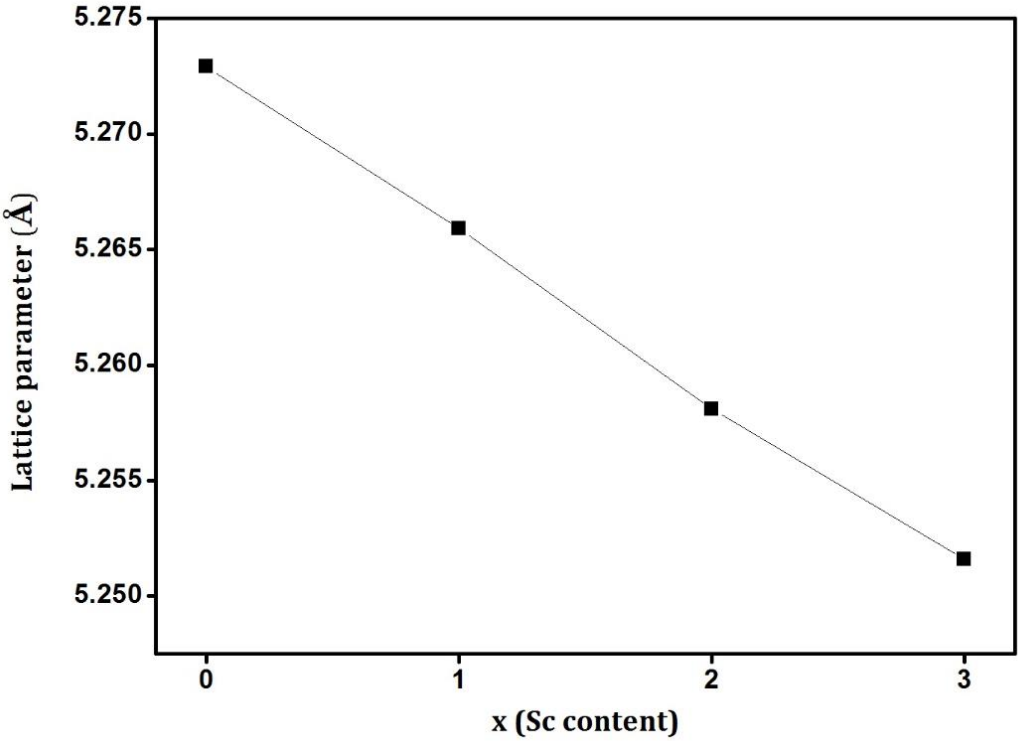

Figure 3-4: Variation of lattice parameter with substitution for GZS series

Substitution of every two Zr ions will create one oxygen vacancy in the vicinity, and can be represented in Kroger-Vink notation as

$$2Zr^{4+} \rightarrow 2M^{3+} + V_o'' \qquad (3.1)$$

This will reduce the average coordination number of the 4*a* site cation which is 8 for an ideal fluorite-type lattice. Marrochelli *et al*. established through molecular dynamics simulation and a meta-analysis of literature that the size of an oxygen vacancy is smaller than an oxygen ion. They report that for host cations smaller than Ce^{4+} in fluorite-structure, the asymmetric cation relaxations around an oxygen vacancy can lead to a significant contraction of the lattice [Chatzichristodoulou *et al.* 2015, Marrocchelli *et al.* 2013]. This is observed by the

shift of X-ray reflection peaks towards higher angles. Such an effect has been observed in some other similar chemical systems too [Sayed*, et al.* 2012, Thampi *et al.* 2015]. A close examination of the XRD patterns showed that there is no considerable change in the width of diffraction peaks with respect to both substitutions. Instrumental broadening, crystallite size effect and lattice strain are the key factors that contribute to the line width in diffraction pattern. Since the first two factors were made as equivalent as possible for all the samples through same measurement conditions and similar crystallite sizes, any change in the line width could be loosely attributed to the lattice strain. Absence of such an effect may be indicating that the substitution process does not introduce much strain to the lattice. In this context, it is reasonable to assume that when the cationic size difference is comparatively smaller, the effect of oxygen vacancies becomes dominant as far as substitution by Sc^{3+} and Y^{3+} are compared.

3.3.1.2. FT-Raman analysis

A parallel way to understand the structural influence of the ionic substitution was attempted through FT-Raman analysis. In the cubic fluorite structure, the site symmetry of the 4*a* site cation is O_h and that of the 8*c* anion is T_d [N. Kjerulf-Jensen 1996]. Factor group analysis had shown that an ideal cubic fluorite lattice would possess only one Raman active mode T_{2g} which is generally found at ~470 cm^{-1} [Banerji *et al.* 2009, Li *et al.* 2011, McBride *et al.* 1994]. However in the Raman spectra of the present samples shown in Figure 3-5, more than one peak could be distinguished in the Raman spectra which are generally broad in nature. The broad nature of Raman modes cannot be a result of small crystallite size since the sharp X-ray reflections and the images in the SEM and TEM analyses indicate the contrary. The broadness is a result of inherent deviations from the translational periodicity in the lattice of a disordered fluorite structure [Mandal*, et al.* 2007, Moriga *et al.* 1990, Wan*, et al.* 2011]. Presence of

some additional vibrations below and above the T_{2g} frequency can be justified by acknowledging the deviation of the present system from an ideal fluorite lattice. In such defect fluorite-type crystals some degree of ordering will always be present due to the different cations occupying the same crystallographic site and this is expected to give rise to some additional vibrational modes as visible in Figure 3-5 [Banerji, *et al.* 2009, Li, *et al.* 2011]. As observed in the present system, T_{2g} mode in defect fluorites is reported to be generally very weak and broad in nature [Hess *et al.* 2002, Radhakrishnan, *et al.* 2011].

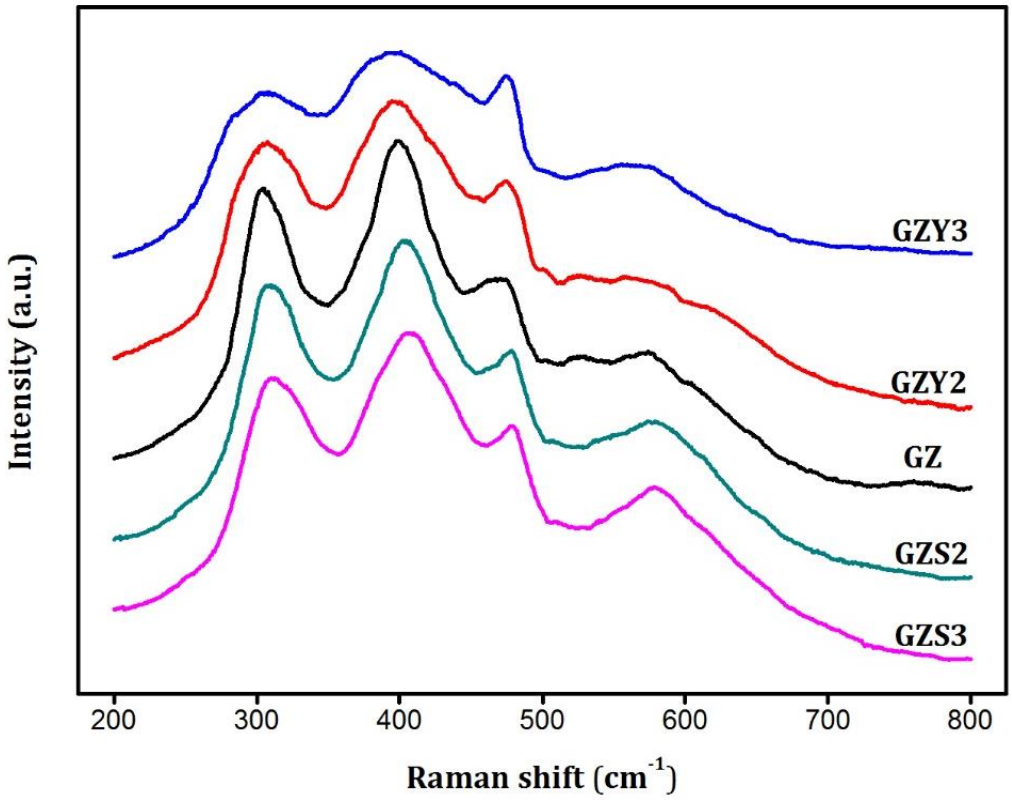

Figure 3-5: FT-Raman spectra showing the effect of cation substitution.

Broadening of vibrational modes is often an indication of increasing disorder in a crystal lattice. The cationic size difference is a crucial factor deciding the extent of order in fluorite-related structures like pyrochlores. In pyrochlore type structures with a general formula $A_2B_2O_7$, the ratio of radii of A and B cations

(r_A/r_B) gives a measure of order. In the discussions regarding the order-disorder transitions in such chemical systems, ordered pyrochlore structure is said to be stable in the r_A/r_B range of 1.76 to 1.46 and a decrease in r_A/r_B is a driving factor of disorder [Chakoumakos 1984, Minervini, *et al.* 2000, Subramanian, *et al.* 1983]. Considering the size of the cations involved in the present system, it can be inferred that substitution by Sc and Y, both being larger than Zr and smaller than Gd, would in effect bring down the cationic size difference in the lattice thereby leading to more disorder. This can be understood from the observation that Y^{3+} substituted system, it being the larger of the two substituent cations, show more broadening than the Sc^{3+} substituted one [Mandal, *et al.* 2007].

A contrast between two substitutions is seen when the peak position is analysed. With Sc-substitution, the T_{2g} mode is found to show a small positive shift in frequency whereas with Y-substitution it is showing a small negative shift. McBride *et al.* had observed and explained a positive frequency shift of Raman modes in fluorite structure due to the formation of oxygen vacancies in the lattice [McBride, *et al.* 1994]. According to their model oxygen vacancies can give rise to another peak at ~570 cm^{-1} which was later reported by Li *et al.* also [Li, *et al.* 2011]. A small hump can be observed in our Sc-substituted system too, at an adjacent frequency, which can be interpret to emphasize the dominance of oxygen vacancies in deciding the structural properties of those chemical compositions. A small negative shift of vibrational modes in Y-substituted compositions can be attributed to the increase in lattice volume caused by the considerably larger substituent cation [McBride, *et al.* 1994].

3.3.2. Thermal expansion

High-temperature X-ray diffraction study was carried out to investigate the response of the crystal lattice to change in temperature. Powder XRD patterns of various samples were recorded at intervals of 200 degrees from 298 K to 1273

K and the evolution of various structural features were observed. These materials retained their crystallinity and crystal structure at all measuring temperatures and did not show any structural transition. Figure 3-6 shows the expanded view of the (111) Miller reflection of one representative sample GZY3 at various measuring temperatures.

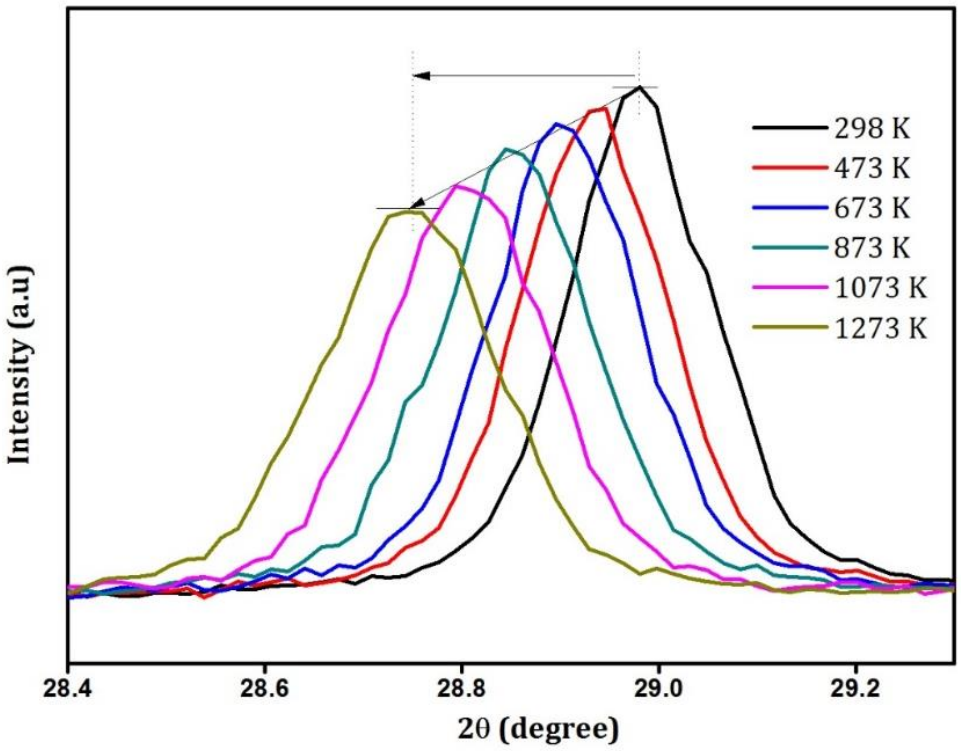

Figure 3-6: Effect of temperature on the (111) peak of GZY3 sample

The effect of increase in temperature is reflected in two aspects of the X-ray diffraction peak; position and intensity. As the temperature increases from 298 K towards 1273 K, the peaks progressively shift towards lower diffraction angles and at the same time their intensity dwindle. The shift of peaks is quite obvious since the phonon frequencies in real crystals depend on the amplitude of lattice vibrations hence making the phonon gas pressure a temperature-dependent parameter. The ultimate reason for this is the anharmonic nature of lattice potential which in a vast majority of real crystals lead to an expansion of

linear dimensions with increase in temperature. Thus the progressive shift of X-ray diffraction peaks towards lower angles is the direct indication of thermal expansion behavior.

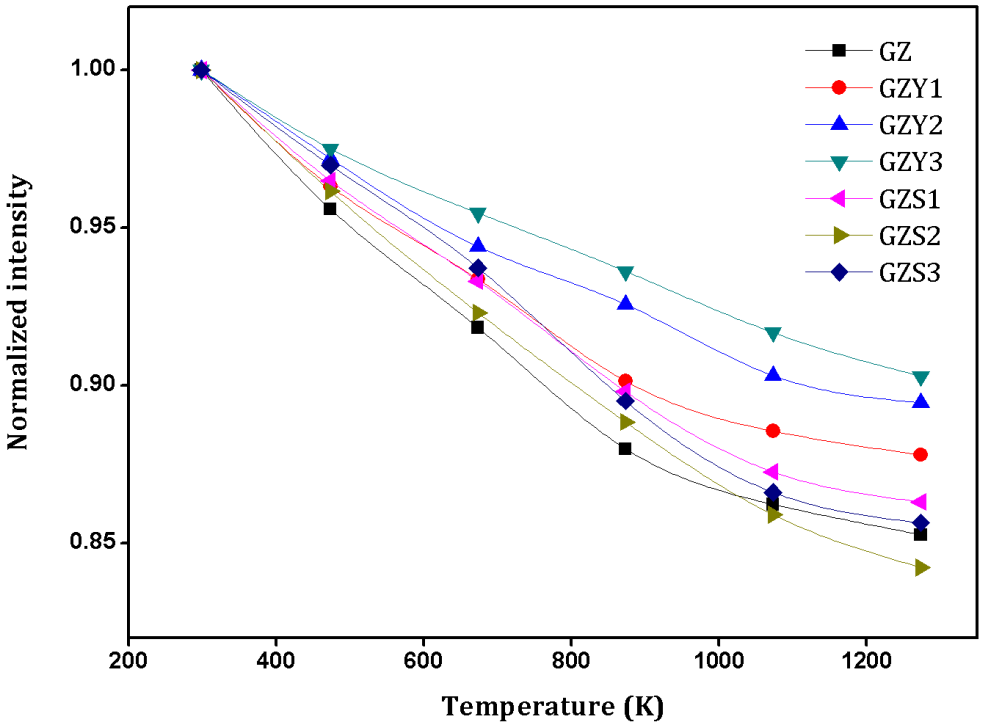

Figure 3-7: Change in intensity of the (111) XRD peak of various samples with temperature

A plot of integrated intensity (normalized by maximum) of the (111) peak against temperature for various samples is shown in Figure 3-7. The decrease in peak intensity can be explained by the effect of lattice vibrations on the coherent scattering of X-rays from the crystal. As the prime role in X-ray scattering from a crystal is played by the electron cloud around various atoms, the vibration of atoms about their equilibrium positions has an effect of smearing the electron cloud into larger volumes in effect bringing about a decrease in electron charge density. Thus, the increase in vibration amplitude with increase in temperature should lead to a decrease in scattering intensity. This effect has been formulated as the Debye-Waller factor (DWF) that appears as an

exponential term in the theoretical expression for Bragg peak intensity [Kim *et al.* 2003]. The concept of DWF is quite involved and its calculation warrants more sophisticated instrumentation [Mohanlal 1979]. Even then, it is reasonable to assume that the rate of decrease of intensity is connected to the rigidity of the lattice, since the amplitude of atomic vibrations are dependent on it. It can be seen that the Sc-substituted samples are more susceptible to loss of scattering intensity with respect to temperature. With increase in Y-substitution the rate of decrease in intensity shows a decrease. This can be an indication of increase in rigidity of the lattice.

The recorded X-ray diffraction patterns of all the samples at all temperatures were analysed by carrying out Le-Bail fitting using X'Pert HighScore plus software which yielded the corresponding lattice parameter values. A plot of lattice parameter against temperature showed a linear relationship between the two and the slope of the respective plots could be used to calculate their thermal expansion coefficient through the equation,

$$\alpha = \frac{1}{a_{298}} \frac{da}{dT} \tag{3.2}$$

where α is the thermal expansion coefficient (TEC), a_{298} is the original lattice parameter measured at room temperature and $\frac{da}{dT}$ is the slope of the lattice parameter variation with respect to temperature. Effect of cationic substitution on the thermal expansion behavior is reflected in the plot of TEC against the substituent mole fraction (x), as shown in Figure 3-8. It can be seen that the TEC decreases with increase in substitution for both Sc and Y. Although both cations introduce the same effect, the mechanisms through which these effects are brought about seem to be different.

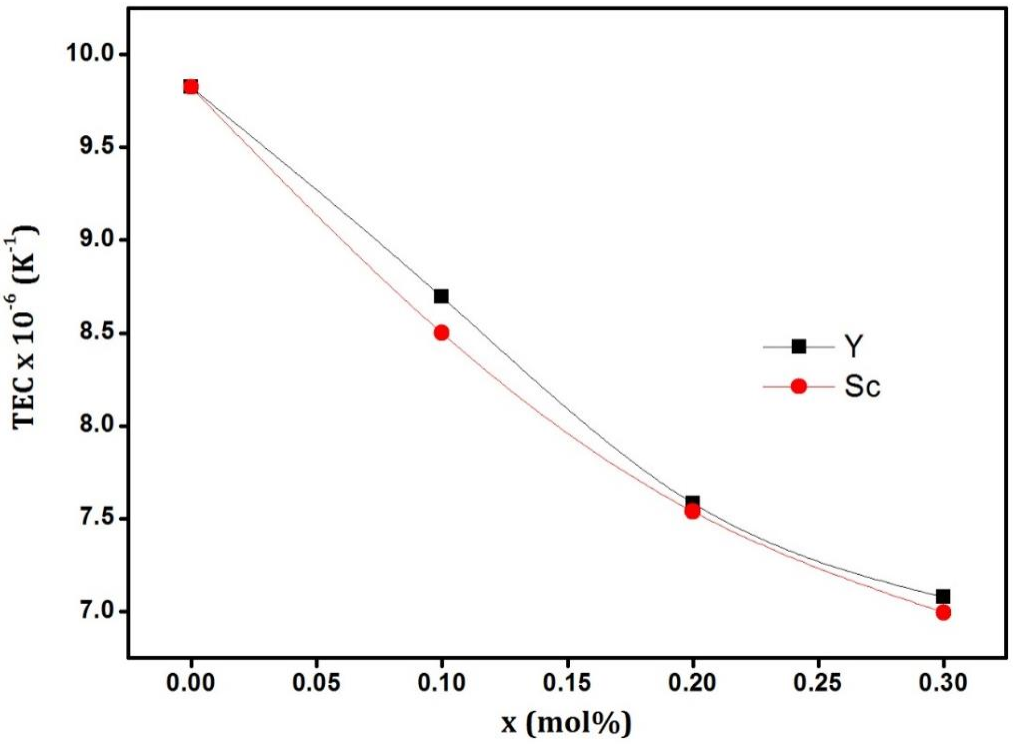

Figure 3-8: Variation of thermal expansion coefficient (TEC) with substitution

The decrease in TEC with Y-substitution can be explained by the change in ionic nature of the average diatomic bonds in the crystal. The electronegativity of Zr, Sc, Y and O in Pauling scale are 1.33, 1.36, 1.22 and 3.44 respectively [Lide 2005]. Since the ionic nature, and hence the strength of bonding, is proportional to the difference in electronegativities of the participant atoms, substitution of Zr atoms by less electronegative Y atoms is going to increase the ionic nature of the average diatomic bond in the crystal. This will increase the ionization energy of the electrons involved in the bonding process which is connected to the phonon frequency. There exists a theoretical proof that the square of the phonon frequency is directly proportional to the exponential of the ionization energy of the bond-forming electrons [Arulsamy 2011]. Hence in the Y-substitution scenario of the present system, the phonon frequency is expected to increase thereby making the lattice more rigid. This can explain the decrease in thermal

expansion coefficient. But in the case of Sc-substitution, direct influence of ionic nature is not seen since, Sc being more electronegative than Zr should in that case increase the TEC. The reverse trend observed here may be attributed to the oxygen vacancies. As we have observed the dominance of oxygen vacancies in Sc-substituted system, this decrease in TEC may be due to the clustering of oxygen vacancies as was earlier reported by Liu *et al.* [Liu, *et al.* 2009]. The lattice contraction caused by these vacancies may also contribute to this phenomenon.

3.3.3. Morphology

The surface morphology of sintered pellets were examined using scanning electron microcopy. All the pellets had a sintering density of around 80% of the theoretical density. The SEM images of polished surfaces of three representative samples are shown in Figure 3-9. The typical polycrystalline morphology consisted of grains varying in size, generally in 2 μm to 6 μm range. Distinct grain boundaries could be seen along with some amount of porosity.

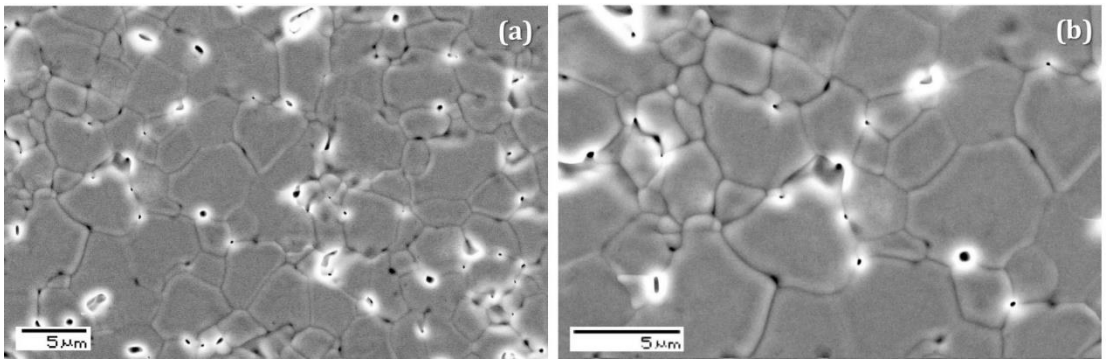

Figure 3-9: SEM images of the polished surfaces of two representative samples (a) GZY3 (b) GZS3

The powder X-ray diffraction pattern serves to indicate only the average crystalline nature of a bulk sample and hence transmission electron microscopy (TEM) was used to confirm the crystallinity of the chemical systems in small domains. Figure 3-10 shows the HR-TEM images of some representative samples.

(a), (b) and (c) are high-resolution images of GZ, GZY3 and GZS3, where lattice planes could be identified and indexed by a comparison of their spacing with the X-ray diffraction data. The selected area diffraction pattern showed concentric rings typical of polycrystalline samples. But, since the powder samples consisted of fairly big particles, typically in micrometer range, the rings did not seem continuous but consisted of intermittent spots. The indexed rings are marked in Figure 3-10(d) which were identified by their radii compared with typical interplanar spacings in fluorite lattice.

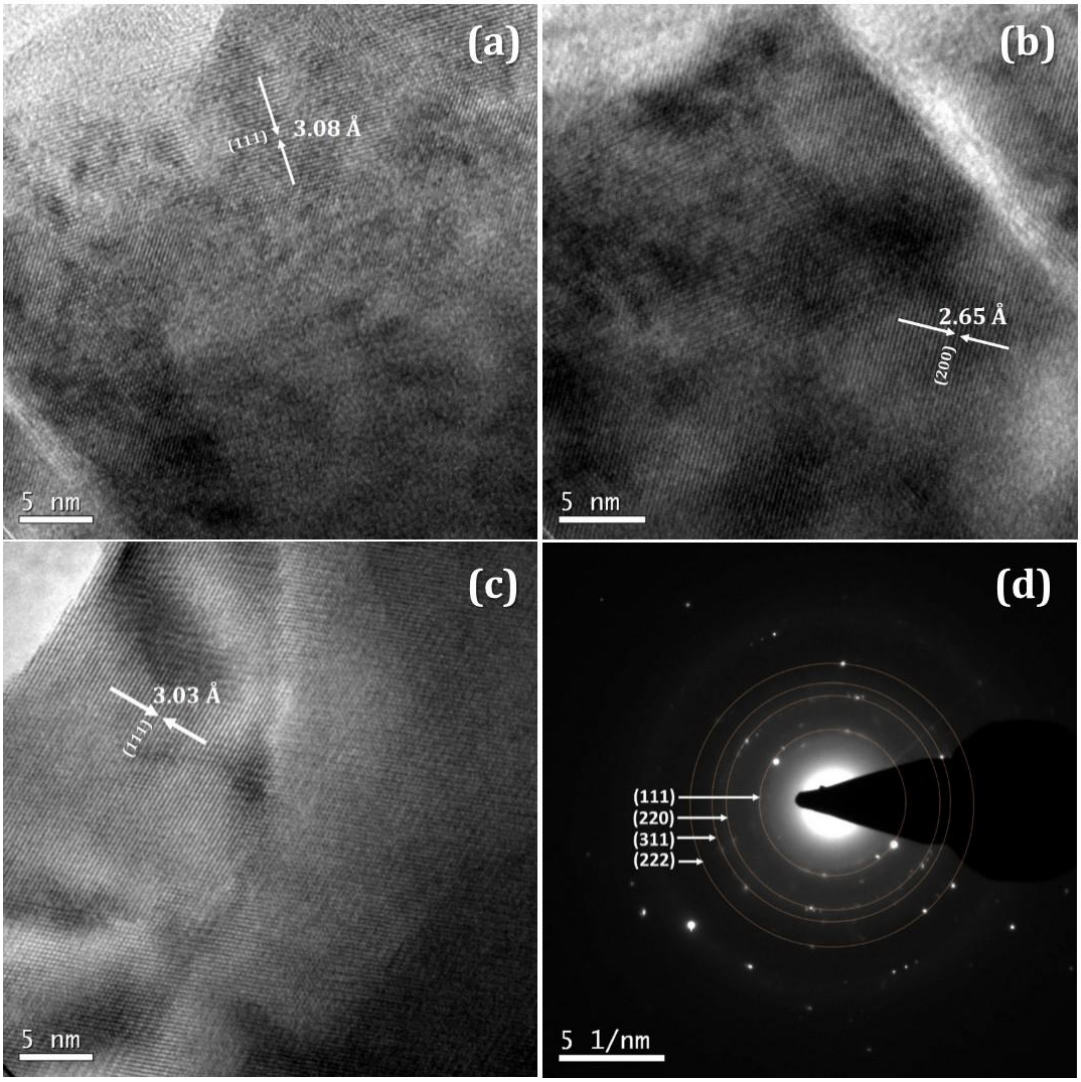

Figure 3-10: TEM images of various samples. (a), (b) and (c) show the HR-TEM images of GZ, GZY3 and GZS3 respectively, (d) shows the SAED pattern of GZY3

3.3.4. Electrical properties

The sintered pellets of the prepared samples were given a small ac signal (100 mV) of varying frequency (1 Hz – 1 MHz) and their response was analysed using impedance spectroscopic technique. A polycrystalline material in such a scenario is often considered a series of parallel RC-circuits, with the resistance (R) corresponding to conduction and the capacitor (C) corresponding to the charge accumulation effects. A Nyquist plot of imaginary part of impedance against the real part of an RC parallel circuit is a semicircle with diameter R. Since the capacitance values associated with charge accumulation depends on where it happens, whether it is within the bulk of grains, in the grain boundaries or in the sample-electrode interface, the Nyquist plot for a polycrystalline material will ideally consist of three semicircular arcs.

Figure 3-11 shows this complex plane representation of ac impedance of a representative sample, GZY3, at two different temperatures. Two semicircles could be distinguished, the mechanisms responsible for which can be identified from the capacitance values associated with them. Grain boundaries offer higher capacitance due to bigger chances of charge polarization and therefore the relaxation associated with the grain boundary phenomena falls in lower frequency region, whereas the grain relaxation happens in higher frequencies [Liu*, et al.* 2010]. Depending on the range of measurement frequency and the difference in relaxation frequencies between grain and grain boundary phenomena, the semicircles may appear incomplete or merged as observed in Figure 3-11. It could be seen that, as temperature increases the semicircles became smaller in diameter.

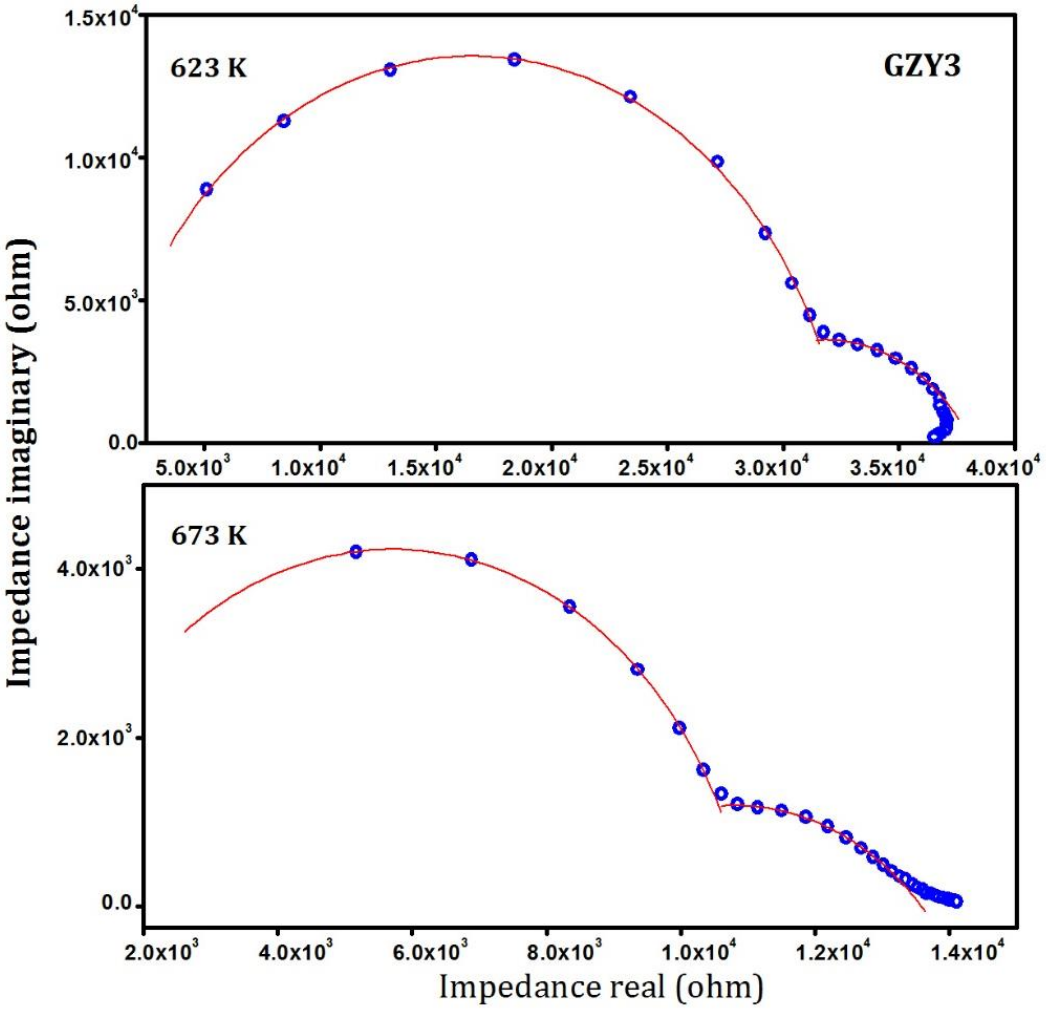

Figure 3-11: Complex plane representation of ac impedance of representative sample, GZY3, at two temperatures

The intercept of an impedance semicircle with the real axis gives the ohmic resistance, *R*, offered against the conduction process associated with it. With increase in temperature, the semicircles diminish in radius indicating a decrease in resistance. Considering the sample thickness (*l*) and the electroding area (*A*), the conductivity σ can be calculated as,

$$\sigma = \frac{l}{RA} \tag{3.3}$$

Since the grain and grain boundary semicircles were not always well-resolved, only their total resistance was considered to calculate the conductivity

at various temperatures. The conductivity value increases with increase in temperature.

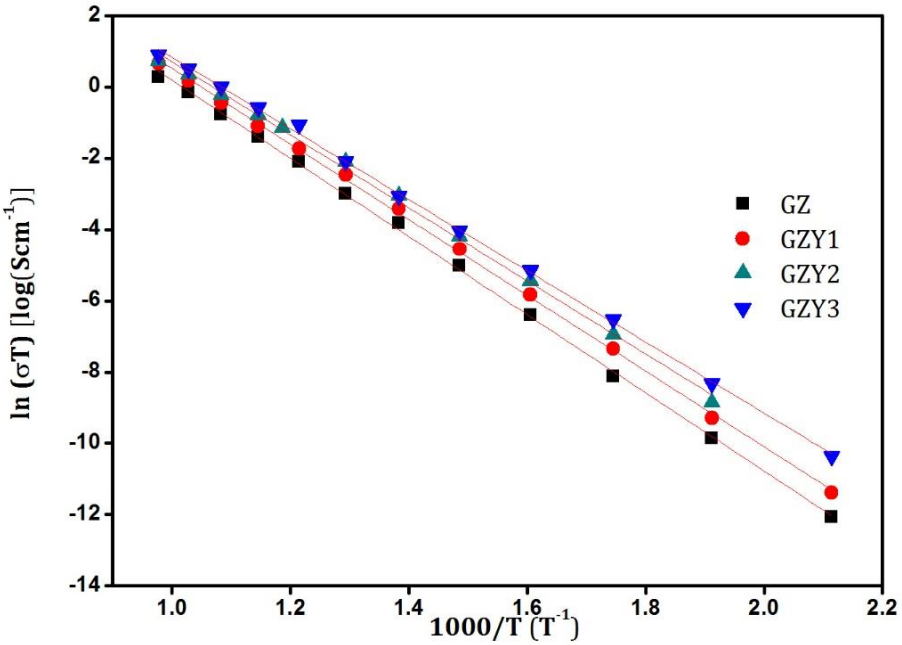

Figure 3-12: Arrhenius plots of various samples in GZY series

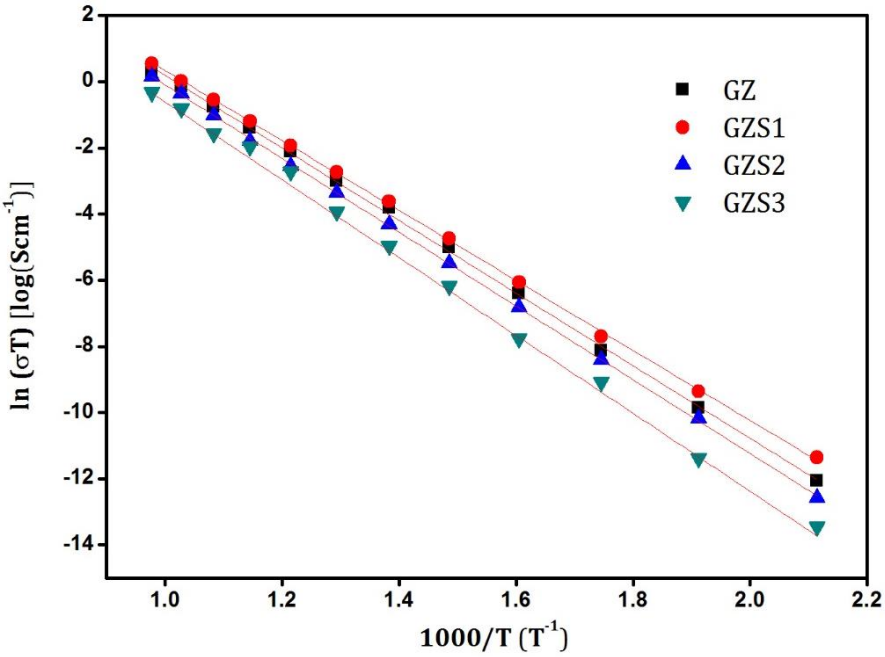

Figure 3-13: Arrhenius plots of various samples in GZS series.

Figure 3-12 and Figure 3-13 show the Arrhenius plots of various samples, where the straight lines are the least squares fit of the conductivity data with the linearized form of Arrhenius equation (Eq. 1.12). The slopes of the straight line fits would yield the values of activation energy. The values of conductivity at maximum measuring temperature (1023 K) against substitution is plotted in Figure 3-14 and the corresponding trend of activation energy is shown in Figure 3-15.

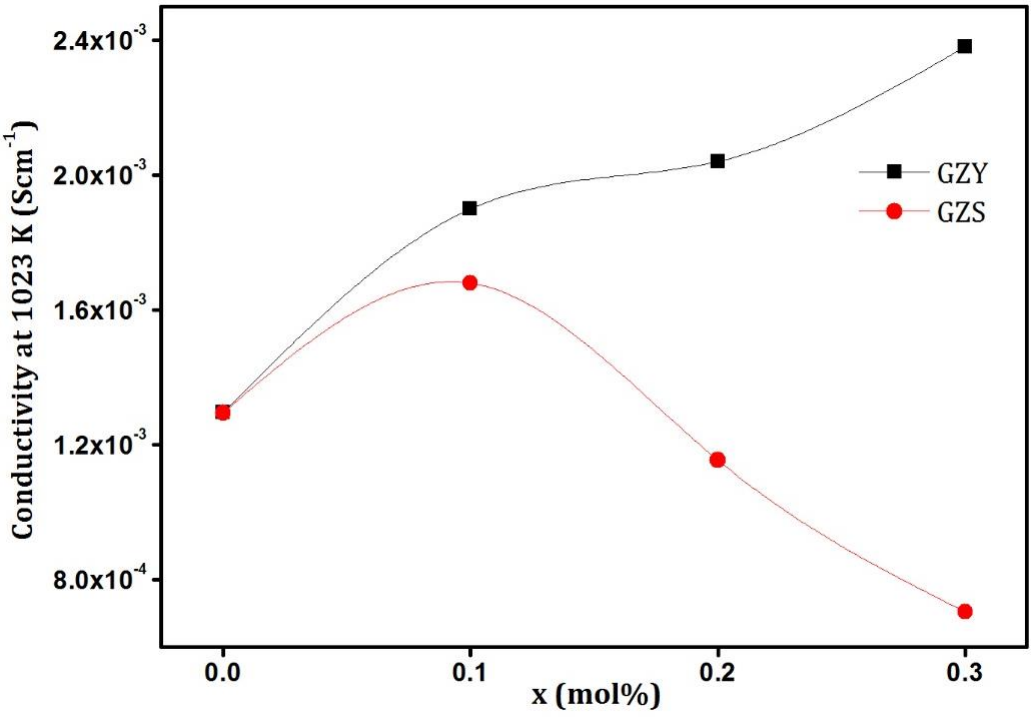

Figure 3-14: Effect of substitution on the conductivity of various samples

It can be seen that, for GZY series, the conductivity increases with increase in substitution along with a corresponding decrease in activation energy. But in the case of GZS series, the trend is different. With substitution of Sc^{3+}, the activation energy decreases at first and then it starts to increase which reflects directly in the trend of conductivity variation also.

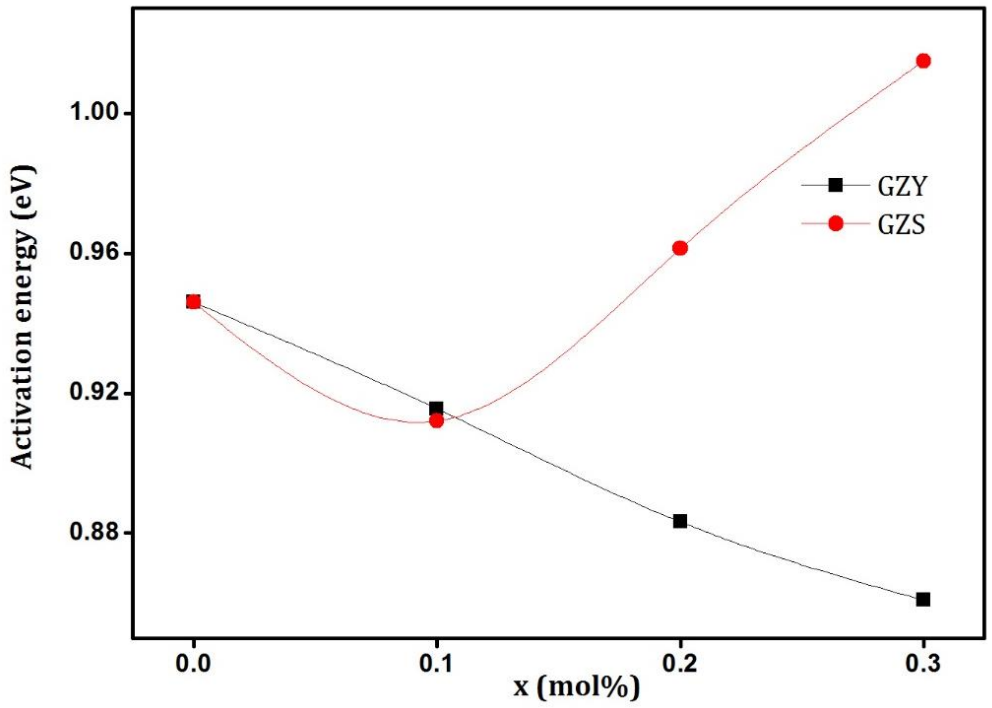

Figure 3-15: Effect of substitution on activation energy of various samples

For a better understanding of the processes involved, analysis was extended to electric modulus function, M^*, which is essentially the reciprocal of dielectric permittivity and is connected to complex impedance (Z^*) as [Hodge *et al.* 1976],

$$M^* = j\omega C_0 Z^* \tag{3.4}$$

where C_0 is the vacuum cell capacitance and ω is the frequency. The advantage of modulus formalism is that it highlights the bulk processes and does not receive much contribution from electrode polarization effects. Figure 3-16 shows a frequency plot of the imaginary part (M'') of the electric modulus at various temperatures measured on the representative sample GZY3. Its value is nearly zero in the low frequency region for all temperatures, but shows a peak at a particular frequency which shifts towards higher values with increase in temperature.

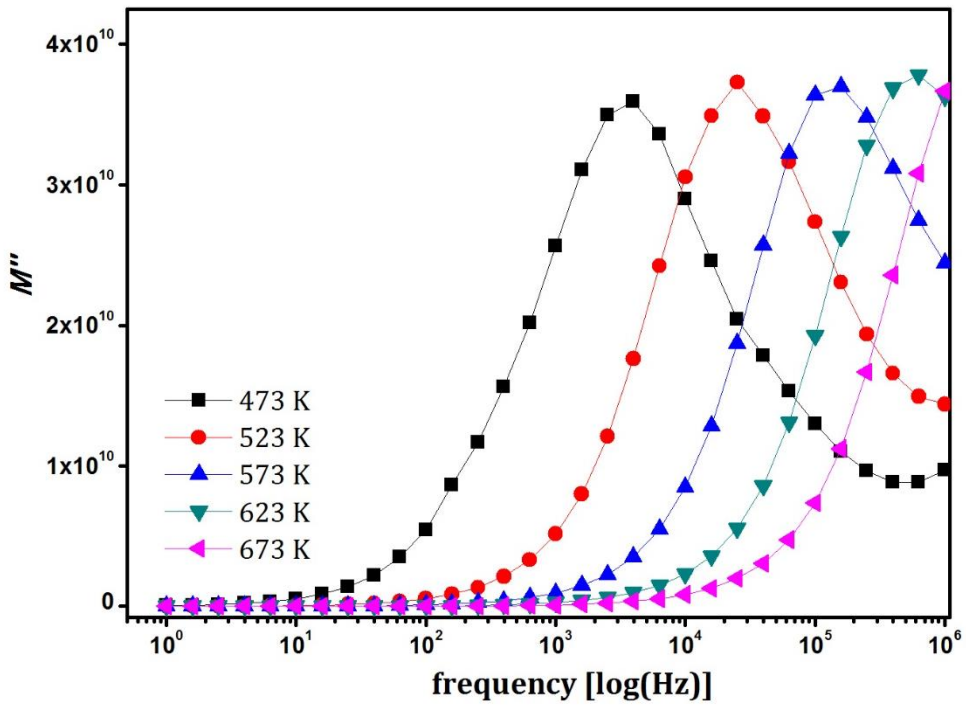

Figure 3-16: Frequency plot of imaginary part of electric modulus of representative sample GZY3.

The peak is obviously an indication of the dielectric relaxation behavior which in oxide ionic conductors is often attributed to the charge re-orientation of ions involving the vacancies [Baral and Sankaranarayanan 2009, Sarkar and Nicholson 1989]. The low frequency side of the relaxation peak corresponds to long-range conduction of ions whereas the higher frequency side to spatially confined ions [Réau *et al.* 1994]. The blue-shift of peak frequency implies a thermally activated ionic transport to which Arrhenius fitting is possible and activation energy could be calculated therefrom. The activation energies calculated from modulus and conductivity considerations were similar in values which indicated that the conduction mechanism in these materials is primarily through ion hopping [Padmasree *et al.* 2006, Réau, *et al.* 1994]. The trend in conductivity as observed in Figure 3-14 can now be explained in terms of the oxygen vacancies and the lattice volume. The reason for enhanced conductivity

in GZY series with substitution of Y^{3+} is apparently obvious. It can be a result of increase in oxygen vacancies which would in effect bring about a low energy pathway for ionic transport within the crystal. The increase in lattice volume brought about by the substitution can also make positive contribution to the ease of ionic diffusion process.

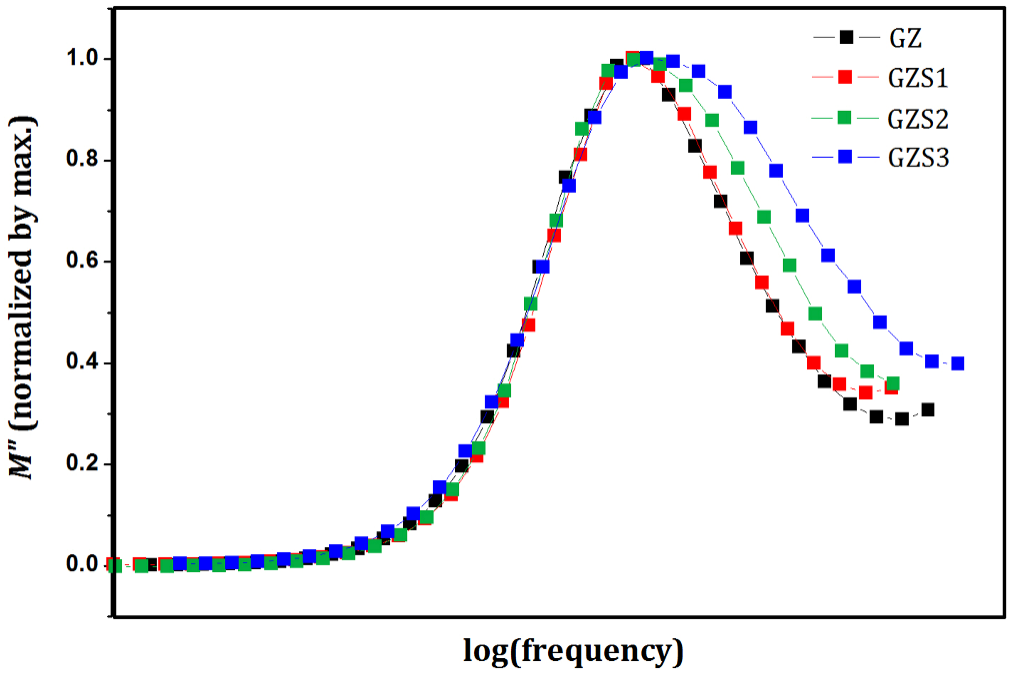

Figure 3-17: Broadening of modulus relaxation peak of GZS samples at 523 K. (plots were shifted along the abscissa for clarity)

However, the effect of Sc^{3+} substitution in GZS series is different. Although the activation energy decreases at first due to increase in available oxygen vacancies, the system fails to keep that up for higher substituent concentration. It may be due to the cooperative behavior of ions in the lattice as conceived by Jonscher [Jonscher 1977] where hopping of one ion can cause a time-dependent movement of other charge carriers in the neighborhood leading to additional relaxations. This would lead to a broadening of relaxation peaks in the modulus spectra [García-Barriocanal *et al.* 2005, Moreno; *et al.* 2005] as can

be seen in Figure 3-17, which shows a plot of imaginary part of electric modulus (normalized by maximum, M''/M''_{max}) of various GZS samples at 523 K. Various plots were shifted along the abscissa for clarity and beyond $x = 0.1$, a broadening of peak can be observed indicating a correlated ionic motion. This ion-ion interaction is generally reported to be detrimental to the overall electrical conductivity by posing a higher activation energy for long range ionic transport [Garcia-Barriocanal*, et al.* 2009]. This increased cooperative behavior of oxygen vacancies in Sc-substituted compositions when compared with the Y-substituted ones may be a result of decrease in lattice volume. Thus it comes out that, although Sc and Y belong to the same group, their influences on the overall behavior of the parent lattice are different from one another making it difficult to formulate a general rule that can guide an enhancement in desirable properties. The results also point out that the lattice volume is also an important variable to be considered along with generation of oxygen vacancies.

3.4. Conclusion

$Gd_2(Zr_{1-x}M_x)_2O_{7-\delta}$ solid solutions were prepared to investigate the effect of substitution by M cation (M = Sc^{3+}, Y^{3+}) on structure and electrical properties. Both systems crystallized in fluorite-type lattice, showing similar extent of solid solution formation. Sc^{3+} lead to a contraction of the lattice *via* lattice defects, while Y^{3+} forced the lattice to expand due to its larger ionic radius. Both systems had oxygen vacancies due to aliovalent substitution, but their effect was more pronounced in the Sc-substituted compositions, as was evident in X-ray diffraction and Raman analysis. Oxygen vacancies in the expanded lattice aided in enhanced electrical properties in Y-substituted system by reducing the energy barrier for thermally activated conduction. Whereas for Sc-substituted system, cooperative behavior of ions in the contracted lattice acted in the reverse direction. Thus it could be concluded that, despite them being in the same group

of *d*-block elements, the ultimate influence in physical aspects depended on the identity of the substituent ions.

CHAPTER 4

****

Influence of Ce Substitution on the Order-to-Disorder Structural transition, Thermal expansion and Electrical properties in $Sm_2Zr_{2-x}Ce_xO_7$ system

****

Substitution in the B-site through a composition, $Sm_2Zr_{2-x}Ce_xO_7$(x= 0, 0.1, 0.2, 0.3, 0.4, 0.5) was studied. Ce ions induced structural disorder to both cationic and anionic sublattices, gradually transforming the unit cell from an ordered pyrochlore to a defect fluorite structure with lattice expansion. The ionic disorder led to decreased energy barrier for the thermally activated conduction process thereby increasing the overall conductivity of the materials. Beyond x = 0.4, the ion-ion interaction in the disordered lattice began to dominate, leading to increased activation energy and decreased total conductivity. It was also found that the thermal expansion of these oxides is predominantly influenced by the B—O bond energy than the Madelung binding energy.

D. S. Vaisakhan Thampi, P. Prabhakar Rao and A. N. Radhakrishnan, "Influence of Ce substitution on the Order-to-Disorder Structural Transition, Thermal expansion and Electrical properties in $Sm_2Zr_{2-x}Ce_xO_7$ system", ***RSC Advances***, 4, 12321–12329 (2014)

4.1. Introduction

Pyrochlore structured compounds have been so important in various facets of materials science due to their interesting physical and chemical properties. Many pyrochlore oxides are reported to have very good oxide ionic conductivity and are promising candidates to be used as Solid Oxide Fuel Cell electrolytes [van Dijk *et al.* 1983]. There are two different cationic sites in a pyrochlore structure. With the six-coordinated B cation site as origin (denoted by Wyckoff symbol 16*c*), the A cations occupy an eight coordinated 16*d* site (0.5, 0.5, 0.5). There are three different anion sites; the 48*f* (*x*, 0.125, 0.125), which has two A- and two B- nearest neighbours, the 8*a* (0.125, 0.125, 0.125) which has four B nearest neighbours and the 8*b* (0.375, 0.375. 0.375), which has four A nearest neighbours. The 8*a* site is normally vacant in an ideal ordered pyrochlore. With this diversity in crystallographic sites, pyrochlore is considered to be an ordered structure. Whereas, the associated crystal structure fluorite is called a disordered structure, since there are only two different lattice sites; 4*a* (0, 0, 0) occupied by cations and 8*c* (0.25, 0.25, 025) occupied by anions. Many reports suggest that a transition from ordered pyrochlore to disordered defect fluorite, or *vice versa*, has significant influence on various physical properties of materials, including the conductivity.

Structural transition from pyrochlore to a defective fluorite structure can be driven by variation in chemical composition [M. A. Subramanian 1983], temperature [Wang *et al.* 2003], pressure *etc*. Moreover, this disordering occurs simultaneously and independently for cations and anions [Ewing, *et al.* 2004, Lian *et al.* 2003]. The ratio of the ionic radii of the cations involved, $(\frac{r_A}{r_B})$, plays a crucial role in the stability of the pyrochlore structure [Zhang *et al.* 2006]. Pyrochlores are reported to be stable in the $(\frac{r_A}{r_B})$ ratio range of 1.46 to 1.78 [Chakoumakos

1984, M. A. Subramanian 1983, Minervini, *et al.* 2000]. Controlling this ratio and thereby inducing order-disorder transition to get improved ionic conduction in pyrochlore oxides has been attempted widely [Garcia-Barriocanal, *et al.* 2009].

Pyrochlore structured $Sm_2Zr_2O_7$ is reported to possess good conducting properties comparable to other low-temperature ionic conductors [Shinozaki *et al.* 1979]. Attempts to enhance its electrical properties by homovalent and aliovalent substitution of cations are widely attempted [Liu *et al.* 2010, Xia *et al.* 2009]. In $Sm_{2-x}La_xZr_2O_7(0\leq x \leq 1.0)$ system, La did not alter the crystal structure of the parent lattice and its overall influence on the electrical conductivity was to decrease it [Liu, *et al.* 2011]. In independent works, Xia *et al.* reported that degree of structural disorder in $(Sm_{1-x}Y_x)_2Zr_2O_7$, $(Sm_{1-x}Eu_x)_2Zr_2O_7$ and $(Sm_{1-x}Mg_x)_2Zr_2O_{7-x}$ systems gradually increases with increase in the substitution of ions and it also influenced the total ionic conductivity [Lang *et al.* 2010, Xia *et al.* 2012, Xiao-Liang Xia 2010]. The transformation from ordered pyrochlore to a disordered defect fluorite structure has been found to be influential in the ionic conductivities of many other chemical systems like $Y_2Sn_{2-x}Zr_xO_7$ and $Nd_{2-y}Ho_yZr_2O_7$ also [de los Reyes *et al.* 2013, Sayed, *et al.* 2012]. As far as the conducting properties of pyrochlore type crystals are concerned, the 48*f* oxygen site is reported to play a crucial role in the ion diffusion mechanism in the lattice [Burggraaf, *et al.* 1981, Wilde and Catlow 1998]. This 48*f* oxygen is also related to the thermal expansion properties of the crystal *via* the Madelung energy in zirconate pyrochlores [Kutty *et al.* 1994, Shimamura, *et al.* 2007]. In industrial applications like fuel cells, both conducting properties and the thermal expansion properties of the materials are important factors to be considered. Here in this work an attempt has been made to tailor disordering in the pyrochlore type $Sm_2Zr_2O_7$ via B-site substitution by Ce^{4+} and to study its influence on the total ionic conductivity of the system, while keeping track of the change in unit cell and thermal expansion properties.

4.2. Experimental

The $Sm_2Zr_{2-x}Ce_xO_7$ compositions were prepared via conventional solid-state reaction route.[Radhakrishnan *et al.* 2011] Commercially available Sm_2O_3 (Alfa Aesar, 99.99%), ZrO_2 (Aldrich, 99%) and CeO_2(Aldrich, 99.9%) were chosen as the starting materials. Thoroughly mixed reactants were calcined at 1573 K for 6 hours. Calcined pellets were grinded and recalcined at 1873 K for 6 hours. Green cylindrical pellets prepared by uniaxial compaction at 25 MPa were sintered at 1923 K for 24 hours. The phase analysis was done using an X-ray powder diffractometer (X'pert Pro, PANalytical). Detailed analysis of XRD data was carried out by Rietveld refinement using commercial X'Pert Highscore Plus software. The surface morphology of the surfaces of the sintered pellets was analysed via electron microscopic imaging using a scanning electron microscope (JEOL JSM-5600LV). FT Raman spectra of the powdered samples were recorded using a Bruker RFS100/S spectrometer employing a standard InGaAs detector. The lattice thermal expansion properties were analysed by high temperature XRD technique in a range of 298 K to 1273 K using an Anton Paar HTK attachment to the X'pert Pro diffractometer. Thermal expansion of bulk samples were studied using a thermo mechanical analyser (SII, TMA/SS7300) in the range of 323 K to 773 K. Electrical characterization of the sintered pellets was carried out using an Impedance analyser (Solartron SI 1260) with a dielectric interface (Solartron 1296) in the temperature range 473 K to 1023 K.

4.3. Results and Discussion

The $Sm_2Zr_{2-x}Ce_xO_7$ compositions with x = 0, 0.1, 0.2, 0.3, 0.4 and 0.5 are labelled as SZC 0, SZC 1, SZC 2, SZC 3, SZC 4 and SZC 5 respectively in the coming sections.

4.3.1. Crystal structure

4.3.1.1. X-ray diffraction

The XRD patterns of $Sm_2Zr_{2-x}Ce_xO_7$ are shown in Figure 4-1. It can be seen that the structure of the crystal lattice is dependent on the fraction of Ce^{4+} present. A gradual structure change happens as we go from x = 0 to x =0.5. The diffraction pattern of pyrochlore is basically that of fluorite structure plus a set of low intensity diffraction peaks at around the 2θ values of 14° (111), 28° (311), 37° (331), 45° (511) and 51° (531) which correspond to the ordering in the lattice. The sample x = 0 is crystallized in pyrochlore structure as can be seen in Figure 4-1.

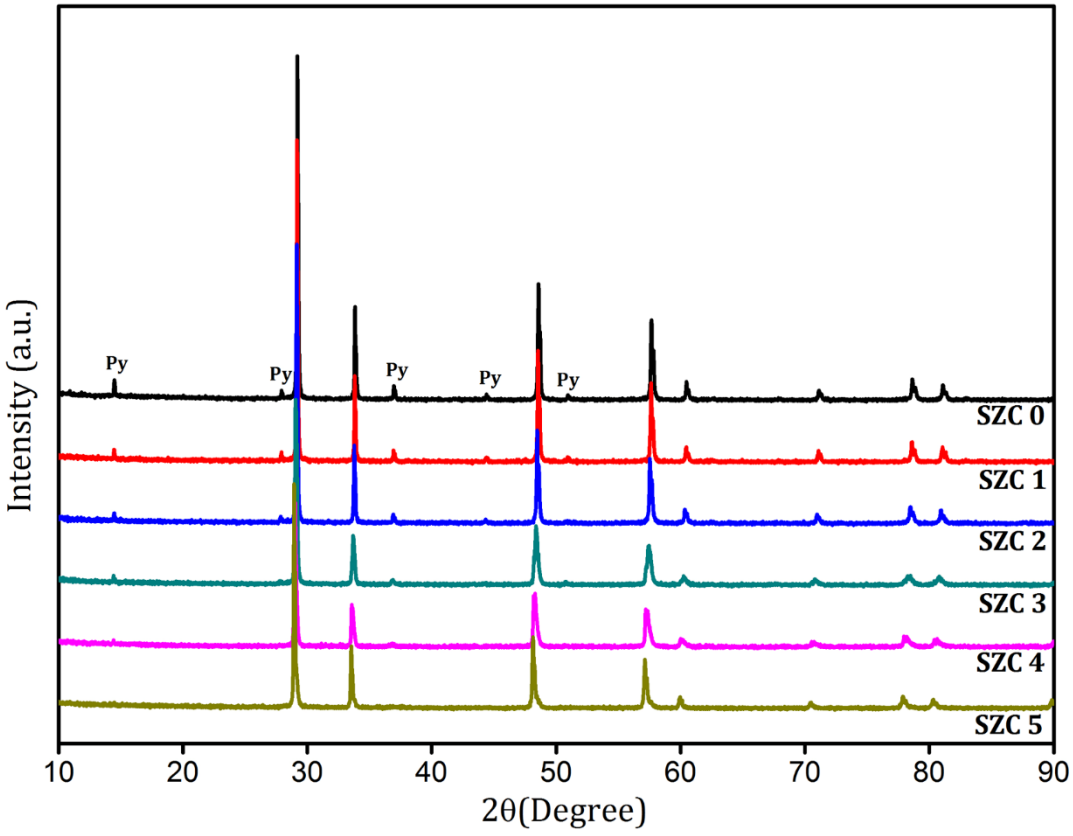

Figure 4-1: Powder XRD patterns of $Sm_2Zr_{2-x}Ce_xO_7$ compositions

The superstructure peaks of the ordered lattice are marked by '**Py**' symbol in the Figure 4-1. The ionic radii of Sm^{3+}, Zr^{4+} and Ce^{4+} are 1.079 Å (VIII),

0.72 Å (VI) and 0.87 Å (VI) respectively [Shannon 1976] where the roman numerals within the parentheses indicate the coordination number. Since Ce^{4+} has a larger ionic radius than Zr^{4+}, its addition to the lattice will decrease the cationic size difference ($\frac{r_A}{r_B}$) thus disrupting the lattice order. This disordering of lattice is manifested as the disappearance of the superstructure peaks in the XRD pattern.

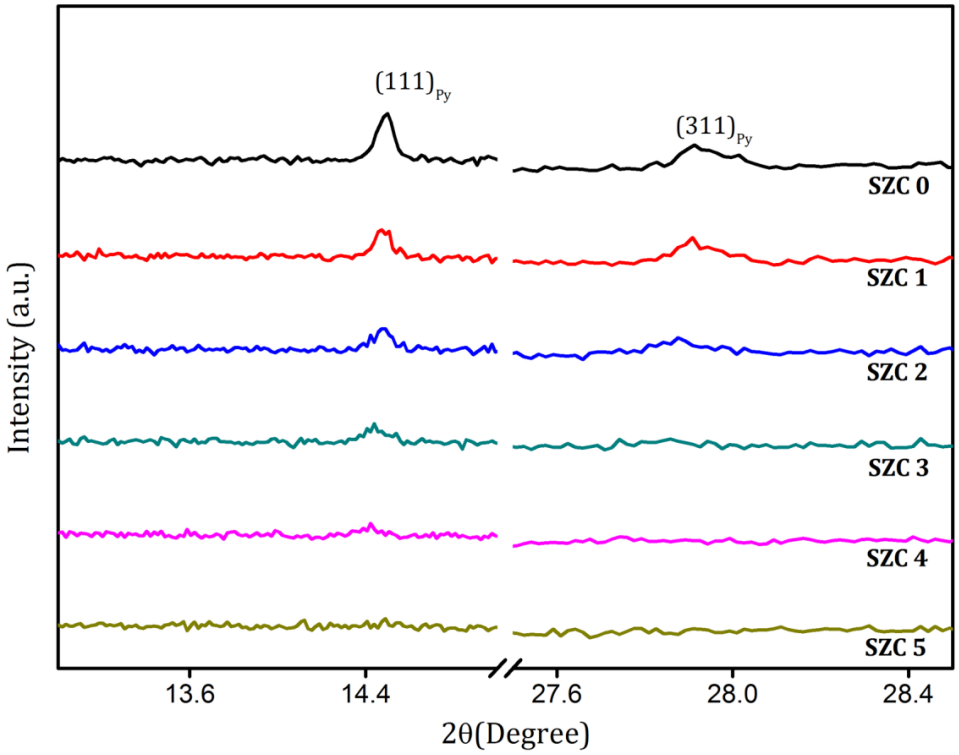

Figure 4-2: Variation of (111) and (311) superstructure peaks with Ce^{4+} substitution

Figure 4-2 shows the (111) and (311) superstructure peaks at various concentrations of Ce^{4+}, from x = 0 to x = 0.5. It clearly indicates that addition of Ce^{4+} to the lattice disrupts the ionic order which results in the disappearance of superlattice peaks at x = 0.5. The sample x = 0.5 is crystallized in a disordered fluorite structure with $Fm\bar{3}m$ space group. Figure 4-3 shows a close examination of the $(622)_{Py}/(311)_{F}$ diffraction peak. It can be seen that with the addition of

Ce^{4+}, the peak shows a shift towards lower angles of diffraction indicating an increase in the lattice spacing resulting from the incorporation of comparatively larger Ce^{4+} ions in place of the Zr^{4+} ions.

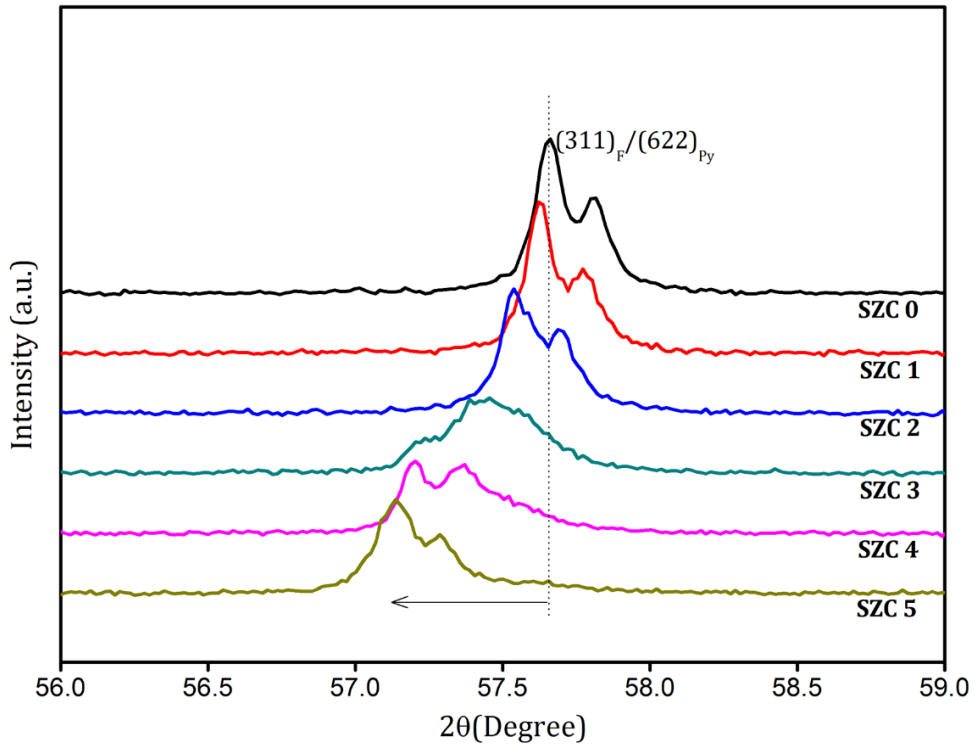

Figure 4-3: Shift in $(311)_F/(622)_{Py}$ peak with Ce^{4+} doping (The smaller peak represents the corresponding Kα2 reflection)

A detailed structural analysis on XRD data was carried out by Rietveld refinement method using X'Pert HighScore Plus software. The stoichiometry used and the XRD patterns observed were used to construct initial structural models of various samples. A pseudo-Voigt profile function was used to fit the diffraction pattern. Background polynomial was refined with respect to flat background and two other coefficients. Other profile functions including Caglioti parameters and asymmetry parameter along with structural parameters like lattice constant and oxygen *x*-parameter were refined. The refined parameters and their values corresponding to the best fit are listed in Table 4-1.

Table 4-1: Refined parameters from Rietveld analysis of $Sm_2Zr_{2-x}Ce_xO_7$ system

Sample	SZC 0	SZC 1	SZC 2	SZC 3	SZC 4	SZC 5
Phase	Pyrochlore	Pyrochlore	Pyrochlore	Pyrochlore	Pyrochlore	Fluorite
Unit cell	Cubic	Cubic	Cubic	Cubic	Cubic	Cubic
Space group	$Fd\bar{3}m$	$Fd\bar{3}m$	$Fd\bar{3}m$	$Fd\bar{3}m$	$Fd\bar{3}m$	$Fd\bar{3}m$
Lattice constant(Å)	10.5962(1)	10.6041(1)	10.6187(2)	10.6387(4)	10.6562(6)	5.3441(1)
Specimen Displacement	-0.046091	-0.031777	-0.053971	-0.020307	0.01278	-0.037034
Flat Background	94.27321	88.72801	86.85529	81.68981	73.78641	77.2878
Coefficient 1	-29.82546	-22.04726	-21.53201	-22.47241	-17.51294	-25.57006
Coefficient 2	33.30337	22.97596	21.18307	24.12136	23.62647	25.88489
Scale factor	0.000003	0.000003	0.000003	0.000002	0.000002	0.000127
Oxygen *x*-parameter	0.3393(9)	0.342(1)	0.3448(9)	0.347(1)	0.351(1)	-
U	0.053718	0.063701	0.111902	0.745046	0.829743	0.087138
V	-0.020268	-0.027337	-0.052835	-0.266091	-0.331451	-0.0127
W	0.00713	0.008477	0.013785	0.051403	0.058735	0.005131
R_{exp}	8.65	9.05	9.15	9.33	9.85	9.66
R_p	7.58	7.66	7.24	7.85	11.08	10.21
R_{wp}	9.86	10.01	9.5	10.15	14.18	13.56
GOF	1.3	1.22	1.07	1.18	2.07	1.96

Samples from x = 0 to 0.4 were best fit using $Fd\bar{3}m$ space group and x = 0.5 was best fit using $Fm\bar{3}m$ space group. The $(\frac{r_A}{r_B})$ ratio for x = 0, 0.1, 0.2, 0.3, 0.4 and 0.5 samples are 1.5, 1.48, 1.47, 1.45, 1.44 and 1.42 respectively. Although the commonly observed lower limit of pyrochlore radius ratio is 1.46 [M. A. Subramanian 1983], $Sm_2Zr_{2-x}Ce_xO_7$ sustains pyrochlore structure to an $\frac{r_A}{r_B}$ value of 1.44. The result of Rietveld refinement for a representative sample is shown in Figure 4-4. The observed and calculated patterns along with the difference patterns are displayed there. The plots show good agreement between observed and calculated diffraction profiles.

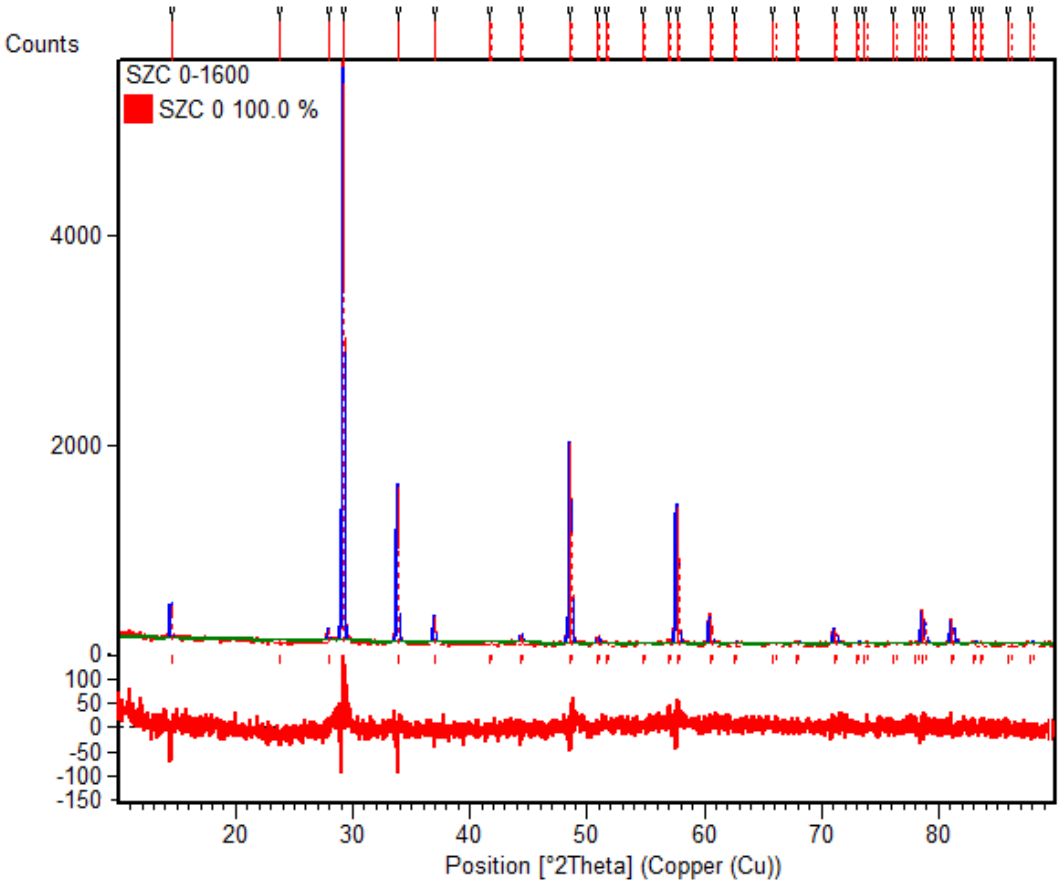

Figure 4-4: Rietveld simulation and refinement of representative samples SZC 0

Rietveld analysis yielded accurate values for the lattice parameter which confirmed the observation in Figure 4-3. In Table 4-1 we can see that the addition of Ce ions leads to an increase in lattice parameter. The calculated lattice parameters from Table 4-1 as a function of Ce^{4+} content are shown in Figure 4-5, wherein the lattice parameter of fluorite type $x = 0.5$ sample has been doubled to fit in graph. It can be seen that the lattice parameter increases almost linearly with increase in Ce content. This is in agreement with Vegard's law [Vegard 1921] according to which the lattice parameter of a mixture will have a linear relation with those of the components *via* the composition. This is applicable to the substitution of larger Ce^{4+} in place of smaller Zr^{4+} ions.

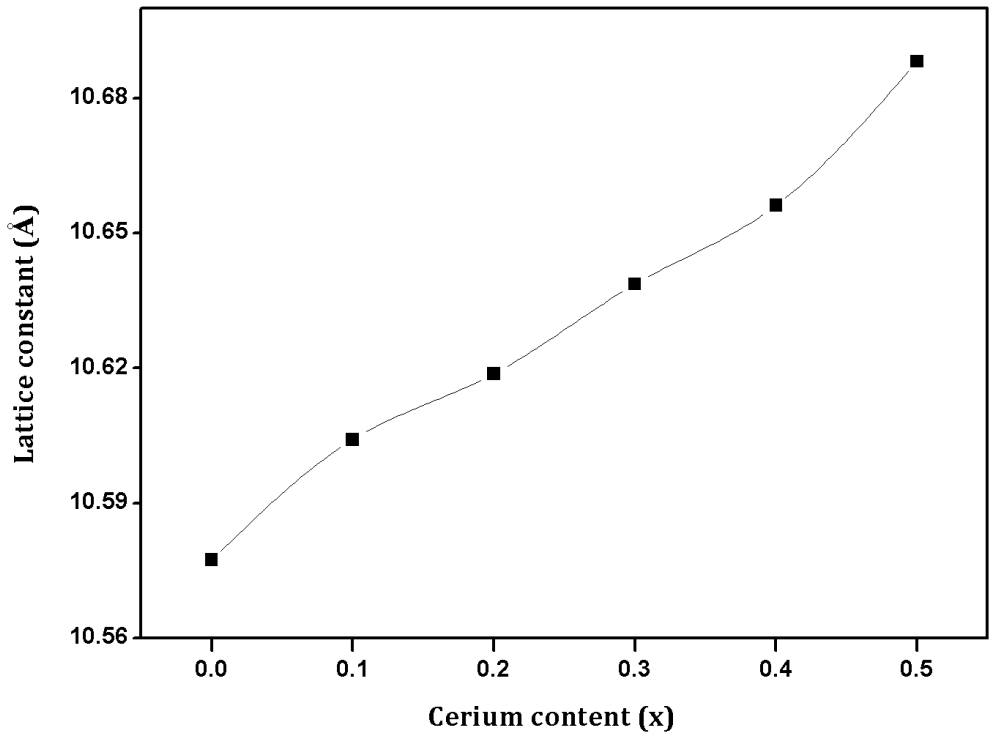

Figure 4-5: Variation of lattice parameter with Ce^{4+} substitution

One characteristic of the pyrochlore structure is that the oxygen ion at 48*f* position has a variable *x*-coordinate, typically in the range 0.3125 to 0.375.

For the disordered fluorite structure this oxygen has an *x*-coordinate 0.375 at a tetrahedral position corresponding to an ideal cubic array of anions. As the 8*a* site in pyrochlore unit cell is vacant, the 48*f* oxygen tends to shift from its ideal tetrahedral position towards the two nearby B-cations leading to a decrease in net B—O bond length. But as the lattice undergoes a disordering, the shift of oxygen towards B cation decreases. This will lead to an increase in *x*-parameter as well as in the B—O bond length.

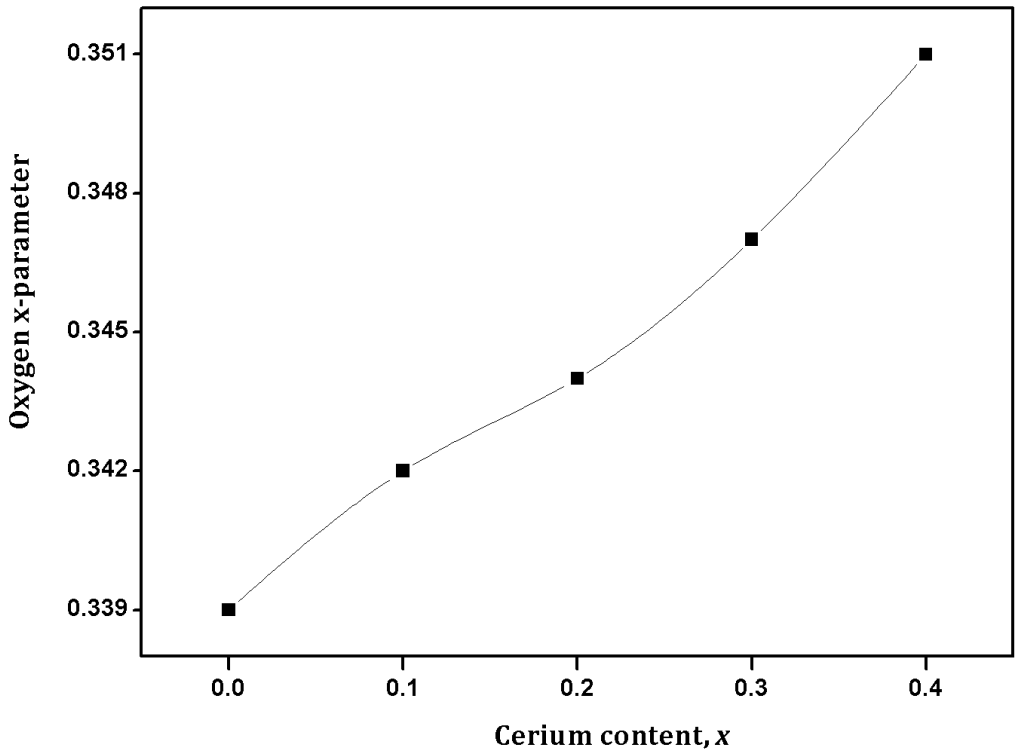

Figure 4-6: Variation of oxygen x-parameter with Ce^{4+} substitution

Figure 4-6 shows a plot of oxygen *x*-parameter as a function of cerium content and Figure 4-7 shows the corresponding variation of B—O bond length. The trend of increase in both the parameters shows the disorder induced by the incorporation of Ce^{4+} in the lattice. Dickson *et al.* showed that the position of 48*f* oxygen strongly influences the (111) Bragg reflection from the crystal and the

intensity of the (111) reflection tends to be zero as the *x*-parameter increases towards 0.375 [Dickson *et al.* 1989]. We have already observed this in Figure 4-1.

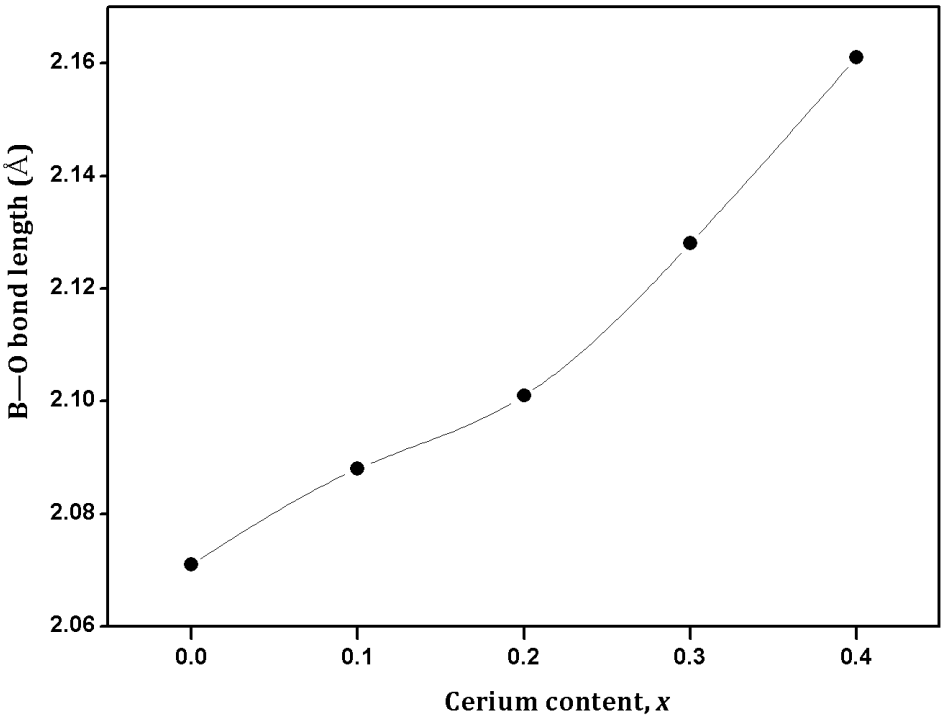

Figure 4-7: Variation of B—O bond length with Ce^{4+} substitution

4.3.1.2. FT Raman Spectroscopy

Glerup *et al.* used Raman spectroscopy as an effective tool for distinguishing an ordered pyrochlore structure from a disordered defect fluorite structure [Glerup, *et al.* 2001]. Since X-ray diffraction is much sensitive to the disorder in the cationic sublattice while Raman spectroscopy is primarily sensitive to the vibrations of the cation-oxygen bonds, the latter can be more instrumental for the study of local disorder. The expected normal modes of vibrations of pyrochlore and fluorite structure are determined using factor group analysis and are widely reported in literature [Glerup, *et al.* 2001, McCauley 1980, N. Kjerulf-Jensen 1996, Poulsen, *et al.* 2000]. Cubic pyrochlores of the general formula $A_2B_2O_6O'$ belong to $Fd\bar{3}m$ space group with Z = 8 and the corresponding

factor group is O_h. The site symmetry for A and B ions is D_{3d}, for O it is C_{2v} and for O' it is T_d [McCauley 1980]. This is a highly ordered lattice where there are three crystallographically different anion sites. Factor group analysis has shown that pyrochlore structure possess six Raman active modes of vibration whose irreducible representations are given as

$$\Gamma(\text{Raman}) = A_{1g} + E_g + 4T_{2g}$$

The origin of these modes and the corresponding wavenumbers are listed in Table 4-2, adapted from reference [Mandal*, et al.* 2010].

Table 4-2: Raman active modes, their origin and corresponding wavenumbers

Symmetry	**Mode of vibration**	**Wavenumber(cm^{-1})**
$\mathbf{E_g}$	B–O_6 Bending	302
$\mathbf{T_{2g}}$	Mostly B–O stretching with mixture of A–O stretching and O–B–O bending vibration	400
$\mathbf{T_{2g}}$	Mostly O–B–O bend with mixture of B–O stretching	507
$\mathbf{A_{1g}}$	Mostly O–B–O bending	520
$\mathbf{T_{2g}}$	Mostly B–O stretching	585
$\mathbf{T_{2g}}$	Mostly B–O stretching	750

Cubic fluorites with general formula AO_2 belong to $Fm\bar{3}m$ space group with Z = 4 and the corresponding factor group is O_h. The site symmetry for A ion is O_h and for O it is T_d [N. Kjerulf-Jensen 1996]. This is a disordered lattice where all the anions are randomly distributed among the eight total anion sites available in the unit cell. Hence all the O ions in a fluorite structure are in crystallographically identical lattice sites. Due to this the Raman spectrum of a

fluorite structure is reduced to a broad continuum of density of states. Only one Raman active mode (T_{2g}) is known in a fluorite structure [Sayed *et al.* 2011].

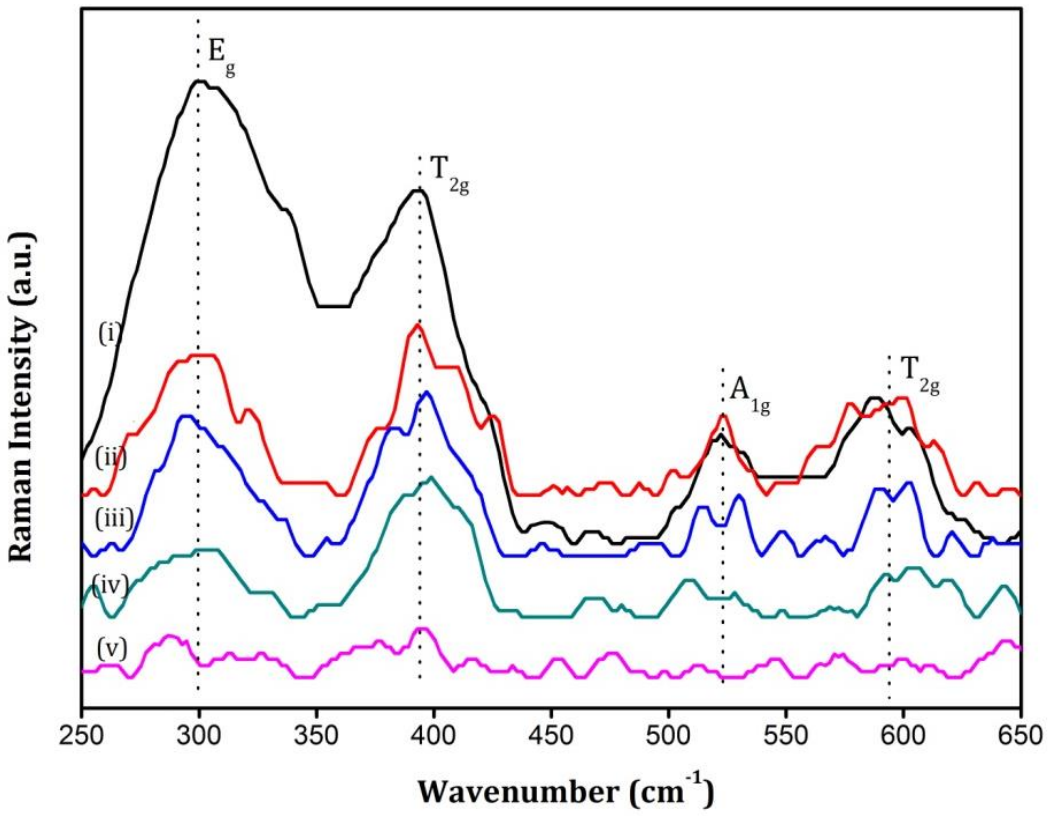

Figure 4-8: Raman spectra of (i) SZC 1 (ii) SZC 2 (iii) SZC 3 (iv) SZC 4 (v) SZC 5

The FT-Raman spectra of various $Sm_2Zr_{2-x}Ce_xO_7$ samples (x = 0.1, 0.2, 0.3, 0.4, 0.5) in the range 250 – 650 cm^{-1} are shown in Figure 4-8. The peaks in the spectra are generally broad which are characteristic of the ordered pyrochlore structure due to inherent deviations from translational symmetry in the lattice [Mandal, *et al.* 2007, Wan, *et al.* 2011]. This broadness is not due to small particle size because the sharp peaks in XRD diagram and also the SEM analysis had shown that the particle size falls in the micrometer range in the present study. The Raman peaks were assigned frequencies following the work of Vandenborre [Vandenborre, *et al.* 1983]. One notable difference in the present work is that we observe a broad peak at around 520 cm^{-1} in some samples whereas Vandenborre

had observed two separate peaks at 523 and 532 cm^{-1}. This superposition of two peaks to appear as a single unresolved broad peak has already been observed at the same position by B. P. Mandal *et al.* [Mandal, *et al.* 2010] in the case of $Nd_{2-y}Y_yZr_2O_7$ system. The predominant bands in the spectra are the E_g band at ~300 cm^{-1}, the T_{2g} bands at ~394 cm^{-1} and ~594 cm^{-1} and the A_{1g} band at ~523 cm^{-1} and other bands were very weak in intensity. The E_g band at ~300 cm^{-1} and the T_{2g} modes at ~594 cm^{-1} are related to the 48*f* oxygen in pyrochlore structures whereas the T_{2g} mode at ~394 cm^{-1} is related to 8*b* oxygen [Qu *et al.* 2007]. Intensity of all these bands tends to diminish with increase in Ce^{4+} content in the lattice. This implies that addition of Ce^{4+} into the lattice disturbs the arrangement of both the 48*f* and 8*b* oxygen ions leading to an overall disorder of anionic sublattice. Qu [Qu, *et al.* 2007] and Mandal [Mandal, *et al.* 2010] in their independent works reported disorder in the zirconate systems with A-site substitution. They observed from the Raman analysis that only the 48*f* oxygen undergoes considerable disorder and the 8*b* oxygen are almost intact with the substitution. But here in the present work, Raman analysis shows that with B-site substitution 8*b* oxygen also undergoes disorder. This may be due to the fact that Raman modes of vibrations in pyrochlores are mostly related to B—O bonds rather than to A—O bonds and B-site substitution makes it more evident in the Raman spectrum.

4.3.2. Morphology

Typical SEM micrographs of thermally etched polished surfaces and the fractured cross sections of three representative samples, x = 0, 0.2 and 0.5 after sintering at 1873 K for 8 hours are shown in Figure 4-9. Visibly, the $Sm_2Zr_{2-x}Ce_xO_7$ samples are relatively dense with a little amount of porosity. The overall morphologies of all the samples are more or less similar. The average grain size falls in the range of a few micrometer. Distinct grain boundaries can also be

identified. The densities of the samples were in the range of 80–85% of theoretical density.

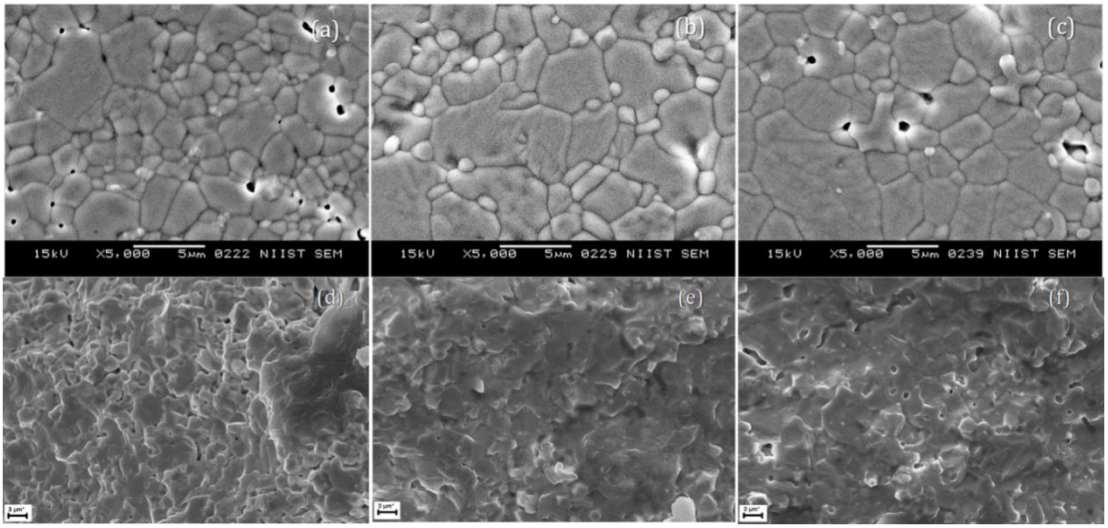

Figure 4-9: Surface morphology of sintered pellets of representative samples (a) SZC 0 (b) SZC 2 and (c) SZC 5; (d), (e) and (f) being the fractured surfaces of the same in order.

4.3.3. Thermal expansion

Influence of temperature on the crystallographic properties of materials is an important factor to be considered if they are to be used for high temperature applications like the fuel cells. Structural stability of a solid sample with respect to temperature is best reflected in its thermal expansion coefficient (TEC). In the present work two methods have been adopted to study the thermal expansion of the samples; high temperature XRD and thermo mechanical analysis (TMA). High temperature XRD study was performed on powder samples at intervals of 200 degrees in a temperature range from 298 K to 1273 K. The expanded view of (222) Bragg reflection of a representative sample SZC 1 to illustrate the evident effect of temperature on unit cell properties is shown in Figure 4-10.

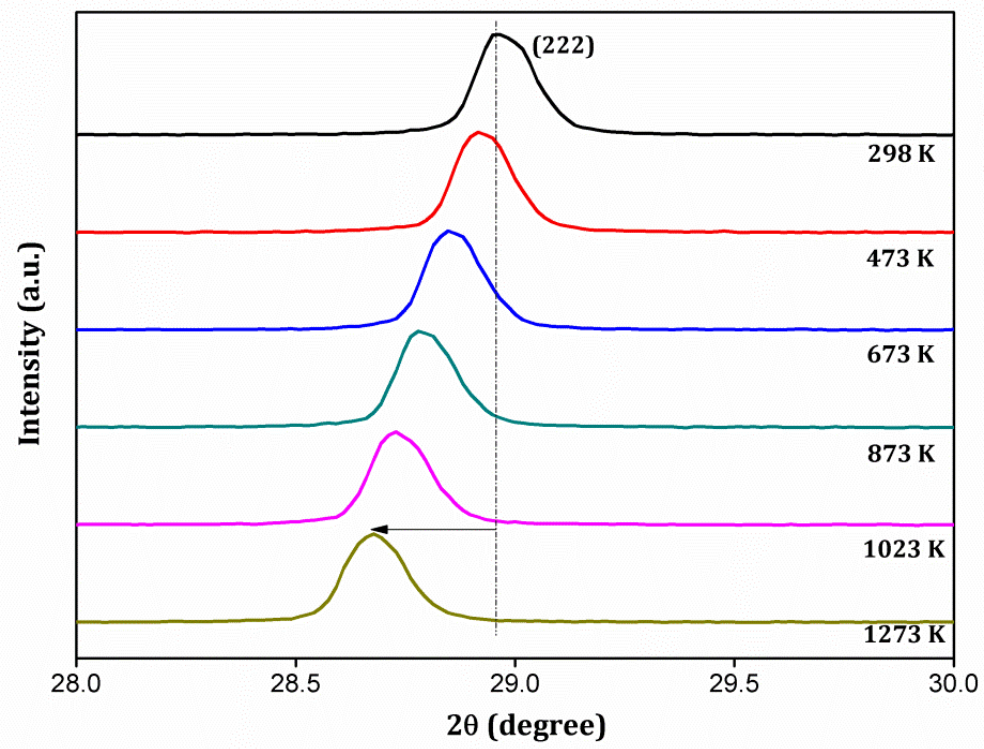

Figure 4-10: Expanded view of the (222) reflection of representative sample SZC 1 at various temperatures

The recorded XRD patterns of each sample at all temperatures were fitted by Le-bail fitting method using commercial X'pert HighScore plus software and the values of lattice parameter were calculated. All the samples retained their respective crystal structures without undergoing any space group transformation. The lattice parameter of all the samples showed a linear increase with an increase in temperature which is also qualitatively evident in the shift of (222) peak in Figure 4-10 towards lower angle side. From the plots of lattice parameter versus absolute temperature, the lattice thermal expansion coefficients were calculated using the equation

$$\propto_{XRD} = \frac{1}{a_{298}}\left(\frac{da}{dT}\right) \qquad (4.1)$$

where $\propto_{XRD}$ is the lattice thermal expansion coefficient, a_{298} is the value of lattice parameter at room temperature and $\frac{da}{dT}$ is the slope of the temperature dependence of lattice parameter. The variation of lattice thermal expansion coefficient, $\propto_{XRD}$, with the doping level of Ce^{4+} is shown in Figure 4-11.

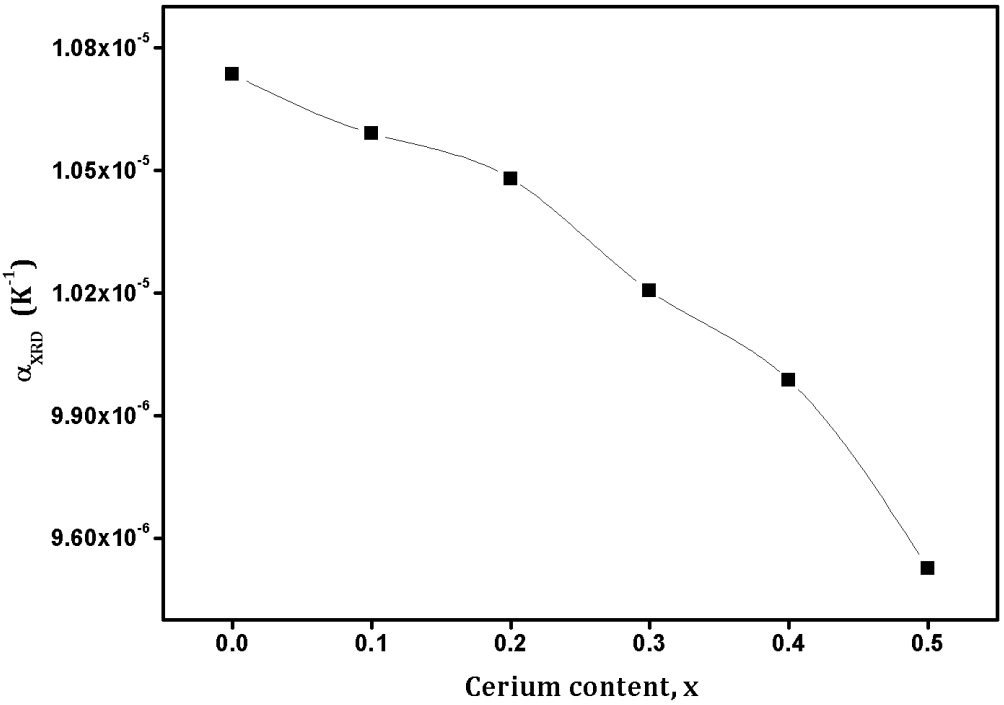

Figure 4-11: Variation of lattice thermal expansion coefficient with Ce^{4+} substitution as yielded by high temperature XRD

Results of high temperature XRD studies give us an idea about the response of the crystal lattice to temperature in the microscopic level, in terms of the unit cell parameters. In order to confirm this trend, a macroscopic approach to the same has been performed by employing thermo mechanical analysis. Bulk samples in the form of sintered cylindrical pellets were loaded in the TMA apparatus and the variation in the linear dimension of the pellets with respect to temperature was studied. The coefficient of expansion was calculated using the equation

$$\propto_{TMA} = \frac{1}{l}\left(\frac{dl}{dT}\right) \qquad (4.2)$$

This equation is in essence similar to equation (4.1) except that this deals with the macroscopic measure of a physical dimension of the bulk sample. A plot of $\propto_{TMA}$ against Ce^{4+} content is shown in Figure 4-12. In this plot too, the thermal expansion coefficient is found to decrease with the increase in amount of Ce^{4+} in the lattice.

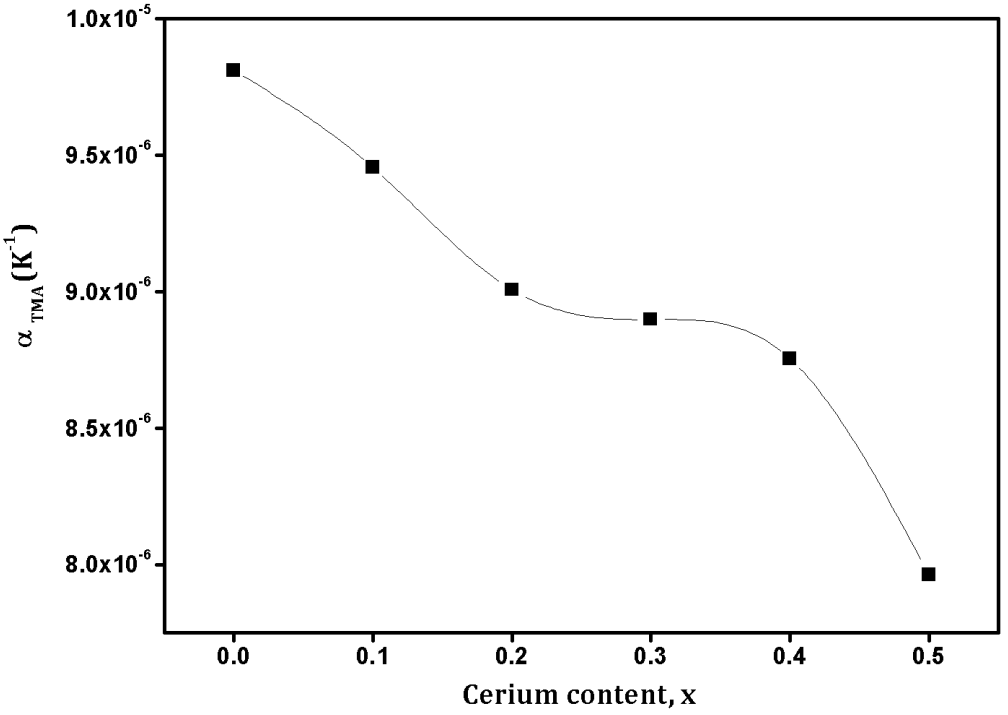

Figure 4-12: Variation of bulk thermal expansion coefficient with Ce^{4+} substitution as yielded by thermo mechanical analysis on sintered pellets

Both high temperature XRD and the TMA results go hand in hand with respect to this trend of decrease in thermal expansion coefficient with Ce^{4+} substitution. This result is opposite to the commonly reported trend of increase in TEC with a decrease in Madelung binding energy [Radhakrishnan*, et al.* 2011, Shimamura*, et al.* 2007]. An increase in *x*-parameter of the 48*f* oxygen negatively affects the Madelung energy [Subramanian*, et al.* 1983] and hence the trend in

Figure 4-6 should imply an increase in TEC with respect to increase in Ce^{4+} content. The reverse trend in this system shall be attributed to the change in diatomic bond energies of B—O bonds. The bond energy of Ce—O bond is (795 ± 8) kJ/mol whereas that of Zr—O bond is (776 ± 13.4) kJ/mol [Lide 2005] implying that the diatomic bond strength of Ce—O bond is greater than that of Zr—O bond. Hence the effect of substitution of Zr^{4+} by Ce^{4+} in $Sm_2Zr_2O_7$ lattice is to increase the ionization energy of the electrons participating in the B—O bond formation. A positive correlation between the exponential of the ionization energy of the bond-forming electrons and the square of the phonon frequency has been theoretically established by A. Arulsamy [Arulsamy 2011] using renormalization group method. This leads to a conclusion that presence of Ce^{4+} in this system increases the phonon frequency resulting into increased rigidity of the lattice and hence lowering the thermal expansion. It can also be inferred that for $Sm_2Zr_{2-x}Ce_xO_7$ systems, the B—O bond energy dominates over the Madelung energy in deciding the thermal expansion properties.

4.3.4. Electrical properties

Electrical behaviour of the materials were studied by applying an *ac* stimulus of 100 mV strength and varying frequency from 1 MHz to 1 Hz across samples in form of cylindrical pellets. The measurements were carried out at various temperatures from 473 K to 1023 K. The complex plane representation of imaginary part of the ac impedance of the sintered pellets against the real part (Nyquist plot) yielded semi-circular arcs characteristic of most of the solid electrolyte systems. Typical impedance spectra of a representative sample SZC 4 at 773 K and 823 K are shown in Figure 4-13. Calculating the capacitance values associated with the semi-circular arcs is a way of understanding the nature of conduction associated with it. For grain conduction the capacitance values are in pF order and for grain boundary conduction they are in nF order [Liu*, et al.* 2010].

Here it could be seen that the high frequency arcs correspond to grain conduction and the low frequency arcs to grain boundary conduction.

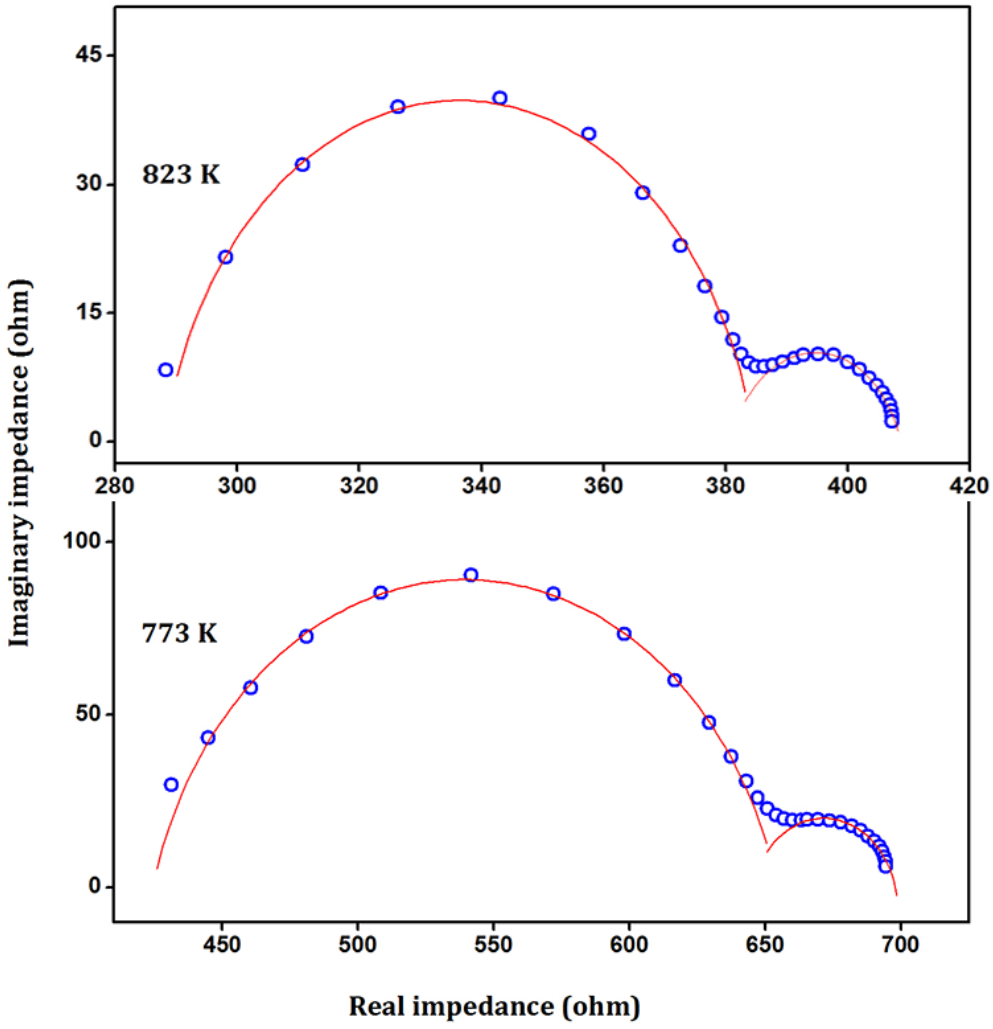

Figure 4-13: Nyquist plots of representative sample SZC 4 at 773 K and 823 K

A slight deviation from the ideal semi-circular behaviour is seen at the low frequency region of the plot. This behaviour is characteristic of certain ionic conductors and is the result of a blocking double layer capacitance at the electrode-sample interface [Sibi *et al.* 2009]. The capacitance values associated with these low frequency points were found to be in typical microfarad order which establishes this point. The intercept of the bulk and grain boundary arcs

with the real axis would respectively yield grain resistance (R_g) and grain boundary resistance (R_{gb}) offered by the samples to the flow of charge across them. The total resistance R_T will be the sum of these two resistive components ($R_T = R_g + R_{gb}$). The total conductivity can then be calculated using the equation,

$$\sigma = \frac{l}{R_T A} \tag{4.3}$$

where l and A represent the thickness and the electroding surface area respectively of the samples.

Apart from the complex impedance (Z*), many other dielectric functions like complex permittivity (ϵ^*), complex electric modulus (M^*) *etc.* are used to describe the electrical properties of solid materials. All these complex functions are related to the dielectric relaxation process in materials and will give rise to semicircle behaviour when their imaginary parts are plotted against the respective real parts. However, the frequencies at which these functions show relaxation behaviour are different from one another. The separation between the relaxation frequencies associated with two different dielectric functions depends on the nature of charge transport within the materials. Variation of real part of permittivity (ϵ') with frequency can give some direct information about this. The strength of dielectric relaxation is given by a parameter, r, defined by the relation [Gerhardt 1994],

$$r = \frac{\epsilon_s}{\varepsilon_\infty} \tag{4.4}$$

Here ϵ_s is the real permittivity when the frequency approaches zero and ε_∞ is the real permittivity when the frequency approaches infinity (when compared to the relaxation frequency of the process). Figure 4-14 shows a plot

of real part of complex permittivity against frequency at three different temperatures.

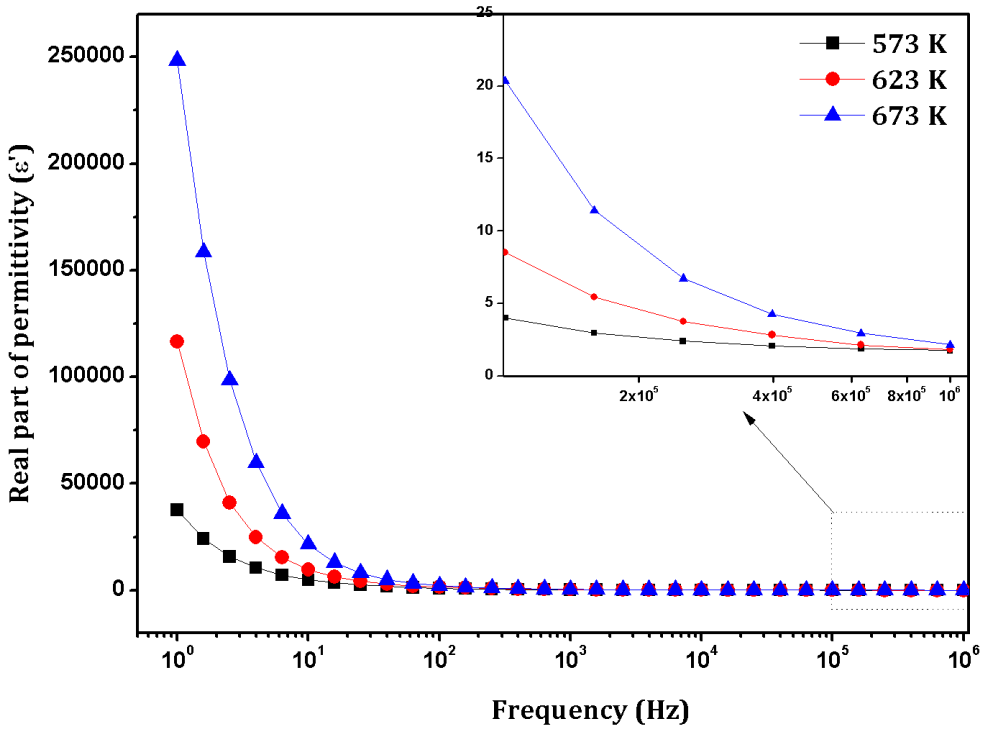

Figure 4-14: A plot of real part of permittivity against frequency, for three different temperatures. Inset shows the expanded view of the same at the highlighted frequency range.

It can be seen that as the frequency increases, the real permittivity decreases. This decrease happens because with increase in frequency, the high periodical reversal of field at the interface helps to reduce the contribution of charge carriers towards the dielectric constant. At very high frequencies, it reaches a saturation value, ε_∞. The low-frequency permittivity is found to increase rapidly with increase in temperature and in figure, with a 100 degree rise in temperature, it has increased up to around 50 times. This implies that with increase in temperature, the strength of relaxation (r) increases. R. Gerhardt proved that high values of relaxation strength is an indication of long range order migration of oxygen ions in ionic conductors [Gerhardt 1994].

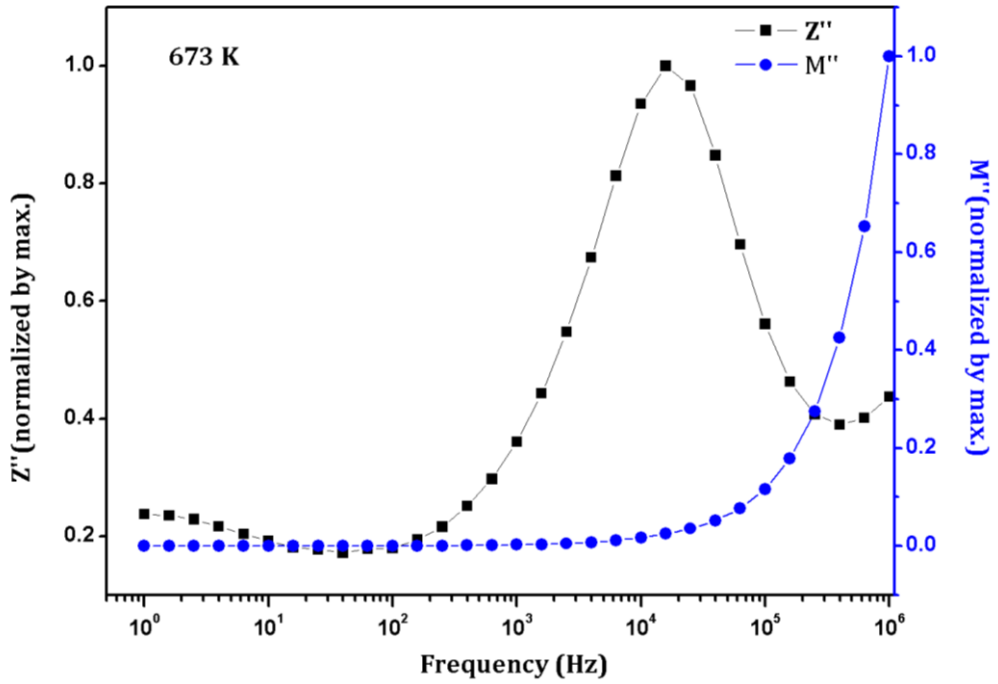

Figure 4-15: Plots of normalized imaginary parts of impedance and electric modulus against frequency at 673 K

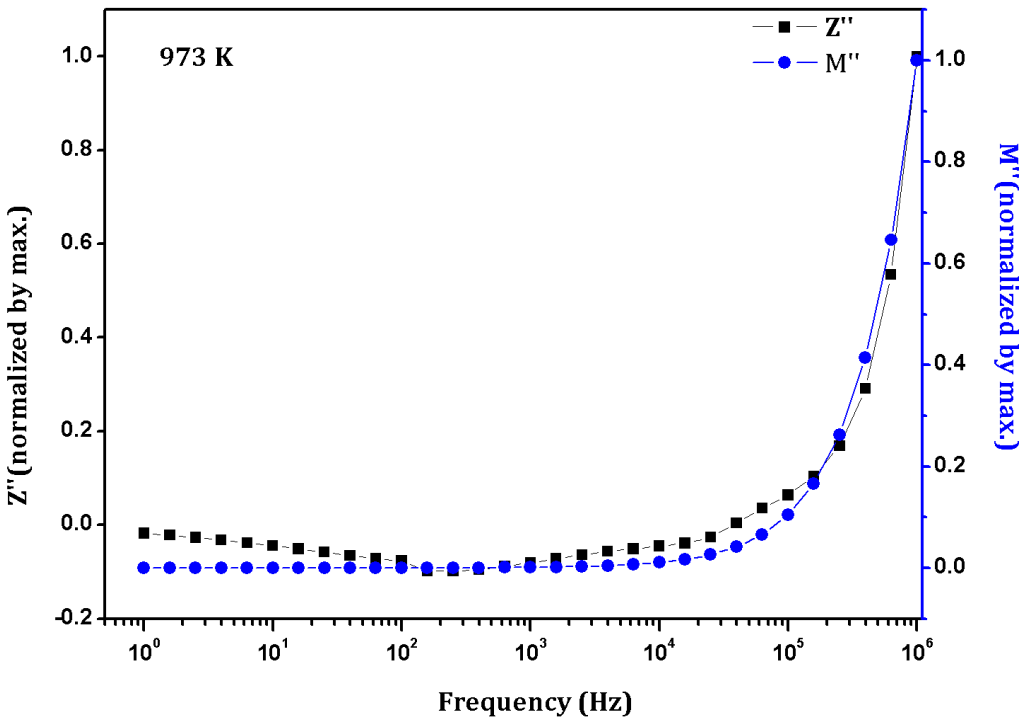

Figure 4-16: Plots of normalized imaginary parts of impedance and electric modulus against frequency at 973 K

Gerhadt developed mathematical expressions which show that, in presence of long range conduction, the relaxations of imaginary parts of electric modulus function and impedance function tend to happen at the same frequencies. Figure 4-15 shows a plot of imaginary part of impedance (Z'') and imaginary part of electric modulus (M''), both being normalized by maximum, plotted against frequency for the representative sample SZC 4. The same plot at a higher temperature is shown in Figure 4-16. A comparison of the two plots reveals that at higher temperature, the relaxation peaks of *Z''* and *M''* tend to merge. This implies that as the temperature increases, localized relaxation behaviour gets dominated over by long range conduction, indicating a thermally activated ionic transport.

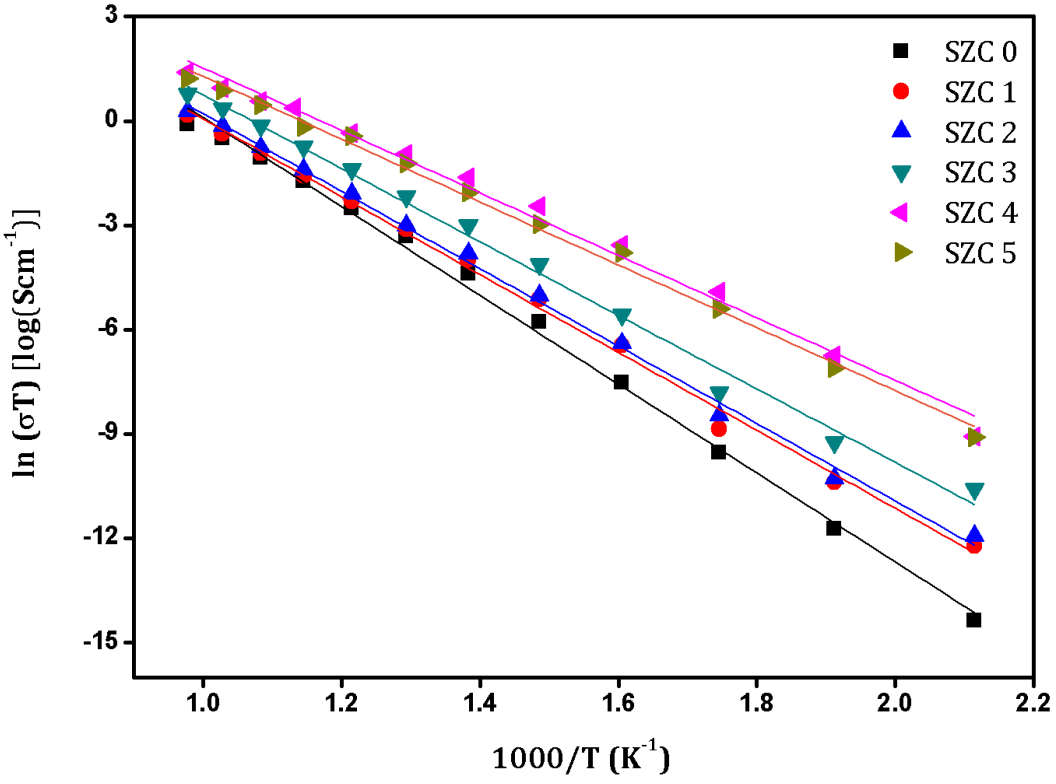

Figure 4-17: Arrhenius plots of $Sm_2Zr_{2-x}Ce_xO_7$ compositions and their linear fit

The activation energy for ionic conduction can be calculated from a plot of $\log_e(\sigma T)$ against $1000/T$. This plot utilizes the linearized form Arrhenius equation,

$$\sigma = \frac{\sigma_0}{T} \exp\left(-\frac{E_a}{kT}\right) \tag{4.5}$$

wherein the slopes of the line is directly proportional to the activation energy, E_a. The Arrhenius plots of various samples is shown in Figure 4-17 and the data could be fit with straight lines using least square fitting method. The slopes of the fitted straight lines give an idea about the activation energy involved. The conduction process by diffusion of oxide ions in $Sm_2Zr_{2-x}Ce_xO_7$ samples is evidently thermally activated with an activation energy that depends on the amount Ce^{4+} doped.

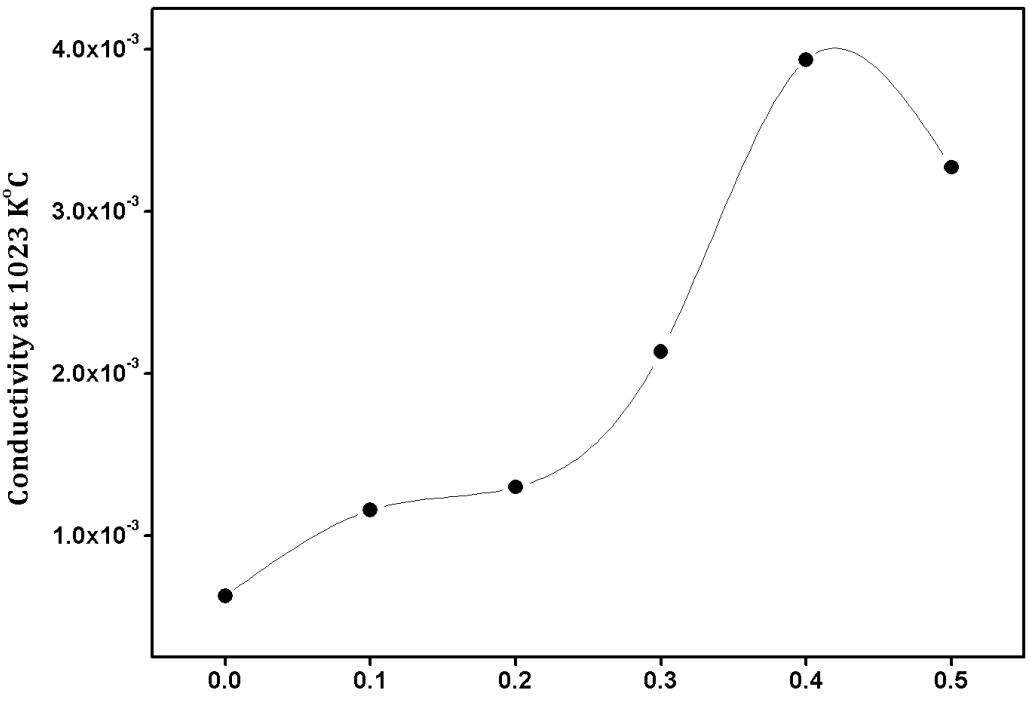

Figure 4-18: Variation of conductivity at 1023 K with Ce^{4+} substitution

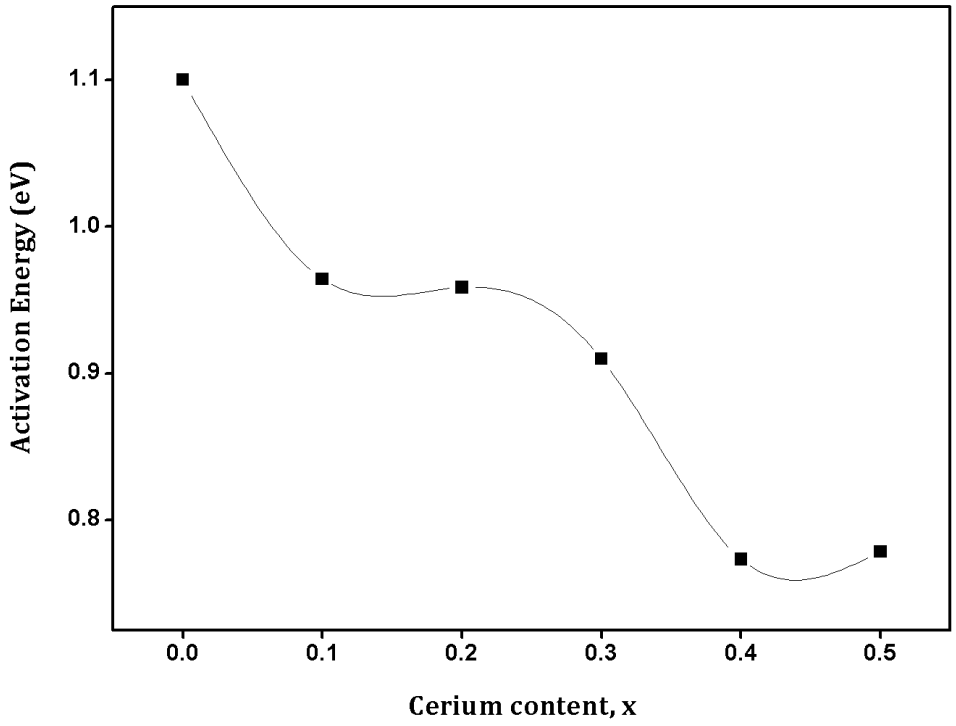

Figure 4-19: Variation of activation energy with Ce^{4+} substitution

Figure 4-18 and Figure 4-19 show the plots of activation energy E_a and total conductivity at 1023 K against the cerium content in the $Sm_2Zr_2O_7$ lattice. As the Ce^{4+} substitution increases, the activation energy shows a decrease from x = 0 to x = 0.4 and beyond that, it begins to increase again. The variation in total conductivity is evidently in accordance with this trend. Conductivity increases with increase in Ce^{4+} content and shows a maximum at x = 0.4. Recalling the discussion on crystal structure, this can be correlated with the lattice disorder introduced by Ce^{4+} in the cubic pyrochlore structure of $Sm_2Zr_2O_7$. In pyrochlore systems most of the ionic conduction is carried out by vacancy hopping mechanism of the 48*f* oxygen [Chen *et al.* 2002, Pirzada*, et al.* 2001]. This conduction process is greatly influenced by the $(\frac{r_A}{r_B})$ ratio and the lattice constant [Yamamura *et al.* 2003]. The decrease in the $(\frac{r_A}{r_B})$ ratio tends to disorder in the lattice and in turn the oxygen vacancy which enables easy hoping of oxide ions

due to creation of equivalent anion sites which minimizes the activation energy for the oxygen hoping in the lattice. In addition, the increase in lattice constant also increases lattice free space (volume). The disordering process relieves the ions off the stringent conditions of Coulombic interactions with the neighbouring cations. This will introduce a decreased energy barrier for the mobile ion transport. Hence both these contributions are accompanied by decrease in activation energy of the oxide ions and it accounts for the considerable decrease in activation energy observed in the present system. But disorder beyond a certain degree can prove to be detrimental to the conductivity as it can increase the ion-ion interaction within the lattice [Garcia-Barriocanal*, et al.* 2009]. This is evident as the increase in activation energy beyond x = 0.4. It can also be noted that this concentration correspond to the boundary of transition from ordered pyrochlore to disordered fluorite structure.

4.4. Conclusion

$Sm_2Zr_{2-x}Ce_xO_7$ system was prepared by solid state reaction route. Addition of Ce^{4+} to the ordered pyrochlore type $Sm_2Zr_2O_7$ lead to the transition to a disordered defect fluorite structure. This is indicated by the disappearance of characteristic pyrochlore superlattice peaks in XRD diagram. Raman spectroscopic studies revealed that the disorder is happening to both cationic and anionic sublattices. The anionic disorder involved both the 48*f* and 8*b* oxygen sites. High temperature XRD and thermo mechanical analysis showed that the substitution also leads to a decrease in thermal expansion coefficient. Impedance spectroscopic analysis revealed that the conduction process in the system is thermally activated obeying the Arrhenius equation. Increasing Ce^{4+} content increased the total conductivity of the system with lattice disorder up to the pyrochlore-fluorite phase boundary and later it decreased for completely disordered structures.

CHAPTER 5

****

Simultaneous Substitution in $(Sm,Zr)_{2-x}(Sc,Ce)_xO_7$ system and its Effect on Structural and Electrical behaviour

****

Simultaneous substitution by two cations in A- and B- sites of $Sm_2Zr_2O_7$ was studied. Substitution caused a disorder with simultaneous decrease in lattice parameter. It was found that both substituents, Sc^{3+} and Ce^{4+}, diffused randomly into both cation sites due to similar ionic radii. Rietveld analysis combined with theoretical models of pyrochlore structure was used to calculate the site occupancies of various ions. Change in rigidity of the inter-ionic bonds with substitution led to decrease in thermal expansion coefficient. The disordering helped to reduce the activation energy up to an extent. But beyond that, the increased cooperative behaviour encouraged by lattice contraction caused the conductivity to decrease.

5.1. Introduction

Substitution in the B-site of $Sm_2Zr_2O_7$ pyrochlore was found to drive a structure transition to disordered defect fluorite structure, and was also influential in enhancing its conducting properties. Since it was found that structural disordering has positive effect on the electrical conductivity, which primarily was a function of radius ratio of the cations, simultaneous substitution of more than one cation can also be expected to have a significant effect on the physical properties of materials. When Yb^{3+} and Sm^{3+} were incorporated together in the A-site of $Gd_2Zr_2O_7$, an order-disorder transition was observed along with considerable enhancement in conductivity [Jia-Hu Ouyang *et al.* 2015]. Ti^{4+} and Sm^{3+}, in barium zirconate had also showed remarkable influence on the electrical, thermal and optical properties [Badapanda *et al.* 2014]. When Ca^{2+} was used as a substituent along with Nb^{5+} and Ta^{5+} independently in $Gd_2Zr_2O_7$, the lattice showed change in lattice order, thermal expansion and electrical conductivity [Radhakrishnan*, et al.* 2011].

Substitution by Y^{3+} in the A-site of $Sm_2Zr_2O_7$ induced structure transition, also enhancing the conductivity. Substitution in the B-site with Ce^{4+} also was advantageous for conductivity up to a certain extent of disorder. For the same parent lattice, co-doping with Gd^{3+} and Yb^{3+} showed that the conductivity was more dependent on the extent of Gd-doping [Liu*, et al.* 2010]. The electrical and thermal expansion behavior of these materials depend strongly on the variation in structure properties and the nature of substituent ions. Here in this work, simultaneous substitution by Sc^{3+} and Ce^{4+} in the form $(Sm,Zr)_{2-x}(Sc,Ce)_xO_7$ is attempted. The variation in structure and thermal expansion properties is monitored and then correlated with the conduction behavior.

5.2. Experimental

The chemical compounds were prepared via conventional solid-state reaction route. Commercially available Sm_2O_3 (Alfa Aesar, 99.99%), ZrO_2 (Aldrich, 99%), Sc2O3 (Alfa Aesar, 99.99%) and CeO_2 (Aldrich, 99.9%) were chosen as the starting materials. Thoroughly mixed reactants were calcined at 1573 K for 6 hours. Calcined pellets were grinded and recalcined at 1873 K for 6 hours. Green cylindrical pellets prepared by uniaxial compaction at 25 MPa were sintered at 1923 K for 24 hours. The crystal structure was analysed using an X-ray powder diffractometer (X'pert Pro, PANalytical). Rietveld refinement using commercial X'Pert Highscore Plus software was employed for a more detailed analysis of the same. Structure analysis was also probed by FT-Raman analysis, by exciting the samples with an argon laser of wavelength 784 nm in a Labram HR 800 spectrometer (Horiba Scientific). The surface morphology of the surfaces of the sintered pellets was analysed via electron microscopic imaging using a scanning electron microscope (JEOL JSM-5600LV). The lattice thermal expansion properties were analysed by high temperature XRD technique in a range of 298 K to 1273 K using an Anton Paar HTK attachment to the X'pert Pro diffractometer. Electrical characterization of the sintered pellets was carried out using an Impedance analyser (Solartron SI 1260) with a dielectric interface (Solartron 1296) in the temperature range 473 K to 1023 K.

5.3. Result and Discussion

The various $(Sm,Zr)_{2-x}(Sc,Ce)_xO_7$ samples for x = 0, 0.1, 0.2, 0.3, 0.4 and 0.5 are labelled as SSZC 0, SSZC 1, SSZC 2, SSZC 3, SSZC 4 and SSZC 5 respectively in the coming sections for brevity.

5.3.1. Crystal structure

5.3.1.1. X-ray diffraction

The powder XRD patterns of the $(Sm,Zr)_{2-x}(Sc,Ce)_xO_7$ samples are shown in Figure 5-1. Monitoring the evolution of reflection pattern with substitution from $x = 0$ to $x = 0.5$ indicates that the substitution process drives a structural change in the lattice. The SSZC 0, which is essentially samarium zirconate, crystallized in its usual pyrochlore phase with space group $Fd\bar{3}m$. But the other end-member is crystallized in fluorite phase with $Fm\bar{3}m$ space group. Hence obviously the substitution-driven disordering of pyrochlore-type lattice is observed in this case.

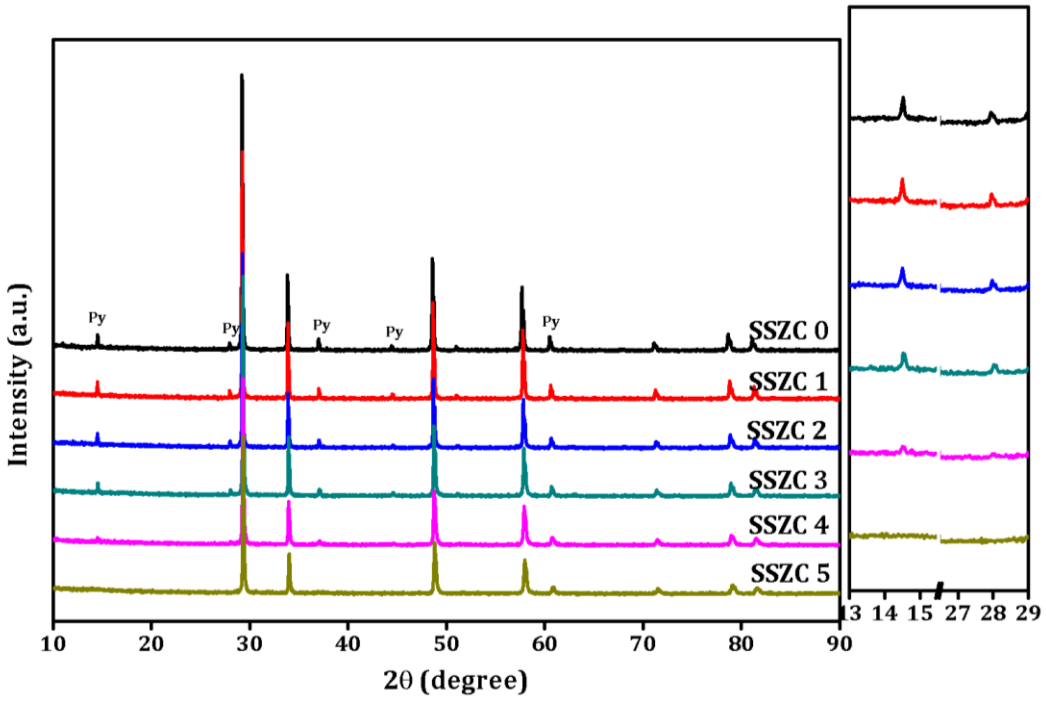

Figure 5-1: Powder X-ray diffraction patterns of various $(Sm,Zr)_{2-x}(Sc,Ce)_xO_7$ samples

The pyrochlore being a superstructure of basic fluorite-type unit cell, its x-ray diffraction pattern consists of all the fluorite reflections plus the superlattice peaks corresponding to the additional miller planes introduced by

the cationic size difference in an ordered lattice. In pyrochlore, the A-site cations are eight-coordinated and the B-site cations are six-coordinated which decides the ionic radii of the respective ions. According to Shannon's estimation [Shannon 1976], the ionic radii of Sm^{3+} and Sc^{3+} under eight-coordination are 1.079 Å and 0.87 Å respectively. On the other hand, Zr^{4+} and Ce^{4+} under six-coordination are estimated to have ionic radii of 0.72 Å and 0.87 Å respectively. Thus the simultaneous substitution of Sm and Zr by Sc and Ce in $(Sm,Zr)_{2-x}(Sc,Ce)_xO_7$ compositions changes the effective ionic radius of A-site cation (r_A) from 1.079 Å for x = 0 to 1.027 Å for x = 0.5, and that of B-site cation (r_B) from 0.72 Å for x =0 to 0.75 Å for x = 0.5. This is changing the radius ratio ($\frac{r_A}{r_B}$) from 1.498 to 1.37, which crosses the pyrochlore stability range which is from 1.78 to 1.46 [Chakoumakos 1984]. The decrease in radius ratio tends to distribute the cations randomly between the A- and B-sites which would affect the scattering efficiency of certain lattice planes. The Miller planes with indices h, k, and l, corresponding to the parent fluorite structure in a pyrochlore diffraction pattern seem to obey the conditions,

$$\begin{aligned} h + k &= 4n \\ k + l &= 4n \\ h + l &= 4n \end{aligned} \qquad (5.1)$$

and these reflections are mostly dependent on the sum of scattering lengths in site A and B. But the superstructure peaks at the 2θ values of ~14°, ~28° , ~37°, ~45° and ~51° do not satisfy these condition and they, instead, depend on the difference in scattering power between A and B cations, distortion in the anionic array *etc.* [Heremans*, et al.* 1995]. As the lattice evolves through a disordering process, the x-ray scattering from these planes decrease and the corresponding

superlattice peaks slowly disappear. This can be clearly seen in the side panel of Figure 5-1.

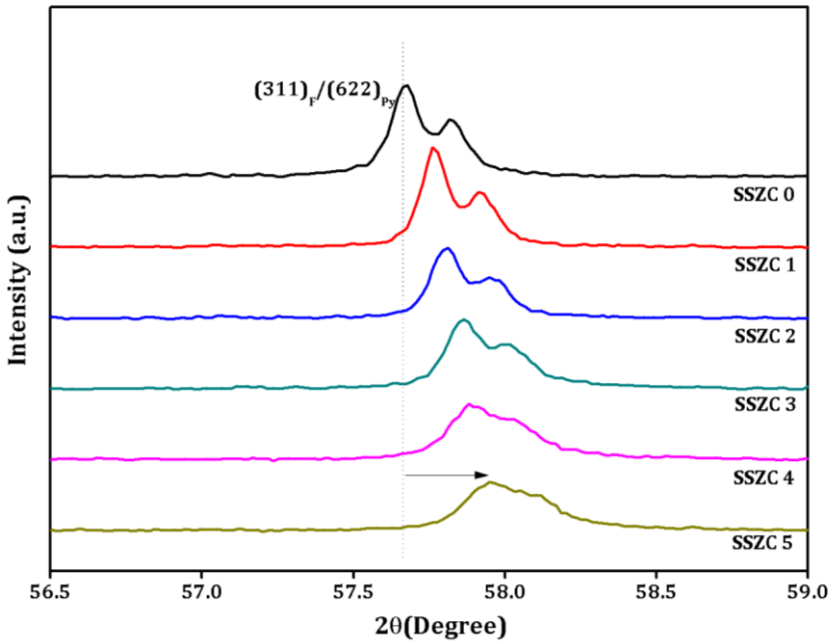

Figure 5-2: Effect of substitution on crystal structure, as evidenced in the $(311)_F/(622)_{Py}$ peak

Figure 5-2 shows the expanded view of $(311)_F/(622)_{Py}$ peak in x-ray diffraction pattern. It can be seen that with substitution, the reflection shifts to higher angles indicating a contraction of the lattice. This trend is opposite to what we have observed in the $Sm_2Zr_{2-x}Ce_xO_7$ system discussed in the previous chapter. There, with Ce-substitution, the lattice was undergoing an expansion apparently due to the larger ionic radius of the substituent. But here in this case, simultaneous substitution with another smaller ion seems to be more influential on the fundamental lattice translation vector.

In the present system, due to the comparable sizes of various ions involved, it is difficult to intuitively assume which ion would occupy which site. Rietveld refinement can help to resolve this issue to a good extent. But since a

large number of permutations of site occupancies of various ions are possible, some theoretical considerations were made simultaneously with Rietveld simulation and refinement. There are some mathematical models to predict the lattice parameter of pyrochlore compositions [Brik and Srivastava 2012, Cai *et al.* 2011]. Among them the most effective one that gives most accurate predictions for most number of known pyrochlore compositions, especially the (3+, 4+)-types, is developed by R. Mouta *et al*. and they put forward the following expression for pyrochlore lattice parameter (a),[Mouta *et al.* 2013]

$$a = \frac{8}{3^{1}/_{2}}\left[1.43373(R_A + R_O) - 0.42931\frac{(R_A + R_O)^2}{R_B + R_O}\right] \qquad (5.2)$$

where R_A, R_B and R_O represent the radii of A-cation, B-cation and the oxygen ion respectively.

Table 5-1: Site occupancies of cations as in $Sm_{2-(y+z)}Sc_yCe_zZr_{2-(y+z)}Sc_zCe_yO_7$ stoichiometry

Net substitution, ($x = y+z$)	***y***	***z***	**Average R_A**	**Average R_B**	**R_O**	**calculated lattice parameter**
0	0	0	1.079	0.72	1.38	10.57702
0.1	0.1	0	1.06855	0.7275	1.38	10.57639
0.2	0.18	0.02	1.0591	0.73375	1.38	10.57382
0.3	0.24	0.06	1.05065	0.73875	1.38	10.56954
0.4	0.27	0.13	1.0437	0.741875	1.38	10.56319
0.5	0.5	0	1.02675	0.7575	1.38	10.56703

A comparison between theoretical calculation and Rietveld refinement indicates that the fraction of Ce^{4+} going into Sm^{3+}-site and that of Sc^{3+} going into Zr^{4+}-site were random. The best match in values of lattice parameter between theoretical calculation and Rietveld refinement, along with the agreement indices

in Rietveld method were used to arrive at the most probable site occupancies of various ions. Assuming the general form of chemical formula for various samples in the present system to be $Sm_{2-(y+z)}Sc_yCe_zZr_{2-(y+z)}Sc_zCe_yO_7$, where partial diffusion of both substituent cations into both cation sites were assumed, the best fit results were corresponding to the values in Table 5-1.

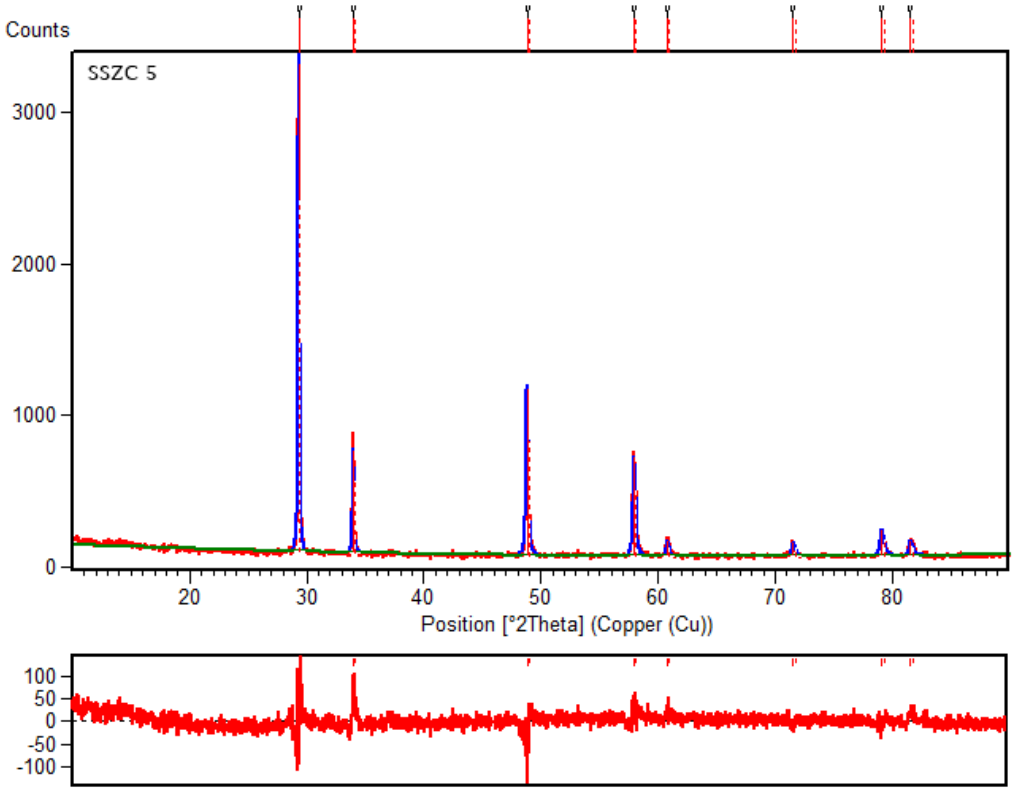

Figure 5-3: Graphical output from Rietveld refinement of SSZC 5, along with difference plot

Rietveld simulation and refinement was carried out using the HighScore plus suit [Degen *et al.* 2014]. Manual indexing of XRD peaks with standard reference pattern available in the ICDD database helped to construct the starting model of structure including space group and estimated lattice parameter. Estimation of atom positions and the respective site occupancies was guided by equation (5.2). A pseudo-Voigt function was used for fitting the diffraction peaks.

Table 5-2: Refined parameters from Rietveld analysis of $(Sm,Zr)_{2-x}(Ce,Sc)_xO_7$ samples

Sample	**SSZC 0**	**SSZC 1**	**SSZC 2**	**SSZC 3**	**SSZC 4**	**SSZC 5**
Structure	Pyrochlore	Pyrochlore	Pyrochlore	Pyrochlore	Pyrochlore	Fluorite
Space group	$Fd\bar{3}m$	$Fd\bar{3}m$	$Fd\bar{3}m$	$Fd\bar{3}m$	$Fd\bar{3}m$	$Fm\bar{3}m$
Specimen Displacement [mm]	-0.114614	-0.014108	-0.002522	-0.088268	-0.039283	0.002951
Flat background	94.04745	96.20512	82.47349	88.94485	81.69617	0.261497
Coefficient 1	-30.27779	-31.20246	-30.59346	-33.81564	-28.93339	0.323178
Coefficient 2	33.91555	38.0872	39.59866	37.11109	33.78223	0.615642
Scale Factor	0.000003	0.000001	0.000001	0.000003	0.000001	0.000001
Lattice parameter [Å]	10.5774(1)	10.5758(2)	10.5718(2)	10.5680(2)	10.5600(4)	5.2756(2)
Oxygen *x*-parameter	0.3250(3)	0.3253(1)	0.3256(3)	0.3261(2)	0.3271(4)	-
U	0.037855	0.062118	0.055956	0.043487	0.268139	0.03873
V	-0.0063	-0.028135	-0.014937	0.006921	-0.126989	0.062284
W	0.004073	0.007982	0.005612	0.002374	0.025913	-0.0057
Peak Shape 1	0.72352	0.768115	0.829476	0.649457	0.915014	0.552707
Peak Shape 2	0.00475	-0.001205	-0.001469	0.005516	-0.00363	0.004717
R_{exp}	8.65	8.63	9.25	8.89	9.3	9.5
R_p	8.21	9.49	10.11	8.71	9.82	9.56
R_{wp}	10.42	12.39	12.96	11.51	12.58	11.98
GOF	1.45	2.06	1.96	1.67	1.83	1.59

Unit cell characteristics including the lattice constant and oxygen *x*-parameter were refined along with other fitting parameters like scale factor, Caglioti functions, flat background and peak shape functions. The agreement indices showed that the best possible fits were achieved. Various refined parameters are listed in Table 5-2 and the graphical output for one representative sample is shown in Figure 5-3. Refinement yielded precise values of lattice parameter and oxygen x-parameter. The variation of observed lattice parameter as obtained from Rietveld refinement and that of the predicted theoretical lattice parameter as plotted against the extent of substitution, *x* is shown in Figure 5-4.

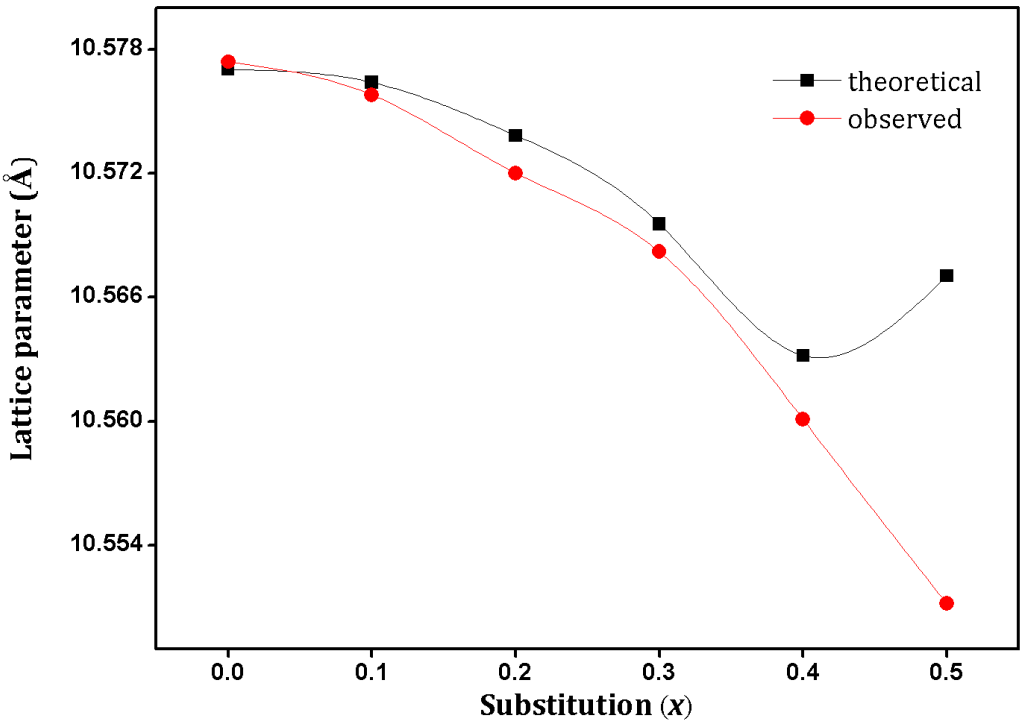

Figure 5-4: Variation of theoretical and observed lattice parameter with substitution

It can be seen that decrease in lattice parameter observed in the present system is in accordance with the trend predicted by theoretical considerations. The difference between predicted and observed values increases with increase in substitution, and for $x = 0.5$ the difference is very large. This is justifiable since,

the theoretical model does not take into account the disordering process that is happening parallel to the lattice contraction in the present system. It should be remembered that the last data point corresponds to $Fm\bar{3}m$ space group of lattice, while the theoretical expression used for calculation of lattice parameter assumes it to be $Fd\bar{3}m$. As the lattice transforms into a different space group altogether during substitution, there are obvious limitations for the actual lattice parameter values to be exactly close to the predicted ones.

Since the disordering process is best reflected in the oxygen *x*-parameter, variation of x-parameter was also monitored. As a theoretical aid for knowing the range of unknown oxygen positional parameter mathematical inequalities formulated by Nikiforov was used. Those relations are reproduced as follows from literature [Cai*, et al.* 2011]:

$$\frac{1}{2}R_O\frac{\sqrt{2}}{a} \geq x \geq \frac{2R_O}{a} \tag{5.3}$$

$$\frac{3}{8}-\frac{1}{8}\left[3\left\{\frac{(R_B+R_O)}{R_A+R_O}\right\}^{1/2}-2\right]^2 \geq x \geq \frac{3}{8}-\left[\left\{\frac{(R_B+R_O)}{a}\right\}^2-\frac{1}{32}\right]^{1/2} \tag{5.4}$$

These equations assume the origin to be at the 8*b*-oxygen site. Since in the present thesis we have been referring to the 16*c* site of B-cation to be the origin, we shall use the following relation for converting the *x*-value to a B-origin lattice,

$$x_{16c} = \frac{5}{8} - x_{8b} \tag{5.5}$$

Figure 5-5 shows the variation theoretically predicted and observed values of *x*-parameter with substitution.

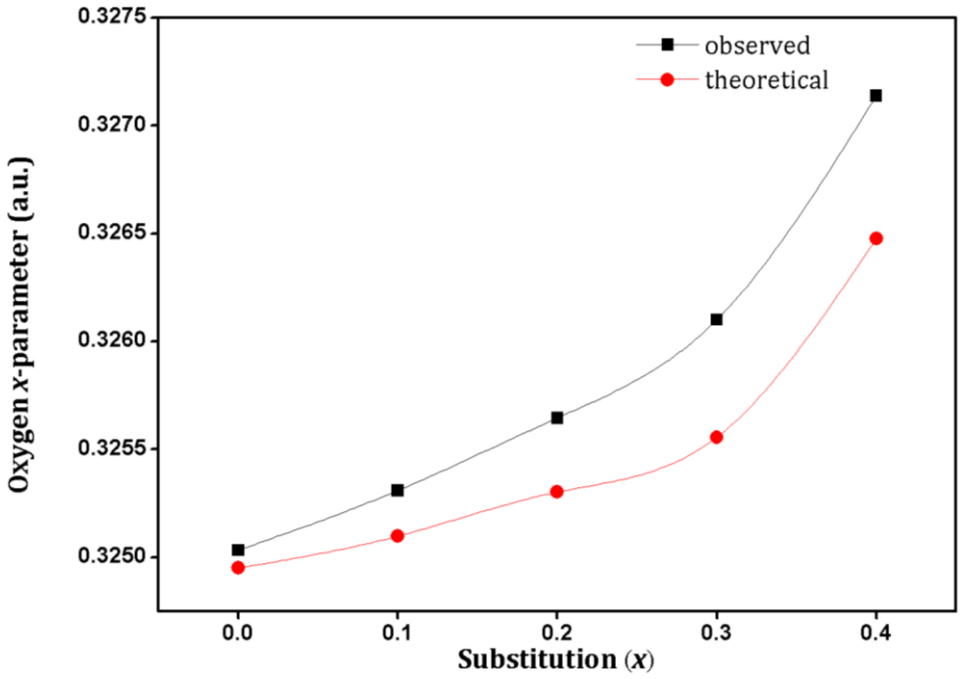

Figure 5-5: Variation of theoretical and observed values of oxygen x-parameter with substitution

The trend of *x*-parameter is found to follow the predicted increase with substitution. However, as in the case of lattice parameter, the values of observed and predicted *x*-parameters are slightly different from one another. This is a commonly observed variation, and has been reported to be unimportant as far as the trend in variation is concerned [McCauley 1980, Radhakrishnan*, et al.* 2011]. In effect, the increase in variable positional parameter of oxygen clearly indicates that the lattice is disordering. The extent of disorder is comparatively more compared to the B-site substitution in the previous chapter since the decrease in radius ratio is faster due to simultaneous substitution on both A- and B-sites.

5.3.1.2. FT-Raman analysis

The scattered x-rays from which we deduce various structural aspects of the scattering crystal is mostly contributed by the cations in the lattice since the oxygen ions are very poor scatterers of x-rays when compared to the heavy metal

ions. Hence the disorder inferred from x-ray diffraction pertains only to the cationic sublattice alone. Raman spectroscopy on the other hand is a better tool to determine local disorder as it is sensitive to the vibrations of cation-oxygen atomic bonds. Cubic pyrochlores of the form $A_2B_2O_7$ ($Fd\bar{3}m$, O_h^7) with Z = 8 is reported to possess six Raman active modes whose irreducible representations are expressed as

$$\Gamma(\text{Raman}) = A_{1g} + E_g + 4T_{2g}$$

Whereas, cubic fluorites of the general form AO_2 ($Fm\bar{3}m$, O_h^5) with Z = 4 has only one Raman active mode given by,

$$\Gamma(\text{Raman}) = T_{2g}$$

Due to this drastically different behaviour in Raman scattering for these two crystal structures, a disordering process can be easily understood with the help of Raman spectroscopy.

Figure 5-6 shows the FT-Raman spectra of various SSZC samples recorded in the wavenumber range of 200 – 800 cm^{-1}. Various distinct peaks corresponding to different vibrational modes can be distinguished in the spectra. The peaks are generally broad in nature. This happens due to the inherent disorder present in pyrochlore crystals. Even in an ordered crystal, some amount of disorder is always present in the form of vacancy, defects, foreign atoms *etc*. which would break down the translational periodicity. This can lead to considerable dispersion in a phonon branch leading to line broadening. Since we have not utilized a single-crystal and polarized Raman spectroscopy, assignment of vibrational modes to different peaks is a non-trivial task. However lattice dynamic calculations done one similar systems can be extended here which would enable to identify the most conspicuous modes in the present pyrochlore

system [Gupta and Brown 2003, Scheetz and White 1979]. Work of Vandenborre *et al.* is often referred to in the literature for assigning vibrational modes, especially in probing disorder in pyrochlores [Mandal, *et al.* 2007, Sayed, *et al.* 2012, Vandenborre, *et al.* 1983].

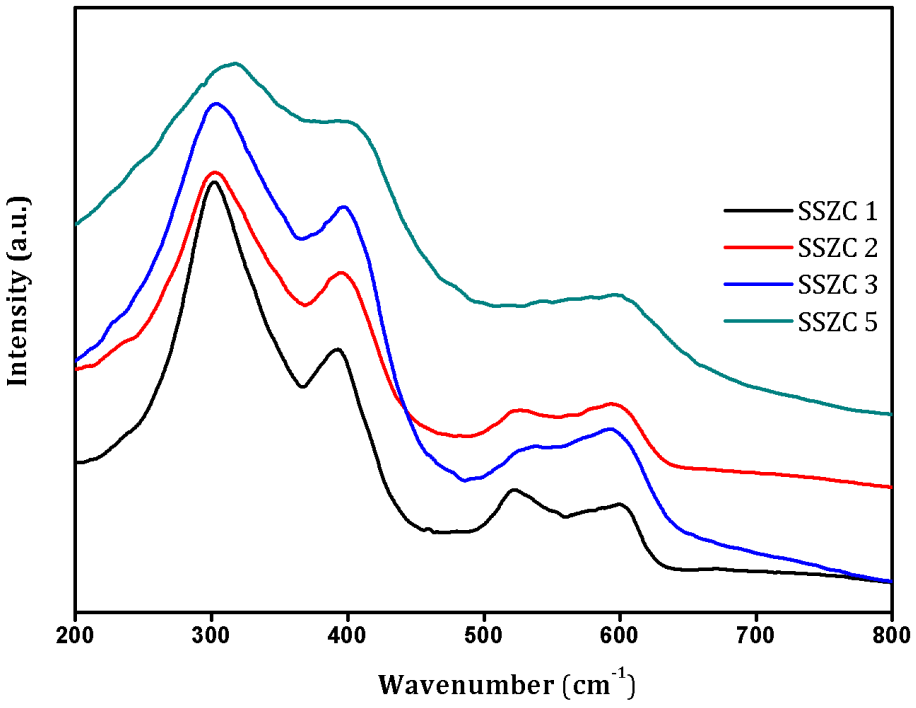

Figure 5-6: FT-Raman spectra of various SSZC samples

The distinct vibrational modes of $(Sm,Zr)_{2-x}(Ce,Sc)_xO_7$ in Figure 5-6 could be identified as the E_g band at ~300 cm^{-1}, the T_{2g} bands at ~393 cm^{-1} and ~596 cm^{-1} and the A_{1g} band at ~523 cm^{-1}. It can also be observed that with increase in substitution, all the vibrational modes undergo broadening and a decrease in intensity. The E_g mode and the T_{2g} mode at ~596 cm^{-1} are related to the vibrations of the 48*f*-anion and an increase in width of these modes indicates an increasing degree of disorder in 48*f*-oxygen sites. The other T_{2g} mode at 393 cm^{-1} is the only mode related to the 8*b* oxygen which is also indicating an increasing structural disorder with substitution. Thus, as in the case of the previous system,

simultaneous substitution on both A- and B-sites induces disorder to the total anionic sublattice involving both 48*f* and 8*b* oxygen ions.

5.3.2. Morphology

The morphology of the samples prepared in the form of dense cylindrical pellets, sintered at 1923 K, was analysed in a scanning electron microscope. The samples showed typical polycrystalline nature, with grains falling in a range of 3–6 μm in size. Distinct grain boundaries could also be observed. All the samples had a certain amount of porosity, as can be seen in Figure 5-7. The densities of all the samples were around 85% of the theoretical density.

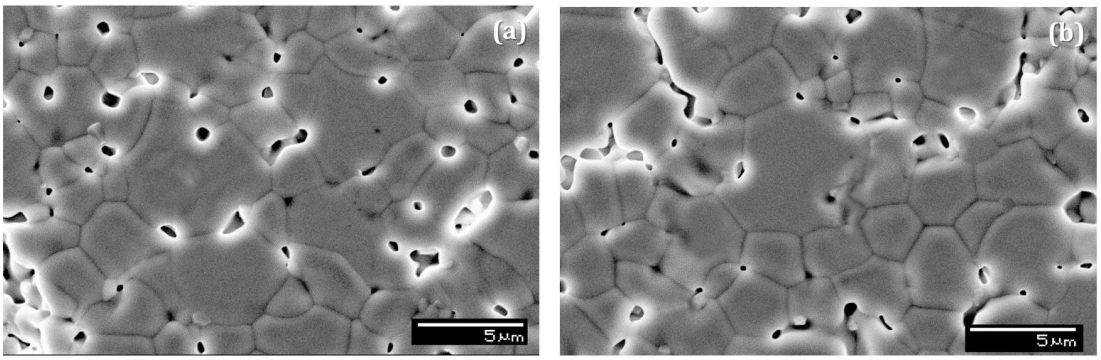

Figure 5-7: Scanning electron microscopic images of the polished surfaces of two representative samples (a) SSZC 1 (b) SSZC 5

5.3.3. Thermal expansion

A more detailed picture about the structural aspects of crystals can be achieved if we analyse the response of the lattice to change in temperature. Moreover, structural stability in high temperature and thermal expansion are essential parameters to be considered for materials that are to be tried as solid oxide electrolytes. Thermal expansion behaviour of these materials were investigated by using high-temperature x-ray diffraction. XRD patterns of all samples were recorded at varying temperatures from ambient temperature to 1273 K, at intervals of 200 degrees. At all substitutions, the samples retained their

diffraction pattern intact during the entire range of measurement temperatures indicating the absence of any structure transition at elevated temperatures. However, there are mainly two aspects in the XRD pattern of all the samples that reflect the influence of substitution and that of change in temperature. One is the scattering intensity and the other is angular position of the scattering peaks.

The intensity of scattered x-rays depends on the scattering power of the ions, which is proportional to the density of electron clouds around them. As the temperature increases the ions undergo lattice vibrations about their equilibrium positions. This would affect the spatial distribution of electronic charge in the lattice and hence also the scattered intensity. The more the amplitude of vibrations, the more will be the decrease in charge density. Since the amplitude of vibrations will be directly proportional to the amount of thermal energy, intensity of the x-ray diffraction peaks diminish with increase in temperature.

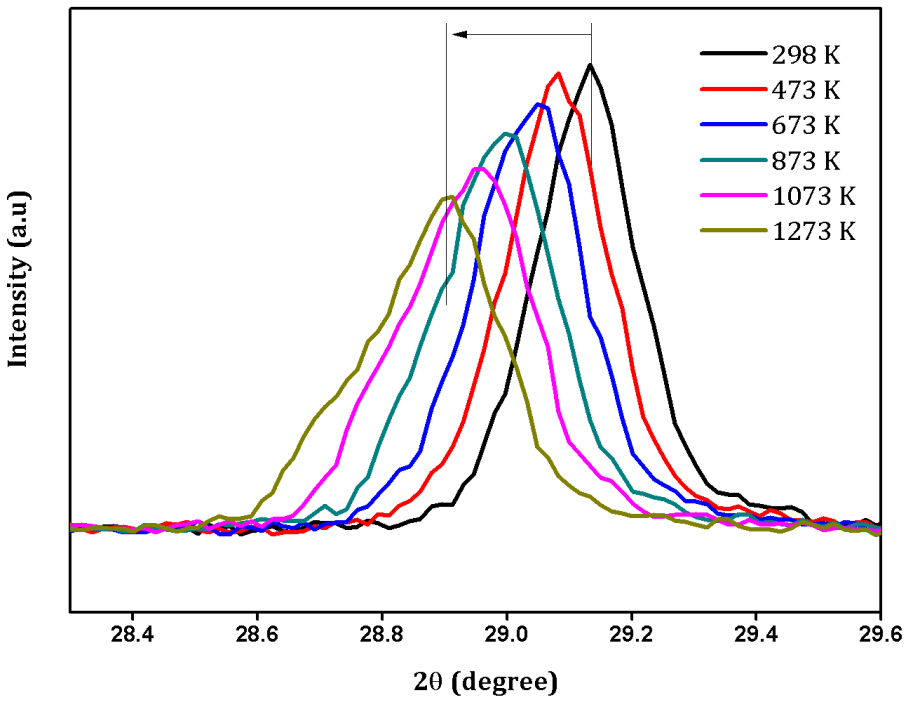

Figure 5-8: Evolution of (222) XRD peak of representative sample SSZC 3 with increase in temperature

Figure 5-8 shows the (222) reflection of a representative sample SSZC 3 at various temperatures. It can be seen that the diffraction peaks shift towards lower angles with increasing temperature. This indicates an increase lattice parameter with temperature implying the thermal expansion behaviour. The XRD patterns of all the samples were analysed by Le-bail fitting method, which yielded the values of lattice parameter at various temperatures.

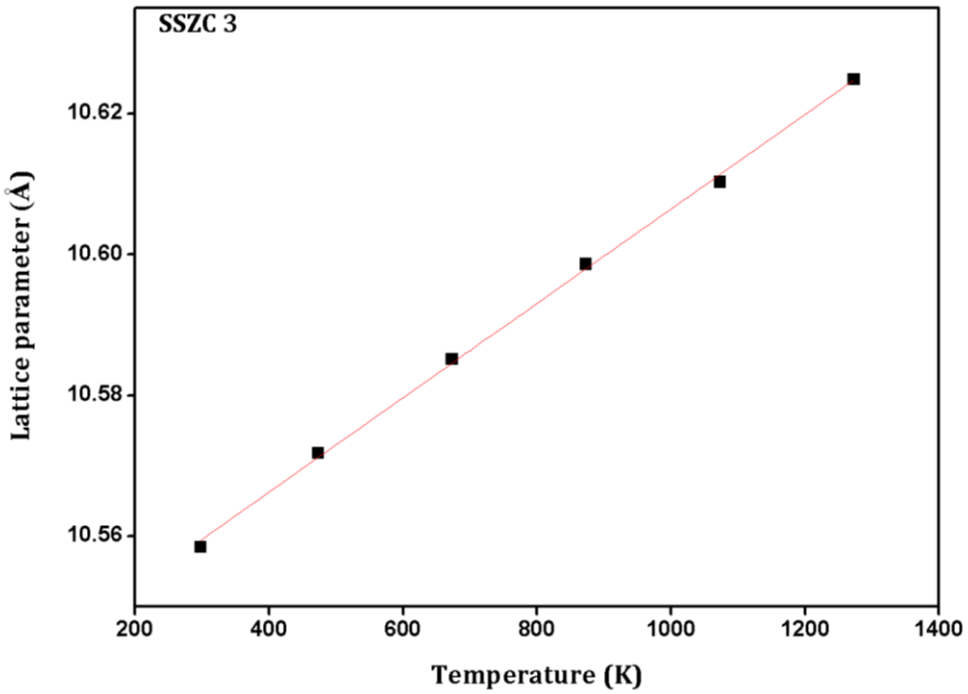

Figure 5-9: Variation of lattice parameter with temperature for SSZC 3 sample

A plot of lattice parameter *vs.* temperature for SSZC 3 is shown in Figure 5-9, which shows a linear increase according to the equation ($y = 10.539 + 6.699x$). Using the slope of the lattice parameter variation ($\frac{da}{dT}$) and the lattice parameter at room temperature (a_{298}), the lattice thermal expansion coefficient ($\propto$) can be calculated using the equation,

$$\propto = \frac{1}{a_{298}}\left(\frac{da}{dT}\right) \qquad (5.6)$$

The variation of lattice thermal expansion property with substitution is shown in Figure 5-10. It can be seen that as the substitution increases, thermal expansion coefficient decreases.

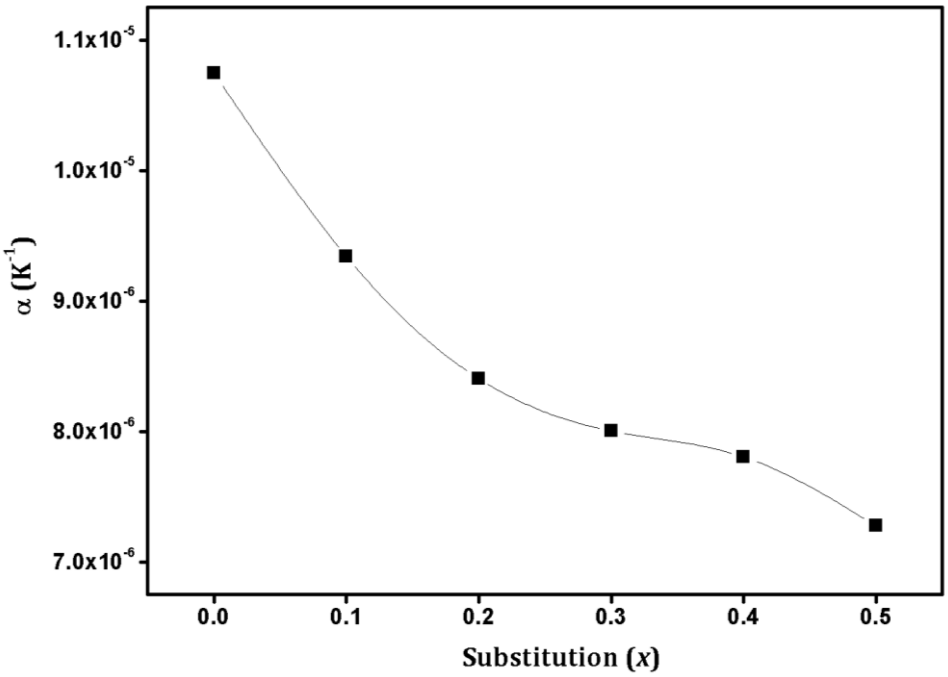

Figure 5-10: Variation of thermal expansion coefficient with substitution

Shimamura *et al.* observed that the thermal expansion in pyrochlores depends on the Madelung binding energy [Shimamura*, et al.* 2007]. They report that as the Madelung binding energy increases, thermal expansion decreases. But it is known that, as the *x*-parameter in pyrochlore increases, the Madelung binding energy decreases [Subramanian*, et al.* 1983]. According to this, the thermal expansion in the present system should increase with increase in substitution since we have observed an increase in *x*-parameter here. The decrease in thermal expansion can be explained by acknowledging the change in rigidity of cation-oxygen bonds in the $Sm_2Zr_2O_7$ lattice with substitution. When Sm^{3+} and Zr^{4+} got partially substituted by Sc^{3+} and Ce^{4+} respectively, the nature of bonds should also change. The diatomic bond energies of Sm—O, Sc—O, Zr—O

and Ce—O bonds are (565 ± 13) kJ/mol, (681.6 ± 11.3) kJ/mol, (776.1 ± 13.4) kJ/mol and (795 ± 8) kJ/mol respectively [Lide 1994]. Thus, the diatomic bond energies of bonds between substituent cations and oxygen are stronger and hence both the average A—O and average B—O bond become stronger with substitution. This makes the lattice less susceptible to expansion at high temperatures.

5.3.4. Electrical properties

A small ac stimulus of 100 mV was applied across the samples prepared in the form of thin cylindrical pellets in order to study the response of the materials. Although the practical application of these chemical systems are mostly in dc electricity, ac stimulus is used since it can throw light on to some of the physical aspects of the electrical conduction mechanism. Impedance spectroscopy primarily measures the ac impedance offered by the samples.

As far as polycrystalline materials are concerned, there are primarily two mechanisms of charge transport within them. One is the usual charge diffusion overcoming a pure ohmic resistance and the other is a tendency of the charges to get accumulated somewhere thereby giving rise to a capacitive reactance to the current. Depending on the sites where charge accumulation can take place - whether it is within the bulk, in the grain boundaries or in the interfaces- the associated capacitance values can differ. The capacitance associated with the bulk of the materials often falls in picofarad range, whereas at the grain-boundaries and sample-electrode interfaces they happen to be in nanofarad and microfarad range respectively. Since the relaxation frequencies associated with these mechanisms will be different from one another, a polycrystalline sample is almost analogous to a series of three RC-parallel circuits.

Figure 5-11 shows the typical complex plane representation of ac impedance of a representative sample SSZC 5 at three different temperatures. Different semi-circular regions can be distinguished in the plot at all temperatures, and they correspond to different mechanism of charge transport within the samples. Depending upon how separated the different relaxation frequencies in the applied ac spectrum are, the semicircles may appear well-resolved, merged or incomplete. Most often, at some temperatures some portions of the semicircle may lie outside the experimental range of frequencies thereby appearing incomplete. At high temperatures, the charge accumulation at the electrode-sample interface may give rise to high capacitance which would cause the semicircles to be dominated over by vertical spikes in the complex plane.

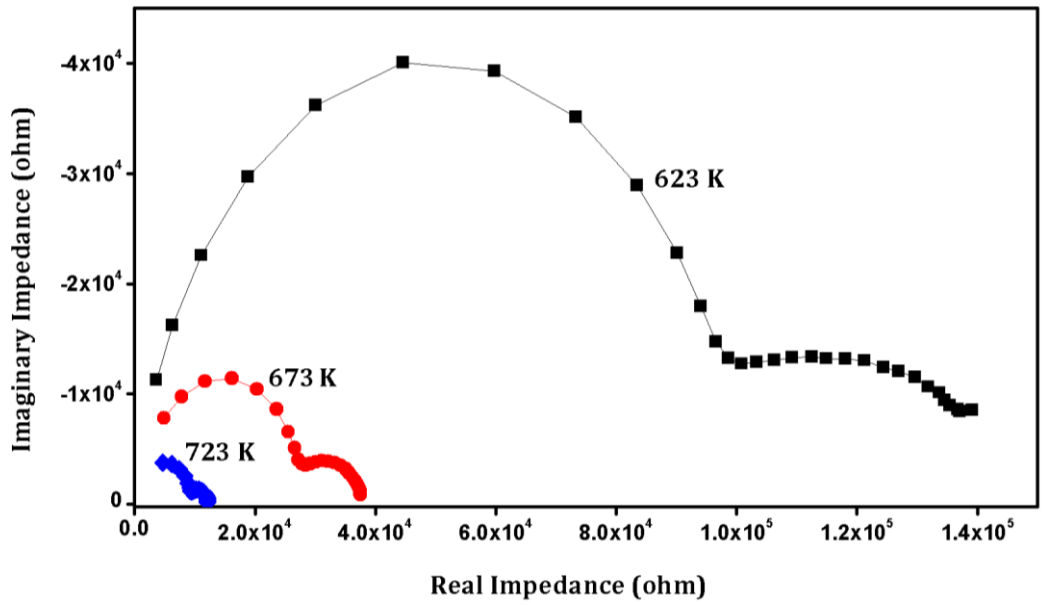

Figure 5-11: Nyquist plots of SSZC 5 at three different temperatures

The intercept of a semicircle with the real axis gives the resistance associated with that particular mechanism. In the present work, since the individual semicircles were not always well resolved, the total resistance (R) involving the contribution from both grain and grain-boundary conditions was

considered. Using the area of electroding (A) and the sample thickness (l), the conductivity (σ) of the samples could be calculated using the equation,

$$\sigma = \frac{l}{RA} \tag{5.7}$$

The temperature-dependent variation in conductivity was analysed by plotting $\log_e(\sigma T)$ against $1000/T$. All the samples showed a linear trend of conductivity with temperature as shown in Figure 5-12 where the straight lines represent the linear mathematical fits of data points. This implies that the conductivity obeys Arrhenius equation for thermally activated processes.

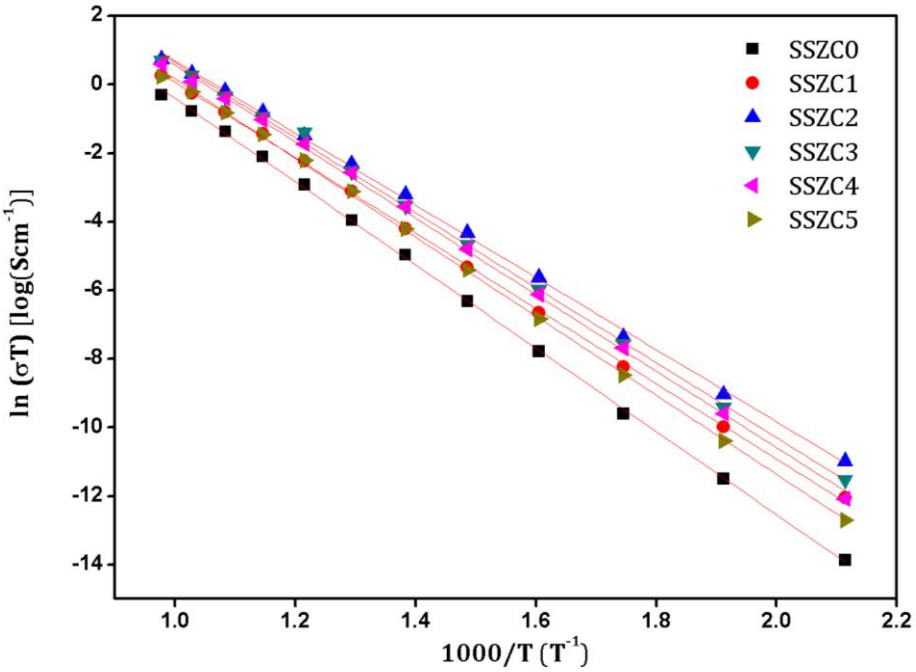

Figure 5-12: Arrhenius plots of SSZC samples along with their straight-line fit

The activation energy for conduction in samples can be calculated from the slopes of the respective Arrhenius plots. The change in activation energy with substitution and the corresponding variation in conductivity at the highest measuring temperature (1023 K) are shown in Figure 5-13 and Figure 5-14 respectively.

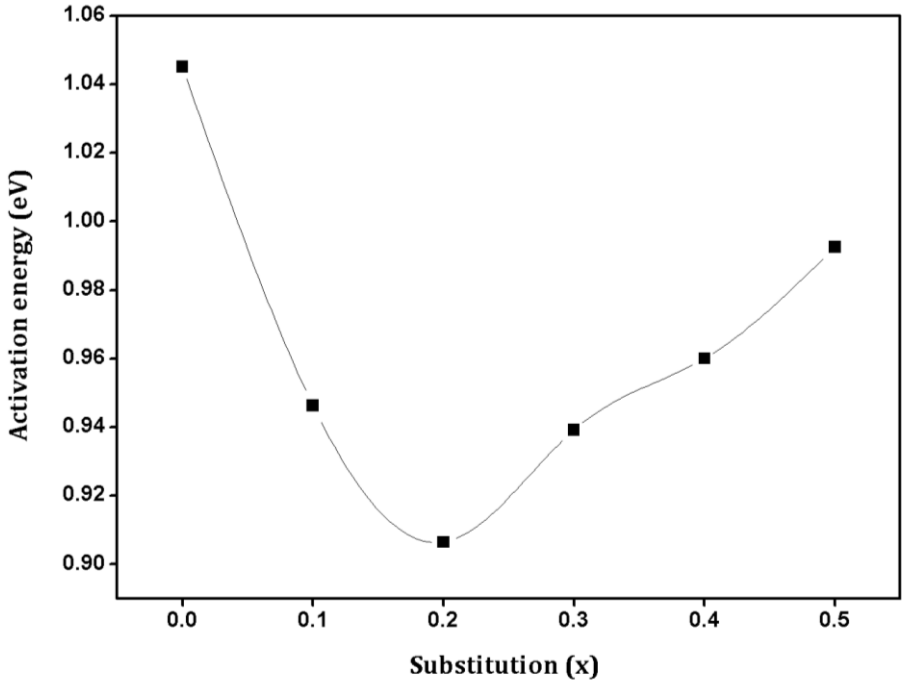

Figure 5-13: Variation of activation energy with substitution

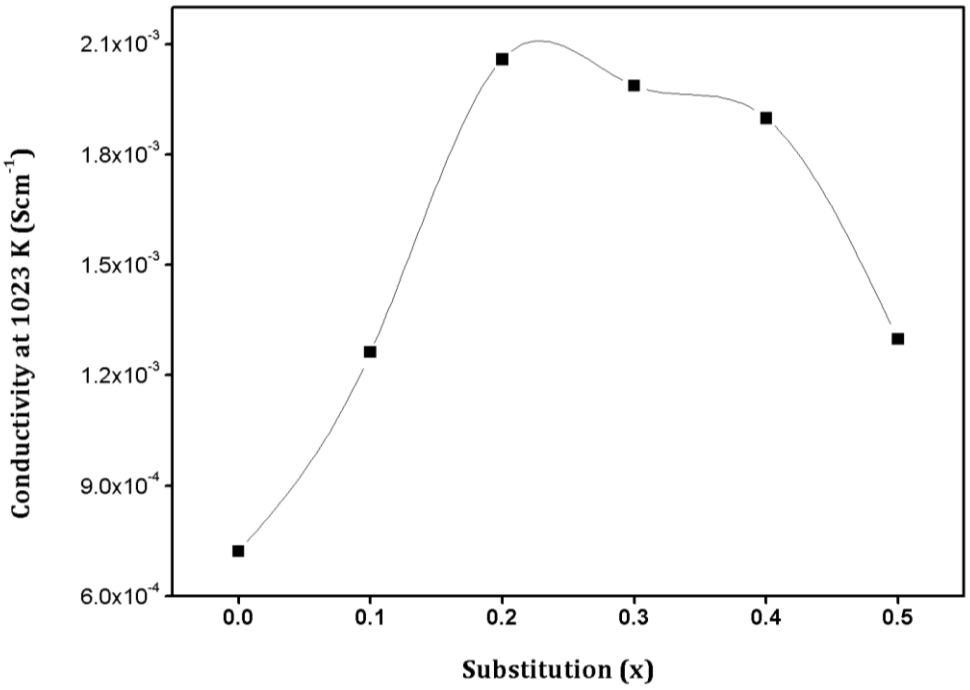

Figure 5-14: Variation of conductivity at 1013 K with substitution

It can be seen that the activation energy decreases until x = 0.2 and beyond that it increases. The conductivity is following a corresponding trend which shows a peak at x = 0.2 and then decreases. In order to understand this trend, the mechanism of electrical conduction needs to be analysed. Variation of electrical conductivity with frequency for the representative sample SSZC5 at four different temperatures is shown in Figure 5-15. The general behaviour is same at all temperatures; the conductivity remains almost the same along a plateau up to a particular frequency and after that it increases with frequency. The plateau shows frequency-independent dc conductivity in the low frequency region and the power-law increase at higher frequencies indicate a dispersion. At higher temperatures, the plateau gets modified slightly by a step, due to the effect of grain-boundary relaxations. This was also evident in the Nyquist plot of impedance.

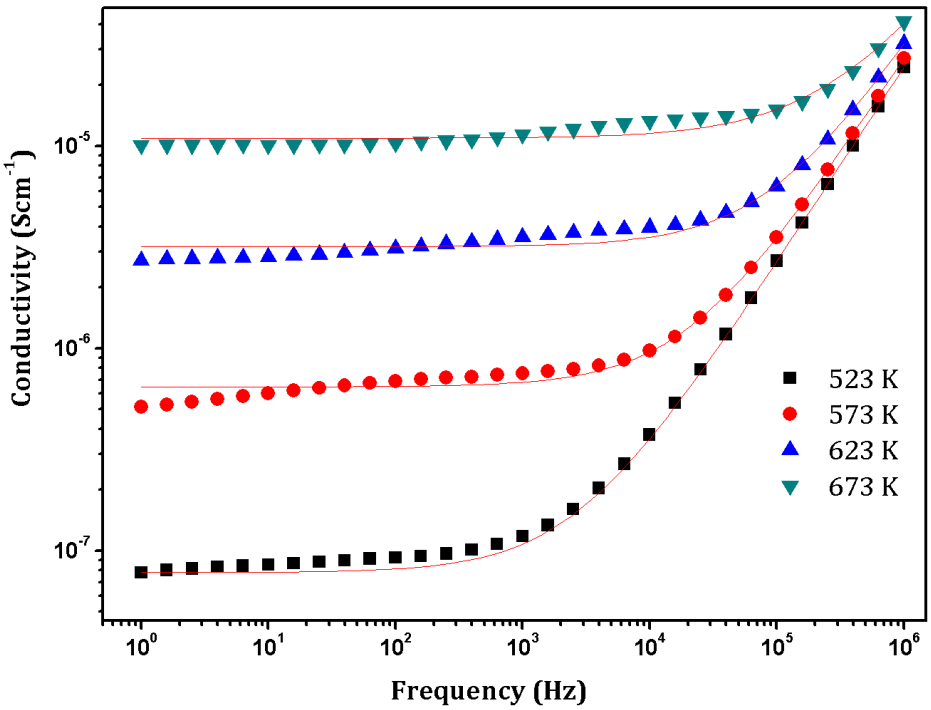

Figure 5-15: Variation of conductivity of SSZC 5 with frequency

It can be noted that the frequency at which the dispersion begins, shifts towards higher frequencies and the conductivity dispersion region shrinks. This behaviour of solid electrolytes is satisfactorily explained by the jump relaxation model put forward by Jonscher [Jonscher 1977]. At lower frequencies, an ion can jump to an adjacent vacant site, successfully contributing to dc conductivity. But at higher frequencies, a relaxation behaviour arises. The ion may jump back to its original site, or the neighbouring ions may reorient accordingly. It is this relaxation that gives rise to the conductivity dispersion at high frequencies. The frequency at which the dispersion begins is called characteristic hopping frequency. Increase in hopping frequency with increase in temperature confirms that the conduction is a thermally activated process, which was also implied by the Arrhenius plots.

Another dielectric function that is commonly used to investigate the electrical conduction process in solids is the electric modulus M^* which is the reciprocal of dielectric permittivity given by the equation,

$$M^* = j\omega C_0(Z' + jZ'') \tag{5.8}$$

such that the real part, $M' = -j\omega C_0 Z''$ and imaginary part, $M'' = -j\omega C_0 Z'$ where Z' and Z'' are the real and imaginary parts respectively of the complex impedance. The advantage of modulus formalism is that it does not receive much contribution from the electrode polarisation and hence can highlight the bulk effects. The variation of imaginary modulus (normalized by maximum, M''/M''_{max}) of various samples at 573 K is shown in Figure 5-16. It can be seen that for all samples M'' increases with frequency, reaches a peak value and then decreases. This peak indicates the presence of a relaxation behaviour, as is the case with any dielectric function. In systems like this, the modulus relaxation peak shifts towards higher frequencies with increase in measuring temperature.

It is a typical behaviour of thermally activated conduction processes [Hodge, *et al.* 1976]. In Figure 5-16 , various plots were shifted along the abscissa so that the variation of width of the relaxation peak is evident.

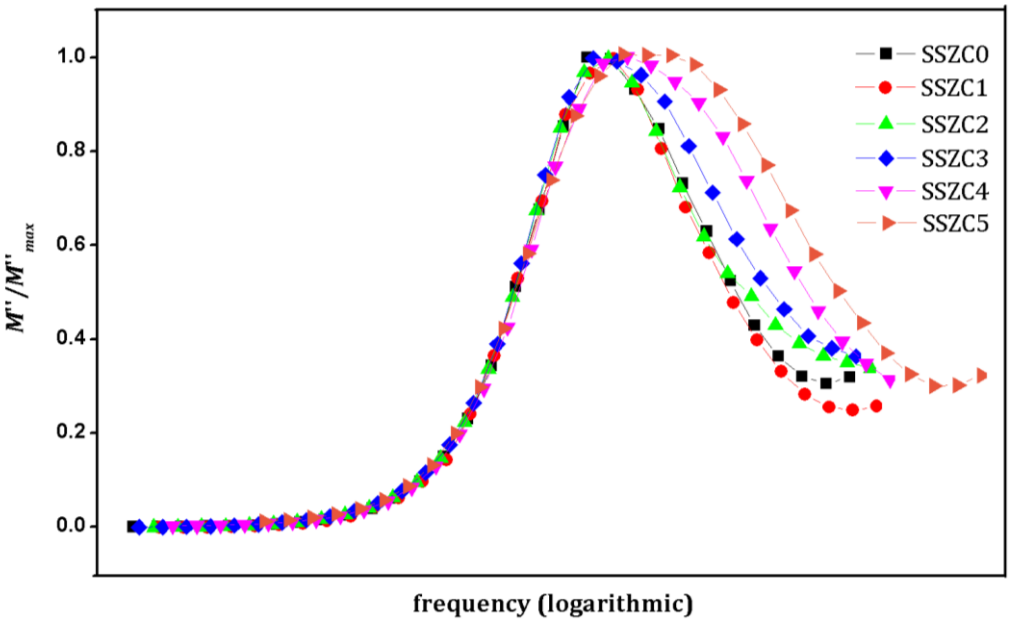

Figure 5-16: Variation in breadth of modulus relaxation peak with substitution (plots shifted along abscissa for clarity)

The ion hopping ac conductivity is related to the electric modulus as $M^*(\omega) = j\omega\epsilon_0/\sigma^*(\omega)$, which can be expressed as a Fourier transform of time derivative of the Kohlrausch function, as follows [Andrew 1999]

$$M^*(\omega) = \frac{1}{\varepsilon_\infty}\left[1 - \int_0^\infty \left(-\frac{d\emptyset}{dt}\right) e^{-j\omega t}\, dt\right] \tag{5.9}$$

where the Kohlrausch's stretched exponential function $\emptyset$ has the form,

$$\emptyset(t) = \exp\left[-\left(\frac{t}{\tau}\right)^{1-n}\right], 0 < (1-n) \leq 1 \tag{5.10}$$

Here ε_∞ is the permittivity at high frequencies and τ is the characteristic relaxation time. According to the charge coupling model of ionic conduction, [Ngai and Martin 1989, Ngai and Tsang 1999] the fractional parameter n is related to the cooperative effects among mobile ions. In a real crystal, the hopping of ions are not totally independent of each other, but can interact and correlate leading to slowing down of the relaxation rates. Increased ion-ion interactions will correspond to higher values of n which would lead to a broadening of the relaxation peak in the M'' spectra. Thus a broadened relaxation peak indicates larger cooperative behaviour among the ions and higher activation energy for the long-range ionic transport.

Results from modulus spectra, conductivity dispersion and Arrhenius plots can now be correlated to explain the trend of conductivity observed in the present system. The increase in conductivity up to x = 0.2 is driven by the reduction in activation energy caused by the disordering of the pyrochlore lattice. Beyond that the ions begin to exhibit a cooperative behaviour, leading to increase in activation energy for ionic transport reducing the conductivity. This effect can also be encouraged by the decrease in lattice volume with substitution.

5.4. Conclusion

Simultaneous substitution in $(Sm,Zr)_{2-x}(Sc,Ce)_xO_7$ and its effect on structure and electrical properties of the lattice were investigated. Powder samples were prepared by solid state reaction method. The system showed a transition from ordered pyrochlore to a defect fluorite structure with substitution, accompanied by a decrease in lattice parameter. The change in inter-ionic bonds resulted in a decrease in thermal expansion coefficient. The electrical conductivity of the samples were facilitated by thermally activated ion hopping mechanism. With increase in substitution, the conductivity increased at

first due to the lower energy barrier offered by lattice disorder. But later, decrease in lattice volume encouraged cooperative behavior among mobile ions, which turned out to be disadvantageous for conducting properties.

CHAPTER 6

****

Conclusion and Future Scope

****

This chapter summarizes all the relevant conclusions that can be drawn from various investigations carried out hitherto. A comparison of results of the present work with those in the existing literature is made. The future aspects of the investigations, including extension and improvement, are also discussed.

6.1. General conclusions

The research work presented in this thesis was an attempt to probe into the details of structure and electrical properties of a few chemical systems that are potential candidates to be used as solid oxide electrolytes for fuel cell application. Effect of cation substitution in already established rare-earth based zirconate compositions was analysed with regard to the structure and electrical property. The correlation between these two aspects was also emphasized. The major conclusions that can be drawn from the overall study are summarized as below:

- Incorporation of Ca ions in $Gd_2Zr_2O_7$ lattice through a stoichiometry of $xCaZrO_3$-$(1-x)Gd_2Zr_2O_7$ led to solid solutions that crystallized into a cubic fluorite structure.

- Despite the larger ionic radius of the substituent atom, the effect of substitution was to decrease the lattice parameter. This was attributed to the oxygen vacancies within the lattice that dominated over the effect of ionic radii difference.

- Substitution also caused an increase in thermal expansion coefficient which also implied the dominance of oxygen vacancies.

- The ionic conductivity was enhanced by the substitution due to the lower energy barriers introduced by the oxygen vacancies towards the charge transport. The thermally activated conduction process in these materials was found to follow Arrhenius behaviour and an analysis of dielectric functions was found to indicate an ionic hopping mechanism leading to long range conductivity. Presence of $CaZrO_3$ secondary phase, in the composition corresponding to $x = 0.4$, turned out to be

disadvantageous to conduction process and thus within the limit of solubility, $CaZrO_3$ enhances the electrical conductivity of $Gd_2Zr_2O_7$.

- The ionic conductivity was enhanced by the substitution due to the lower energy barrier introduced by the oxygen vacancies towards the charge transport.

- $Gd_2(Zr_{1-x}M_x)_2O_{7-\delta}$ solid solutions retained the fluorite structure of the parent lattice during the substitution by M cation (M = Sc^{3+}, Y^{3+}). Both systems showed similar extent of solid solution formation.

- Substitution by Sc^{3+} in $Gd_2Zr_2O_7$ led to a contraction of the lattice *via* lattice defects, while Y^{3+} forced the lattice to expand due to its larger ionic radius.

- Both systems had oxygen vacancies due to aliovalent substitution, but their effect was more pronounced in the Sc-substituted compositions.

- Oxygen vacancies in the expanded lattice aided in enhanced electrical properties in Y-substituted system by reducing the energy barrier for thermally activated conduction. Whereas for Sc-substituted system, cooperative behavior of ions in the contracted lattice acted in the reverse direction. Thus it could be concluded that, despite them being in the same group of *d*-block elements, the ultimate influence in physical aspects depended on the identity of the substituent ions.

- Substitution by Ce^{4+} in an ordered pyrochlore type $Sm_2Zr_2O_7$ led to the transition to a disordered defect fluorite structure in $Sm_2Zr_{2-x}Ce_xO_7$ compositions.

- Raman spectroscopic studies revealed that the disorder is happening to both cationic and anionic sublattices. The anionic disorder involved both the 48*f* and 8*b* oxygen sites.

- The substitution also led to a decrease in thermal expansion coefficient.

- The conduction process in $Sm_2Zr_{2-x}Ce_xO_7$ system is thermally activated obeying the Arrhenius equation. Increasing Ce^{4+} content increased the total conductivity of the system with lattice disorder up to the pyrochlore-fluorite phase boundary and later it decreased for completely disordered structures.

- Simultaneous substitution in $(Sm,Zr)_{2-x}(Ce,Sc)_xO_7$ also led to an order-to-disorder transition which was accompanied by a decrease in lattice parameter.

- Both substitutions caused the inter-ionic bonds to be stronger, making the lattice more rigid, which in turn resulted in a decrease in thermal expansion coefficient.

- The electrical conductivity of the samples was facilitated by thermally activated ion hopping mechanism. With increase in substitution, the conductivity increased at first due to the lower energy barrier offered by lattice disorder. But later, decrease in lattice volume encouraged cooperative behavior among mobile ions, which turned out to be disadvantageous for conducting properties.

Both the parent zirconate systems, $Gd_2Zr_2O_7$ and $Sm_2Zr_2O_7$ showed enhancement in conducting properties as solid oxide electrolytes. The highest value of conductivity obtained in the present research is 3.9×10^{-3} Scm^{-1} for

$Sm_2Zr_{1.6}Ce_{0.4}O_7$. For $CaZrO_3$-$Gd_2Zr_2O_7$ system, it was 3.5 $\times 10^{-3}$ Scm^{-1} for $x = 0.33$. Both these values are higher than the recently reported values in samarium and gadolinium zirconate systems. However, these figures are less than the conductivity of commercially used electrolytes by an order of magnitude. But considering the fact that the present measurements were made at a maximum temperature of 750 °C while the current practical electrolytes operates in temperature up to 1000 °C, and that no direct fuel cell testing was conducted, these results are promising. Also, further improvement in sintering density can lead to significant enhancement in the conductivity.

Combining the inferences from various zirconate systems as presented above, some general conclusions can be drawn. Substitution of cations can have significant influence on the structure and electrical properties of zirconate pyrochlores. However, the mechanism with which this influence is brought about depends on many other physical aspects. Generation of oxygen vacancies by aliovalent substitution can improve the conductivity due to increase in available charge carrier density. But cooperative behaviour among the charge carriers can reduce the conductivity and hence an accompanying increase in lattice volume can be helpful for easier ionic transport. Change in diatomic bond energy with substitution can influence the thermal expansion behaviour of the materials, which is also an important physical parameter to be considered for materials employed in high-temperature applications such as the fuel cells.

6.2. Future scope

The present thesis falls in the first stage of a continuing and concerted process of investigation that leads to development of efficient intermediate temperature solid oxide fuel cells. Before reaching the goal, this has to go through

some more stages of research and development due to the complexity and engineering limitations involved in the development of a practical fuel cell.

The future scope of the work includes achieving improvement in the bulk densities of the materials, which can enhance the conductivity significantly. Adopting different sintering methods, synthesis routes, using higher temperatures *etc.* can be tried for this purpose. In the present study, we had limitations achieving the best possible density due to the very high sintering temperatures warranted by pyrochlore-fluorite type zirconate materials, typically up to or above 1700 °C. The available substrates in our case cannot withstand such high temperatures and are prone to issues like sample diffusion into the substrate. Reducing the sintering temperature is also important, since in practical SOFC`s the components are sintered together to form the individual cell units. Soft chemical methods in synthesis routes may be helpful in this regard.

Electrical characterization in a larger range of temperature and frequency can give a lot more information about the conduction mechanism thereby leading to more insights on the property tuning. In the present work, the measurement temperature could go only up to 750 °C due to the limitation of silver electrodes that cannot withstand higher temperatures. With the use of platinum electrodes, the measurement temperature can go up to 1000 °C. Extension of frequency range, below 1 Hz and above 1 MHz is also desirable. It will be helpful to understand the contribution of grain, grain-boundary and electrode phenomena to the total conductivity and its variation with temperature and with change in chemical composition. Impedance measurement can also be extended to different environments like varying oxygen partial pressure, different atmospheres of nitrogen, hydrogen *etc.* This will be helpful to

understand the transference number in conduction and the chemical stability of the samples.

As these materials ultimately are to be used in a solid oxide fuel cell, the final characterization should involve the fabrication of a fuel cell unit with suitable electrode materials. Then the fuel cell performance including material-matching and voltage generation have to be analysed in a fuel cell test station. Testing should include both no-load and load conditions.

List of publications

List of publications in SCI journals

- **Vaisakhan Thampi D. S.**, Prabhakar Rao Padala, Renju U. A., "Influence of Aliovalent Cation substitution on structural and electrical properties of $Gd_2(Zr_{1-x}M_x)_2O_{7-\delta}$ (M = Sc, Y) system", *RSC Advances,* 5, 88675 – 88685 (2015)

- **Vaisakhan Thampi**, Prabhakar Rao Padala and A. N. Radhakrishnan, "Induced Oxygen vacancies and their effect on the Structural and Electrical properties of a Fluorite-type $CaZrO_3$–$Gd_2Zr_2O_7$ system" *New Journal of Chemistry*, 39, 1469–1476 (2015)

- **D. S. Vaisakhan Thampi**, P. Prabhakar Rao and A. N. Radhakrishnan, "Influence of Ce substitution on the Order-to-Disorder Structural Transition, Thermal expansion and Electrical properties in $Sm_2Zr_{2-x}Ce_xO_7$ system", *RSC Advances*, 4, 12321–12329 (2014)

- N. Radhakrishnan, P. Prabhakar Rao, S. K. Mahesh, **D. S. Vaisakhan Thampi** and Peter Koshy, "Role of Bond Strength on the Lattice Thermal Expansion and Oxide Ion Conductivity in Quaternary Pyrochlore Solid Solutions" *Inorganic Chemistry*, 51, 2409–2419 (2012)

- Linda T. Francis, P. Prabhakar Rao, Mariyam Thomas, S.K. Mahesh, V.R.Reshmi, **Vaisakhan D.S.Thampi**, "New orange-red emitting phosphor $La_3NbO_7:Eu^{3+}$ under blue excitation", *Materials Letters*, 81, 142–144 (2012)

List of Conference presentations

- **D. S. Vaisakhan Thampi** and P. Prabhakar Rao, "*Enhanced conductivity in fluorite-type $Gd_2Zr_2O_7$ lattice through doping-induced oxygen vacancies*" Presented at International Conference on Science Technology and Applications of Rare Earths (ICSTAR 15) conference held at Thiruvananthapuram on April 23-25, 2015.

- **Vaisakhan Thampi D S**, Prabhakar Rao P. and A. N. Radhakrishnan, "*Influence of $CaZrO_3$ addition on structure and electrical properties of $RE_2Zr_2O_7$ (RE: Y, Sm)*" Presented at 25th Kerala Science Congress held at Technopark, Trivandrum on January 30, 2013.

- **Vaisakhan Thampi D S**, Prabhakar Rao P. and A. N. Radhakrishnan, "*Structure and ionic conductivity studies in $CaRECeNbO_7$ system (RE: Gd, Nd, Pr, Sm, Y)*" Presented at Indian Analytical Science Congress (IASC) held at Kanyakumari on January 27-28, 2012.

- **Vaisakhan Thampi D S**, Prabhakar Rao P. and A. N. Radhakrishnan, Aswathy S. Nair, Deepika V. R., Lekshmi U, "*Oxide ionic conductors in Bi, B and Sb doped $Ce_{0.8}Gd_{0.2}O_2$ system for fuel cell applications*" Presented at Science Technology and Applications of Rare Earths conference (STAR 2011) held at Munnar on August 19-20, 2011

- Renju U A, P. Prabhakar Rao, and **Vaisakhan Thampi D S**, "*Electrical properties of $Gd_2Zr_2O_7$-$CaTiO_3$ solid solutions for fuel cell applications*" Presented at National Conference on Advanced Technologies for Materials Processing and Diagnostics (ISAS 2014) held at Kochi on September 18-24, 2014.

References

1. A. K. Baral V. S., "Ion transport and dielectric relaxation studies in nanocrystalline $Ce_{0.8}Ho_{0.2}O_{2-d}$ material" *Physica B*, 404 (**2009**) 1674.
2. Abraham F., Debreuille-Gresse M. F., Mairesse G.and Nowogrocki G., "Phase transitions and ionic conductivity in $Bi_4V_2O_{11}$ an oxide with a layered structure" *Solid State Ionics*, 28–30, Part 1 (**1988**) 529.
3. Andrew K. J., "Dielectric relaxation in solids" *Journal of Physics D: Applied Physics*, 32 (**1999**) R57.
4. Arulsamy A. D., "Renormalization group method based on the ionization energy theory" *Annals of Physics*, 326 (**2011**) 541.
5. Atkinson A., Barnett S., Gorte R. J., Irvine J. T. S., McEvoy A. J., Mogensen M., Singhal S. C.and Vohs J., "Advanced anodes for high-temperature fuel cells" *Nature Materials*, 3 (**2004**) 17.
6. Azad A. M., Larose S.and Akbar S. A., "Bismuth oxide-based solid electrolytes for fuel cells" *Journal of Materials Science*, 29 (**1994**) 4135.
7. B.P. Mandal, S.K. Deshpandeand Tyagi A. K., " Ionic conductivity enhancement in Gd2Zr2O7 pyrochlore by Nd doping" *Journal of Materials Research*, 23 (**2008**) 911.
8. Badapanda T., Sarangi S., Behera B., Anwar S., Sinha T. P., Ranjan R., Luz G. E., Jr., Longo E.and Cavalcante L. S., "Structural refinement, optical and electrical properties of $[Ba_{1-x}\ Sm_{2x/3}](Zr_{0.05}Ti_{0.95})O_3$ ceramics" *Journal of Materials Science: Materials in Electronics*, 25 (**2014**) 3427.
9. Badwal S. P. S., "Zirconia-based solid electrolytes: microstructure, stability and ionic conductivity" *Solid State Ionics*, 52 (**1992**) 23.

10. Badwal S. P. S.and Ciacchi F. T., "Oxygen-ion conducting electrolyte materials for solid oxide fuel cells" *Ionics*, 6 (**2000**) 1.

11. Badwal S. P. S.and Foger K., "Solid oxide electrolyte fuel cell review" *Ceramics International*, 22 (**1996**) 257.

12. Banerji A., Grover V., Sathe V., Deb S. K.and Tyagi A. K., "CeO_2-Gd_2O_3 system: Unraveling of microscopic features by Raman spectroscopy" *Solid State Communications*, 149 (**2009**) 1689.

13. Baral A. K.and Sankaranarayanan V., "Dielectric relaxation properties of nanostructured $Ce_{0.8}Gd_{0.1}Pr_{0.1}O_{2-\delta}$ material at intermediate temperatures" *Applied Physics Letters*, 94 (**2009**) 074101.

14. Battle P. D., Catlow C. R. A., Heap J. W.and Moroney L. M., "Structural and dynamical studies of δ-Bi_2O_3 oxide ion conductors: I. The structure of $(Bi_2O_3)_{1-x}(Y_2O_3)_x$ as a function of x and temperature" *Journal of Solid State Chemistry*, 63 (**1986**) 8.

15. Brandon N. P.and Brett D. J., "Engineering porous materials for fuel cell applications" *Philosophical Transactions of the Royal Society of London A: Mathematical, Physical and Engineering Sciences*, 364 (**2006**) 147.

16. Brett D. J. L., Atkinson A., Brandon N. P.and Skinner S. J., "Intermediate temperature solid oxide fuel cells" *Chemical Society Reviews*, 37 (**2008**) 1568.

17. Brik M. G.and Srivastava A. M., "Pyrochlore Structural Chemistry: Predicting the Lattice Constant by the Ionic Radii and Electronegativities of the Constituting Ions" *Journal of the American Ceramic Society*, 95 (**2012**) 1454.

18. Bućko M. M., "Some structural aspects of ionic conductivity in zirconia stabilised by yttria and calcia " *Materials Science-Poland*, 24 (**2006**) 39.

19. Burggraaf A. J., van Dijk T.and Verkerk M. J., "Structure and conductivity of pyrochlore and fluorite type solid solutions" *Solid State Ionics*, 5 (**1981**) 519.

20. Cai L., Arias A. L.and Nino J. C., "The tolerance factors of the pyrochlore crystal structure" *Journal of Materials Chemistry*, 21 (**2011**) 3611.

21. Carrette L., Friedrich K. A.and Stimming U., "Fuel Cells – Fundamentals and Applications" *Fuel Cells*, 1 (**2001**) 5.

22. Chakoumakos B. C., "Systematics of the pyrochlore structure type, ideal $A_2B_2X_6Y$" *Journal of Solid State Chemistry*, 53 (**1984**) 120.

23. Chatzichristodoulou C., Norby P., Hendriksen P.and Mogensen M., "Size of oxide vacancies in fluorite and perovskite structured oxides" *Journal of Electroceramics*, 34 (**2015**) 100.

24. Chen J., Lian J., Wang L. M., Ewing R. C., Wang R. G.and Pan W., "X-ray Photoelectron Spectroscopy Study of Disordering in $Gd_2(Ti_{1-x}Zr_x)_2O_7$ Pyrochlores" *Physical Review Letters*, 88 (**2002**) 105901.

25. Chiba R., Ishii T.and Yoshimura F., "Temperature dependence of ionic conductivity in *(1-x)*ZrO_2-*(x-y)*Sc_2O_3-$_y$$Yb_2O_3$ electrolyte material" *Solid State Ionics*, 91 (**1996**) 249.

26. Dalslet B., Blennow P., Hendriksen P., Bonanos N., Lybye D.and Mogensen M., "Assessment of doped ceria as electrolyte" *Journal of Solid State Electrochemistry*, 10 (**2006**) 547.

27. David A. Andersson S. I. S., Natalia V. Skorodumova, Igor A. Abrikosov, and Börje Johansson "Optimization of ionic conductivity in doped ceria "

Proceedings of The National Academy of Sciences of the USA, 103 (**2006**) 3518.

28. de los Reyes M., Whittle K. R., Zhang Z., Ashbrook S. E., Mitchell M. R., Jang L.-Y.and Lumpkin G. R., "The pyrochlore to defect fluorite phase transition in $Y_2Sn_{2-x}Zr_xO_7$" *RSC Advances*, 3 (**2013**) 5090.

29. Degen T., Sadki M., Bron E., König U.and Nénert G., "The HighScore suite" *Powder Diffraction*, 29 (**2014**) S13.

30. Díaz-Guillén J. A., Fuentes A. F., Díaz-Guillén M. R., Almanza J. M., Santamaría J.and León C., "The effect of homovalent A-site substitutions on the ionic conductivity of pyrochlore-type $Gd_2Zr_2O_7$" *Journal of Power Sources*, 186 (**2009**) 349.

31. Dickson F. J., Hawkins K. D.and White T. J., "Calcium uranium titanate—A new pyrochlore" *Journal of Solid State Chemistry*, 82 (**1989**) 146.

32. Djurado E.and Labeau M., "Second phases in doped lanthanum gallate perovskites" *Journal of the European Ceramic Society*, 18 (**1998**) 1397.

33. Enoki M., Yan J., Matsumoto H.and Ishihara T., "High oxide ion conductivity in Fe and Mg doped $LaGaO_3$ as the electrolyte of solid oxide fuel cells" *Solid State Ionics*, 177 (**2006**) 2053.

34. Ewing R. C., Weber W. J.and Lian J., "Nuclear waste disposal---pyrochlore $A_2B_2O_7$: Nuclear waste form for the immobilization of plutonium and ``minor'' actinides" *Journal of Applied Physics*, 95 (**2004**) 5949.

35. Fergus J. W., "Doping and defect association in oxides for use in oxygen sensors" *Journal of Materials Science*, 38 (**2003**) 4259.

36. Fergus J. W., "Electrolytes for solid oxide fuel cells" *Journal of Power Sources*, 162 (**2006**) 30.

37. Figueiredo F. M. L.and Marques F. M. B., "Electrolytes for solid oxide fuel cells" *Wiley Interdisciplinary Reviews: Energy and Environment*, 2 (**2013**) 52.

38. Funke K., "Ion transport in fast ion conductors — spectra and models" *Solid State Ionics*, 94 (**1997**) 27.

39. García-Barriocanal J., Moreno K. J., Mendoza-Suárez G., Fuentes A. F., Santamaría J.and León C., "Effects of cooperativity on ion dynamics in oxygen conducting $Gd_2Ti_{2-y}Zr_yO_7$" *Journal of Non-Crystalline Solids*, 351 (**2005**) 2813.

40. Garcia-Barriocanal J., Rivera-Calzada A., Varela M., Sefrioui Z., Díaz-Guillén M. R., Moreno K. J., Díaz-Guillén J. A., Iborra E., Fuentes A. F., Pennycook S. J., Leon C.and Santamaria J., "Tailoring Disorder and Dimensionality: Strategies for Improved Solid Oxide Fuel Cell Electrolytes" *ChemPhysChem*, 10 (**2009**) 1003.

41. Georges S., Goutenoire F., Altorfer F., Sheptyakov D., Fauth F., Suard E.and Lacorre P., "Thermal, structural and transport properties of the fast oxide-ion conductors $La_{2-x}R_xMo_2O_9$ (R=Nd, Gd, Y)" *Solid State Ionics*, 161 (**2003**) 231.

42. Gerhardt R., "Impedance and dielectric spectroscopy revisted: Distinguishing localized relaxation from long-range conductivity" *Journal of Physics and Chemistry of Solids*, 55 (**1994**) 1491.

43. Glerup M., Nielsen O. F.and Poulsen F. W., "The Structural Transformation from the Pyrochlore Structure, $A_2B_2O_7$, to the Fluorite Structure, AO_2, Studied by Raman Spectroscopy and Defect Chemistry Modeling" *Journal of Solid State Chemistry*, 160 (**2001**) 25.

44. Gödickemeier M.and Gauckler L. J., "Engineering of Solid Oxide Fuel Cells with Ceria-Based Electrolytes" *Journal of The Electrochemical Society*, 145 (**1998**) 414.

45. Goodenough J. B., Ruiz-Diaz J. E.and Zhen Y. S., "Oxide-ion conduction in $Ba_2In_2O_5$ and $Ba_3In_2MO_8$ (M=Ce, Hf, or Zr)" *Solid State Ionics*, 44 (**1990**) 21.

46. Goutenoire F., Retoux R., Suard E.and Lacorre P., "Ab InitioDetermination of the Novel Perovskite-Related Structure of $La_7Mo_7O_{30}$ from Powder Diffraction" *Journal of Solid State Chemistry*, 142 (**1999**) 228.

47. Guo X., "Defect Structure Modification in Zirconia by Alumina" *physica status solidi (a)*, 183 (**2001**) 261.

48. Gupta H. C.and Brown S., "An analytical expression for Eg and Ag modes of pyrochlores" *Journal of Physics and Chemistry of Solids*, 64 (**2003**) 2205.

49. Hari Prasad D., Park S. Y., Ji H., Kim H. R., Son J. W., Kim B. K., Lee H. W.and Lee J. H., "Cobalt oxide co-doping effect on the sinterability and electrical conductivity of nano-crystalline Gd-doped ceria" *Ceramics International*, 38, Supplement 1 (**2012**) S497.

50. Hartmann T., Alaniz A., Poineau F., Weck P. F., Valdez J. A., Tang M., Jarvinen G. D., Czerwinski K. R.and Sickafus K. E., "Structure studies on lanthanide technetium pyrochlores as prospective host phases to immobilize technetium and fission lanthanides from effluents of reprocessed used nuclear fuels" *Journal of Nuclear Materials*, 411 (**2011**) 60.

51. HartmanovÁ M., Lomonova E. E., NavrÁTil V., ŠUtta P.and Kundracik F., "Characterization of yttria-doped ceria prepared by directional crystallization" *Journal of Materials Science*, 40 (**2005**) 5679.

52. Hayashi H., Inaba H., Matsuyama M., Lan N. G., Dokiya M.and Tagawa H., "Structural consideration on the ionic conductivity of perovskite-type oxides" *Solid State Ionics*, 122 (**1999**) 1.

53. Hayashi H., Suzuki M.and Inaba H., "Thermal expansion of Sr- and Mg-doped $LaGaO_3$" *Solid State Ionics*, 128 (**2000**) 131.

54. Heremans C., Wuensch B. J., Stalick J. K.and Prince E., "Fast-Ion Conducting $Y_2(Zr_yTi_{1-y})_2O_7$ Pyrochlores: Neutron Rietveld Analysis of Disorder Induced by Zr Substitution" *Journal of Solid State Chemistry*, 117 (**1995**) 108.

55. Hess N. J., Begg B. D., Conradson S. D., McCready D. E., Gassman P. L.and Weber W. J., "Spectroscopic Investigations of the Structural Phase Transition in $Gd_2(Ti_{1-y}Zr_y)_2O_7$ Pyrochlores" *The Journal of Physical Chemistry B*, 106 (**2002**) 4663.

56. Hodge I. M., Ingram M. D.and West A. R., "Impedance and modulus spectroscopy of polycrystalline solid electrolytes" *Journal of Electroanalytical Chemistry and Interfacial Electrochemistry*, 74 (**1976**) 125.

57. Hong S. J., Mehta K.and Virkar A. V., "Effect of Microstructure and Composition on Ionic Conductivity of Rare-Earth Oxide-Doped Ceria" *Journal of The Electrochemical Society*, 145 (**1998**) 638.

58. Huggins R. A., "Simple method to determine electronic and ionic components of the conductivity in mixed conductors a review" *Ionics*, 8 (**2002**) 300.

59. IEA, "Deploying Renewables 2011: Best and Future Policy Practice" Organisation for Economic Co-operation and Development/International Energy Agency, (**2011**).

60. Inaba H.and Tagawa H., "Ceria-based solid electrolytes" *Solid State Ionics*, 83 (**1996**) 1.

61. Inagaki T., Nishiwaki F., Kanou J., Yamasaki S., Hosoi K., Miyazawa T., Yamada M.and Komada N., "Demonstration of high efficiency intermediate-temperature solid oxide fuel cell based on lanthanum gallate electrolyte" *Journal of Alloys and Compounds*, 408–412 (**2006**) 512.

62. Ishihara T., Ishikawa S., Ando M., Nishiguchi H.and Takita Y., "PO2 dependence of valence number of Co in $LaGaO_3$ and its influence on partial electronic and oxide ionic conductivity" *Solid State Ionics*, 173 (**2004**) 9.

63. Ishihara T., Matsuda H., Azmi bin Bustam M.and Takita Y., "Oxide ion conductivity in doped Ga based perovskite type oxide" *Solid State Ionics*, 86–88, Part 1 (**1996**) 197.

64. Ishihara T., Matsuda H.and Takita Y., "Doped $LaGaO_3$ Perovskite Type Oxide as a New Oxide Ionic Conductor" *Journal of the American Chemical Society*, 116 (**1994**) 3801.

65. Ishihara T., Matsuda H.and Takita Y., "Effects of rare earth cations doped for La site on the oxide ionic conductivity of $LaGaO_3$-based perovskite type oxide" *Solid State Ionics*, 79 (**1995**) 147.

66. J. W. Stevenson, K. Hasinska, N. L. Canfieldand Armstrong T. R., "Influence of Cobalt and Iron Additions on the Electrical and Thermal Properties of $(La,Sr)(Ga,Mg)O_{3-\delta}$ " *Journal of Electrochemical Society*, 147 (**2000**) 3213.

67. Jacobson A. J., "Materials for Solid Oxide Fuel Cells" *Chemistry of Materials*, 22 (**2010**) 660.

68. Jia-Hu Ouyang, Cheng Zhu, Zhan-Guo Liu, Zhe Renand Jing L., "Influence of Sm3+ doping on microstructure and electrical properties of $((Nd_{0.7}Yb_{0.3})_{1-x}Sm_x)_2Zr_2O_7$" *Functional Materials Letters*, 08 (**2015**) 1540012.

69. Jiang S.and Chan S., "A review of anode materials development in solid oxide fuel cells" *Journal of Materials Science*, 39 (**2004**) 4405.

70. Jonscher A. K., "The 'universal' dielectric response" *Nature*, 267 (**1977**) 673.

71. Joshi A., Steppan J., Taylor D.and Elangovan S., "Solid Electrolyte Materials, Devices, and Applications" *Journal of Electroceramics*, 13 (**2004**) 619.

72. Juhl M., Primdahl S., Manon C.and Mogensen M., "Performance/structure correlation for composite SOFC cathodes" *Journal of Power Sources*, 61 (**1996**) 173.

73. Kendall K. R., Navas C., Thomas J. K.and Loye H. C. z., "Recent developments in perovskite-based oxide ion conductors" *Solid State Ionics*, 82 (**1995**) 215.

74. Kendrick E., Islam M. S.and Slater P. R., "Developing apatites for solid oxide fuel cells: insight into structural, transport and doping properties" *Journal of Materials Chemistry*, 17 (**2007**) 3104.

75. Kendrick E., Kendrick J., Knight K. S., Islam M. S.and Slater P. R., "Cooperative mechanisms of fast-ion conduction in gallium-based oxides with tetrahedral moieties" *Nature Materials*, 6 (**2007**) 871.

76. Kendrick E.and Slater P. R., "Synthesis of hexagonal lanthanum germanate apatites through site selective isovalent doping with yttrium" *Materials Research Bulletin*, 43 (**2008**) 2509.

77. Kharton V., Tsipis E., Yaremchenko A., Vyshatko N., Shaula A., Naumovich E.and Frade J., "Oxygen ionic and electronic transport in $Gd_{2-x}Ca_xTi_2O_{7-\delta}$ pyrochlores" *Journal of Solid State Electrochemistry*, 7 (**2003**) 468.

78. Kharton V. V., Marques F. M. B.and Atkinson A., "Transport properties of solid oxide electrolyte ceramics: a brief review" *Solid State Ionics*, 174 (**2004**) 135.

79. Kilner J. A., "Fast oxygen transport in acceptor doped oxides" *Solid State Ionics*, 129 (**2000**) 13.

80. Kim C., Mehta A., Feng D. L., Shen K. M., Armitage N. P., Char K., Moon S. H., Xie Y. Y.and Wu J., "X-ray diffraction measurements of the c -axis Debye-Waller factors of $YBa_2Cu_3O_7$ and $HgBa_2CaCu_2O_6$" *Physical Review B*, 67 (**2003**) 092508.

81. Kotobukia M., Munakata H., Kanamura K., Sato Y.and Yoshida T., "Compatibility of $Li_7La_3Zr_2O_{12}$ Solid Electrolyte to All-Solid-State Battery Using Li Metal Anode" *Journal of Electrochemical Society*, 157 (**2010**) A1076.

82. Kuang X., Green M. A., Niu H., Zajdel P., Dickinson C., Claridge J. B., Jantsky L.and Rosseinsky M. J., "Interstitial oxide ion conductivity in the layered tetrahedral network melilite structure" *Nature Materials*, 7 (**2008**) 498.

83. Kuharuangrong S., "Ionic conductivity of Sm, Gd, Dy and Er-doped ceria" *Journal of Power Sources*, 171 (**2007**) 506.

84. Kumar Baral A.and Sankaranarayanan V., "Electrical study and dielectric relaxation behavior in nanocrystalline $Ce_{0.85}Gd_{0.15}O_{2-\delta}$ material at intermediate temperatures" *Applied Physics. A*, 98 (**2010**) 367.

85. Kumar M., Kulandainathan M. A., Raj I. A., Chandrasekaran R.and Pattabiraman R., "Electrical and sintering behaviour of $Y_2Zr_2O_7$ (YZ) pyrochlore-based materials—the influence of bismuth" *Materials Chemistry and Physics*, 92 (**2005**) 295.

86. Kumar P. P.and Yashonath S., "Ionic conduction in the solid state" *J Chem Sci*, 118 (**2006**) 135.

87. Kutty K. V. G., Mathews C. K., Rao T. N.and Varadaraju U. V., "Oxide ion conductivity in some substituted rare earth pyrozirconates" *Solid State Ionics*, 80 (**1995**) 99.

88. Kutty K. V. G., Rajagopalan S., Mathews C. K.and Varadaraju U. V., "Thermal expansion behaviour of some rare earth oxide pyrochlores" *Materials Research Bulletin*, 29 (**1994**) 759.

89. Lacorre P., Goutenoire F., Bohnke O., Retoux R.and Laligant Y., "Designing fast oxide-ion conductors based on $La_2Mo_2O_9$" *Nature*, 404 (**2000**) 856.

90. Lang M., Zhang F., Zhang J., Wang J., Lian J., Weber W. J., Schuster B., Trautmann C., Neumann R.and Ewing R. C., "Review of $A_2B_2O_7$ pyrochlore response to irradiation and pressure" *Nuclear Instruments and Methods in Physics Research Section B: Beam Interactions with Materials and Atoms*, 268 (**2010**) 2951.

91. Lee J. H., Yoon S. M., Kim B. K., Kim J., Lee H. W.and Song H. S., "Electrical conductivity and defect structure of yttria-doped ceria-stabilized zirconia" *Solid State Ionics*, 144 (**2001**) 175.

92. Lee Y. H., Sheu H. S., Deng J. P.and Kao H. C. I., "Preparation and fluorite–pyrochlore phase transformation in $Gd_2Zr_2O_7$" *Journal of Alloys and Compounds*, 487 (**2009**) 595.

93. Leon-Reina L., Losilla E. R., Martinez-Lara M., Bruque S.and Aranda M. A. G., "Interstitial oxygen conduction in lanthanum oxy-apatite electrolytes" *Journal of Materials Chemistry*, 14 (**2004**) 1142.

94. Li L., Chen F., Lu J.-Q.and Luo M.-F., "Study of Defect Sites in $Ce_{1-x}M_xO_{2-\delta}$ (x = 0.2) Solid Solutions Using Raman Spectroscopy" *The Journal of Physical Chemistry A*, 115 (**2011**) 7972.

95. Lian J., Wang L., Chen J., Sun K., Ewing R. C., Matt Farmer J.and Boatner L. A., "The order–disorder transition in ion-irradiated pyrochlore" *Acta Materialia*, 51 (**2003**) 1493.

96. Lide D. R., "CRC Handbook of Chemistry and Physics: A Ready-Reference Book of Chemical and Physical Data" (**1994**).

97. Lion S. S.and Worrell W. L., "Electrical properties of novel mixed-conducting oxides" *Applied Physics A*, 49 (**1989**) 25.

98. Liu Z.-G., Gao S., Ouyang J.-H.and Xia X.-L., "Influence of MoO_3 doping on structure and electrical conductivity of defect fluorite-type $Gd_2Zr_2O_7$" *Journal of Alloys and Compounds*, 506 (**2010**) 868.

99. Liu Z.-G., Ouyang J.-H., Sun K.-N.and Xia X.-L., "Effect of Gd and Yb co-doping on structure and electrical conductivity of the $Sm_2Zr_2O_7$ pyrochlore" *Journal of Power Sources*, 195 (**2010**) 7225.

100. Liu Z.-G., Ouyang J.-H., Sun K.-N.and Zhou Y., "Effect of CaO addition on the structure and electrical conductivity of the pyrochlore-type $GdSmZr_2O_7$" *Ceramics International*, 38 (**2012**) 2935.

101. Liu Z.-G., Ouyang J.-H., Sun K.-N.and Zhou Y., "Electrical properties of the $GdSmZr_2O_7$ ceramic under different sintering conditions" *Journal of Power Sources*, 210 (**2012**) 96.

102. Liu Z.-G., Ouyang J.-H., Zhou Y.and Xia X.-L., "Effect of Sm substitution for Gd on the electrical conductivity of fluorite-type $Gd_2Zr_2O_7$" *Journal of Power Sources*, 185 (**2008**) 876.

103. Liu Z.-G., Ouyang J.-H., Zhou Y.and Xia X.-L., "Effect of Ti substitution for Zr on the thermal expansion property of fluorite-type $Gd_2Zr_2O_7$" *Materials & Design*, 30 (**2009**) 3784.

104. Liu Z.-G., Ouyang J.-H., Zhou Y., Xiang J.and Liu X.-M., "Preparation, structure and electrical conductivity of pyrochlore-type samarium–lanthanum zirconate ceramics" *Materials & Design*, 32 (**2011**) 4201.

105. Liu Z. G., Ouyang J. H.and Sun K. N., "Improvement of Electrical Conductivity of Trivalent Rare-earth Cation-doped Neodymium Zirconate by Co-doping Gadolinium and Ytterbium" *Fuel Cells*, 10 (**2010**) 1050.

106. M. A. Subramanian G. A. a. G. V. S. R., "Oxide Pyrochlores - A Review" *Progress in Solid State Chemistry*, 15 (**1983**) 55.

107. Mandal B. P., Banerji A., Sathe V., Deb S. K.and Tyagi A. K., "Order–disorder transition in $Nd_{2-y}Gd_yZr_2O_7$ pyrochlore solid solution: An X-ray diffraction and Raman spectroscopic study" *Journal of Solid State Chemistry*, 180 (**2007**) 2643.

108. Mandal B. P., Krishna P. S. R.and Tyagi A. K., "Order–disorder transition in the $Nd_{2-y}Y_yZr_2O_7$ system: Probed by X-ray diffraction and Raman spectroscopy" *Journal of Solid State Chemistry*, 183 (**2010**) 41.

109. Marrero-López D., Martín-Sedeño M. C., Peña-Martínez J., Ruiz-Morales J. C., Núñez P., Aranda M. A. G.and Ramos-Barrado J. R., "Evaluation of apatite silicates as solid oxide fuel cell electrolytes" *Journal of Power Sources*, 195 (**2010**) 2496.

110. Marrocchelli D., Bishop S. R.and Kilner J., "Chemical expansion and its dependence on the host cation radius" *Journal of Materials Chemistry A*, 1 (**2013**) 7673.

111. Masashi Mori, Yoshiko Hiei, Nigel M. Sammesand Tompsett G. A., "Thermal Expansion Behaviors and Mechanisms for Ca- or Sr-Doped Lanthanum Manganite Perovskites under Oxidizing Atmospheres" *Journal of Electrochemical Society*, 147 (**2000**) 1295.

112. Massimiliano Lo Faro D. L. R., Vincenzo Antonucci and Antonino Salvatore Aric, "Intermediate temperature solid oxide fuel cell electrolytes" *Journal of the Indian Institute of Science*, 89 (**2009**) 363.

113. McBride J. R., Hass K. C., Poindexter B. D.and Weber W. H., "Raman and x-ray studies of $Ce_{1-x}RE_xO_{2-y}$, where RE = La, Pr, Nd, Eu, Gd, and Tb" *Journal of Applied Physics*, 76 (**1994**) 2435.

114. McCauley R. A., "Structural characteristics of pyrochlore formation " *Journal of Applied Physics*, 51 (**1980**) 290.

115. Pyrochlore Group: Pyrochlore Group mineral information and data, Mineralogy H. I. o., http://www.mindat.org/min-3316.html.

116. Minervini L., Grimes R. W.and Sickafus K. E., "Disorder in Pyrochlore Oxides" *Journal of the American Ceramic Society*, 83 (**2000**) 1873.

117. Minh N. Q., "Ceramic Fuel Cells" *Journal of the American Ceramic Society*, 76 (**1993**) 563.

118. Mogensen M., Lybye D., Bonanos N., Hendriksen P. V.and Poulsen F. W., "Factors controlling the oxide ion conductivity of fluorite and perovskite structured oxides" *Solid State Ionics*, 174 (**2004**) 279.

119. Mogensen M., Sammes N. M.and Tompsett G. A., "Physical, chemical and electrochemical properties of pure and doped ceria" *Solid State Ionics*, 129 (**2000**) 63.

120. Mohanlal S. K., "An experimental determination of the Debye-Waller factor for iron by neutron diffraction" *Journal of Physics C: Solid State Physics*, 12 (**1979**) L651.

121. Moon P. K.and Tuller H. L., "Ionic conduction in the $Gd_2Ti_2O_7$–$Gd_2Zr_2O_7$ system" *Solid State Ionics*, 28–30, Part 1 (**1988**) 470.

122. Moreno K. J., Guevara-Liceaga M. A., Fuentes A. F., García-Barriocanal J., León C.and Santamaría J., "Room-temperature synthesis and conductivity of the pyrochlore type $Dy_2(Ti_{1-y}Zr_y)_2O_7$ ($0 \leqslant y \leqslant 1$) solid solution" *Journal of Solid State Chemistry*, 179 (**2006**) 928.

123. Moreno; K., Mendoza-Suárez; G., Fuentes; A., García-Barriocanal; J.and Santamaria C. L. J., "Cooperative oxygen ion dynamics in $Gd_2Ti_{2-y}Zr_yO_7$" *Physical Review B*, 71 (**2005**) 132301.

124. Mori M., Abe T., Itoh H., Yamamoto O., Takeda Y.and Kawahara T., "Cubic-stabilized zirconia and alumina composites as electrolytes in planar type solid oxide fuel cells" *Solid State Ionics*, 74 (**1994**) 157.

125. Mori M., Suda E., Pacaud B., Murai K.and Moriga T., "Effect of components in electrodes on sintering characteristics of $Ce_{0.9}Gd_{0.1}O_{1.95}$ electrolyte in intermediate-temperature solid oxide fuel cells during fabrication" *Journal of Power Sources*, 157 (**2006**) 688.

126. Moriga T., Emura S., Yoshiasa A., Kikkawa S., Kanamaru F.and Koto K., "X-ray and Raman study on coordination states of fluorite- and pyrochlore-type compounds in the system ZrO_2-Gd_2O_3" *Solid State Ionics*, 40–41, Part 1 (**1990**) 357.

127. Mouta R., Silva R. X.and Paschoal C. W. A., "Tolerance factor for pyrochlores and related structures" *Acta Crystallographica Section B*, 69 (**2013**) 439.

128. Nakayama S., Aono H.and Sadaoka Y., "Ionic Conductivity of $Ln_{10}(SiO_4)_6O_3$ (Ln = La, Nd, Sm, Gd and Dy)" *Chemistry Letters*, 24 (**1995**) 431.

129. Nakayama S., Kageyama T., Aono H.and Sadaoka Y., "Ionic conductivity of lanthanoid silicates, $Ln_{10}(SiO_4)_6O_3$ (Ln = La, Nd, Sm, Gd, Dy, Y, Ho, Er and Yb)" *Journal of Materials Chemistry*, 5 (**1995**) 1801.

130. Ngai K. L.and Martin S. W., "Correlation between the activation enthalpy and Kohlrausch exponent for ionic conductivity in oxide glasses" *Physical Review B*, 40 (**1989**) 10550.

131. Ngai K. L.and Tsang K. Y., "Similarity of relaxation in supercooled liquids and interacting arrays of oscillators" *Physical Review E*, 60 (**1999**) 4511.

132. Nomura K., Mizutani Y., Kawai M., Nakamura Y.and Yamamoto O., "Aging and Raman scattering study of scandia and yttria doped zirconia" *Solid State Ionics*, 132 (**2000**) 235.

133. Nomura K.and Tanase S., "Electrical conduction behavior in $(La_{0.9}Sr_{0.1})M^{III}O_{3-\delta}$ (M^{III}=Al, Ga, Sc, In, and Lu) perovskites" *Solid State Ionics*, 98 (**1997**) 229.

134. Ormerod R. M., "Solid oxide fuel cells" *Chemical Society Reviews*, 32 (**2003**) 17.

135. Padmasree K. P., Kanchan D. K.and Kulkarni A. R., "Impedance and Modulus studies of the solid electrolyte system $20CdI_2–80[xAg_2O–y(0.7V_2O_5–0.3B_2O_3)]$, where $1 \leq x/y \leq 3$" *Solid State Ionics*, 177 (**2006**) 475.

136. Panhans M. A.and Blumenthal R. N., "A thermodynamic and electrical conductivity study of nonstoichiometric cerium dioxide" *Solid State Ionics*, 60 (**1993**) 279.

137. Pikalova E. Y., Murashkina A. A., Maragou V. I., Demin A. K., Strekalovsky V. N.and Tsiakaras P. E., "CeO_2 based materials doped with lanthanides for applications in intermediate temperature electrochemical devices" *International Journal of Hydrogen Energy*, 36 (**2011**) 6175.

138. Pirzada M., Grimes R. W., Minervini L., Maguire J. F.and Sickafus K. E., "Oxygen migration in $A_2B_2O_7$ pyrochlores" *Solid State Ionics*, 140 (**2001**) 201.

139. Porat O., Heremans C.and Tuller H. L., "Stability and mixed ionic electronic conduction in $Gd_2(Ti_{1-x}Mo_x)_2O_7$ under anodic conditions" *Solid State Ionics*, 94 (**1997**) 75.

140. Poulsen F. W., Glerup M.and Holtappels P., "Structure, Raman spectra and defect chemistry modelling of conductive pyrochlore oxides" *Solid State Ionics*, 135 (**2000**) 595.

141. Pramana S. S., Klooster W. T.and White T. J., "Framework `interstitial' oxygen in $La_{10}(GeO_4)_5(GeO_5)O_2$ apatite electrolyte" *Acta Crystallographica Section B*, 63 (**2007**) 597.

142. Qu Z., Wan C.and Pan W., "Thermal Expansion and Defect Chemistry of MgO-Doped $Sm_2Zr_2O_7$" *Chemistry of Materials*, 19 (**2007**) 4913.

143. Radhakrishnan A. N., Rao P. P., Linsa K. S. M., Deepa M.and Koshy P., "Influence of disorder-to-order transition on lattice thermal expansion and oxide ion conductivity in (CaxGd1-x)2(Zr1-xMx)2O7 pyrochlore solid solutions" *Dalton Transactions*, 40 (**2011**)

144. Radhakrishnan A. N., Rao P. P., Linsa K. S. M., Deepa M.and Koshy P., "Influence of disorder-to-order transition on lattice thermal expansion and oxide ion conductivity in $(Ca_xGd_{1-x})_2(Zr_{1-x}M_x)_2O_7$ pyrochlore solid solutions" *Dalton Transactions*, 40 (**2011**) 3839.

145. Ralph J. M., Schoeler A. C.and Krumpelt M., "Materials for lower temperature solid oxide fuel cells" *Journal of Materials Science*, 36 (**2001**) 1161.

146. Rangasamy E., Wolfenstine J.and Sakamoto J., "The role of Al and Li concentration on the formation of cubic garnet solid electrolyte of nominal composition $Li_7La_3Zr_2O_{12}$" *Solid State Ionics*, 206 (**2012**) 28.

147. Réau J. M., Rossignol S., Tanguy B., Rojo J. M., Herrero P., Rojas R. M.and Sanz J., "Conductivity relaxation parameters of some Ag+ conducting tellurite glasses containing AgI or the $(AgI)_{0.75}$ $(T1I)_{0.25}$ eutectic mixture" *Solid State Ionics*, 74 (**1994**) 65.

148. Reddy K.and Karan K., "Sinterability, Mechanical, Microstructural, and Electrical Properties of Gadolinium-Doped Ceria Electrolyte for Low-Temperature Solid Oxide Fuel Cells" *Journal of Electroceramics*, 15 (**2005**) 45.

149. Reis S. L., Souza E. C. C.and Muccillo E. N. S., "Solid solution formation, densification and ionic conductivity of Gd- and Sm-doped ceria" *Solid State Ionics*, 192 (**2011**) 172.

150. Reynolds E., Blanchard P. E. R., Kennedy B. J., Ling C. D., Liu S., Avdeev M., Zhang Z., Cuello G. J., Tadich A.and Jang L.-Y., "Anion Disorder in Lanthanoid Zirconates $Gd_{2-x}Tb_xZr_2O_7$" *Inorganic Chemistry*, 52 (**2013**) 8409.

151. Sameshima S., Hirata Y.and Ehira Y., "Structural change in Sm- and Nd-doped ceria under a low oxygen partial pressure" *Journal of Alloys and Compounds*, 408–412 (**2006**) 628.

152. Sarat S., Sammes N.and Smirnova A., "Bismuth oxide doped scandia-stabilized zirconia electrolyte for the intermediate temperature solid oxide fuel cells" *Journal of Power Sources*, 160 (**2006**) 892.

153. Sarkar P.and Nicholson P. S., "Electric Relaxation Studies of Defects and Defect Associates in Dilute Ceria-Lanthanum Oxide Solid Solutions" *Journal of American Ceramic Society*, 72 (**1989**) 1447.

154. Sayed F. N., Grover V., Bhattacharyya K., Jain D., Arya A., Pillai C. G. S.and Tyagi A. K., "$Sm_{2-x}Dy_xZr_2O_7$ Pyrochlores: Probing Order−Disorder Dynamics and Multifunctionality" *Inorganic Chemistry*, 50 (**2011**) 2354.

155. Sayed F. N., Jain D., Mandal B. P., Pillai C. G. S.and Tyagi A. K., "Tunability of structure from ordered to disordered and its impact on ionic conductivity behavior in the $Nd_{2-y}Ho_yZr_2O_7$ (0.0 [less-than-or-equal] y [less-than-or-equal] 2.0) system" *RSC Advances*, 2 (**2012**) 8341.

156. Sayed F. N., Jain D., Mandal B. P., Pillai C. G. S.and Tyagi A. K., "Tunability of structure from ordered to disordered and its impact on ionic conductivity behavior in the Nd2-yHoyZr2O7 (0.0 [less-than-or-equal] y [less-than-or-equal] 2.0) system" *RSC Advances*, 2 (**2012**) 8341.

157. Sayed F. N., Mandal B. P., Jain D., Pillai C. G. N. S.and Tyagi A. K., "Improved ionic conductivity in $NdGdZr_2O_7$: Influence of Sc^{3+} substitution" *Journal of European Ceramic Society*, 32 (**2012**) 3221.

158. Scheetz B. E.and White W. B., "Characterization of Anion Disorder in Zirconate $A_2B_2O_7$ Compounds by Raman Spectroscopy" *Journal of the American Ceramic Society*, 62 (**1979**) 468.

159. Schwarz K., "Materials design of solid electrolytes" *Proceedings of The National Academy of Sciences of the USA*, 103 (**2006**) 3497.

160. Scott H. G., "Phase relationships in the zirconia-yttria system" *Journal of Materials Science*, 10 (**1975**) 1527.

161. Seifert A., Lange F. F.and Speck J. S., "Epitaxial growth of $PbTiO_3$ thin films on (001) $SrTiO_3$ from solution precursors" *Journal of Materials Research*, 10 (**1995**) 680.

162. Seo D. J., Ryu K. O., Park S. B., Kim K. Y.and Song R.-H., "Synthesis and properties of $Ce_{1-x}Gd_xO_{2-x/2}$ solid solution prepared by flame spray pyrolysis" *Materials Research Bulletin*, 41 (**2006**) 359.

163. Sha X., Lü Z., Huang X., Miao J., Liu Z., Xin X., Zhang Y.and Su W., "Influence of the sintering temperature on electrical property of the $Ce_{0.8}Sm_{0.1}Y_{0.1}O_{1.9}$ electrolyte" *Journal of Alloys and Compounds*, 433 (**2007**) 274.

164. Shannon R., "Revised effective ionic radii and systematic studies of interatomic distances in halides and chalcogenides" *Acta Crystallographica A*, 32 (**1976**) 751.

165. Shannon R., "Revised effective ionic radii and systematic studies of interatomic distances in halides and chalcogenides" *Acta Crystallographica Section A*, 32 (**1976**) 751.

166. Shaula A. L., Kharton V. V.and Marques F. M. B., "Ionic and electronic conductivities, stability and thermal expansion of $La_{10-x}(Si,Al)_6O_{26\pm\delta}$ solid electrolytes" *Solid State Ionics*, 177 (**2006**) 1725.

167. Shimamura K., Arima T., Idemitsu K.and Inagaki Y., "Thermophysical Properties of Rare-Earth-Stabilized Zirconia and Zirconate Pyrochlores as Surrogates for Actinide-Doped Zirconia" *International Journal of Thermophysics*, 28 (**2007**) 1074.

168. Shimonosono T., Hirata Y., Sameshima S.and Horita T., "Electronic Conductivity of La-Doped Ceria Ceramics" *Journal of the American Ceramic Society*, 88 (**2005**) 2114.

169. Shinozaki K., Miyauchi M., Kuroda K., Sakurai O., Mizutani N.and Kato M., "Oxygen-Ion Conduction in the $Sm_2Zr_2O_7$ Pyrochlore Phase" *Journal of the American Ceramic Society*, 62 (**1979**) 538.

170. Shlyakhtina A.and Shcherbakova L., "New solid electrolytes of the pyrochlore family" *Russian Journal of Electrochemistry*, 48 (**2012**) 1.

171. Shlyakhtina A. V., Belov D. A., Knotko A. V., Kolbanev I. V., Streletskii A. N., Karyagina O. K.and Shcherbakova L. G., "Oxygen interstitial and vacancy conduction in symmetric $Ln_{2\pm x}Zr_{2\pm x}O_{7\pm x/2}$ (Ln = Nd, Sm) solid solutions" *Inorganic Materials*, 50 (**2014**) 1035.

172. Sibi K. S., Radhakrishnan A. N., Deepa M., Prabhakar Rao P.and Koshy P., "Oxide ion conductivity and relaxation in $CaREZrNbO_7$ (RE = La, Nd, Sm, Gd, and Y) system" *Solid State Ionics*, 180 (**2009**) 1164.

173. Sinha A., Näfe H., Prakash Sharma B.and Gopalan P., "Study on Ionic and Electronic Transport Properties of Calcium-Doped $GdAlO_3$" *Journal of The Electrochemical Society*, 155 (**2008**) B309.

174. Skinner S. J., "Recent advances in Perovskite-type materials for solid oxide fuel cell cathodes" *International Journal of Inorganic Materials*, 3 (**2001**) 113.

175. Stambouli A. B.and Traversa E., "Solid oxide fuel cells (SOFCs): a review of an environmentally clean and efficient source of energy" *Renewable and Sustainable Energy Reviews*, 6 (**2002**) 433.

176. Steele B. C. H.and Heinzel A., "Materials for fuel-cell technologies" *Nature*, 414 (**2001**) 345.

177. Stevenson J. W., Armstrong T. R., Pederson L. R., Li J., Lewinsohn C. A.and Baskaran S., "Effect of A-site cation nonstoichiometry on the properties of doped lanthanum gallate" *Solid State Ionics*, 113–115 (**1998**) 571.

178. Subramanian M. A., Aravamudan G.and Subba Rao G. V., "Oxide Pyrochlores - A Review" *Progress in Solid State Chemistry*, 15 (**1983**) 55.

179. Subramanian M. A., Aravamudan G.and Subba Rao G. V., "Oxide Pyrochlores - A Review" *Progress in Solid State Chemistry*, 15 (**1983**) 55.

180. Suda E., Pacaud B.and Mori M., "Sintering characteristics, electrical conductivity and thermal properties of La-doped ceria powders" *Journal of Alloys and Compounds*, 408–412 (**2006**) 1161.

181. Sumaletha Narayanan V. T., "Effect of Y substitution for Nb in $Li_5La_3Nb_2O_{12}$ on Li ion conductivity of garnet-type solid electrolytes" *Journal of Power Sources*, 196 (**2011**) 8085.

182. Takahashi T., Iwahara H.and Nagai Y., "High oxide ion conduction in sintered Bi_2O_3 containing SrO, CaO or La_2O_3" *Journal of Applied Electrochemistry*, 2 (**1972**) 97.

183. Tao S.and Irvine J. T. S., "A redox-stable efficient anode for solid-oxide fuel cells" *Nature Materials*, 2 (**2003**) 320.

184. Tealdi C., Malavasi L., Ritter C., Flor G.and Costa G., "Lattice effects in cubic $La_2Mo_2O_9$: Effect of vacuum and correlation with transport properties" *Journal of Solid State Chemistry*, 181 (**2008**) 603.

185. Thampi V., Padala P. R.and Radhakrishnan A. N., "Induced oxygen vacancies and their effect on the structural and electrical properties of a fluorite-type $CaZrO_3$-$Gd_2Zr_2O_7$ system" *New Journal of Chemistry*, 39 (**2015**) 1469.

186. Thornber M. R., Bevan D. J. M.and Summerville E., "Mixed oxides of the type MO_2(fluorite)-M_2O_3. V. Phase studies in the systems ZrO_2-M_2O_3 (M = Sc, Yb, Er, Dy)" *Journal of Solid State Chemistry*, 1 (**1970**) 545.

187. Torrens R., Sammes N. M.and Tompsett G., "Characterization of Pr- and Sm-Doped $Ce_{0.8}Gd_{0.2}O_{2-\delta}$" *Journal of Electroceramics*, 13 (**2004**) 683.

188. Tuller H. L., "Mixed ionic-electronic conduction in a number of fluorite and pyrochlore compounds" *Solid State Ionics*, 52 (**1992**) 135.

189. Vaisakhan Thampi D. S., Prabhakar Rao P.and Radhakrishnan A. N., "Influence of Ce substitution on the order-to-disorder structural transition, thermal expansion and electrical properties in $Sm_2Zr_{2-x}Ce_xO_7$ system" *RSC Advances*, 4 (**2014**) 12321.

190. van Dijk M. P., Burggraaf A. J., Cormack A. N.and Catlow C. R. A., "Defect structures and migration mechanisms in oxide pyrochlores" *Solid State Ionics*, 17 (**1985**) 159.

191. van Dijk M. P., de Vries K. J.and Burggraaf A. J., "Oxygen ion and mixed conductivity in compounds with the fluorite and pyrochlore structure" *Solid State Ionics*, 9–10, Part 2 (**1983**) 913.

192. Vandenborre M. T., Husson E., Chatry J. P.and Michel D., "Rare-earth titanates and stannates of pyrochlore structure; vibrational spectra and force fields" *Journal of Raman Spectroscopy*, 14 (**1983**) 63.

193. Vegard L., "Die Konstitution der Mischkristalle und die Raumfüllung der Atome" *Zeitschrift für Physik*, 5 (**1921**) 17.

194. Wan C., Qu Z., Du A.and Pan W., "Order–Disorder Transition and Unconventional Thermal Conductivities of the $(Sm_{1-x}Yb_x)_2Zr_2O_7$ Series" *Journal of the American Ceramic Society*, 94 (**2011**) 592.

195. Wang J.-X., Li L.-P., Campbell B. J., Lv Z., Ji Y., Xue Y.-F.and Su W.-H., "Structure, thermal expansion and transport properties of BaCe1−xEuxO3−δ oxides" *Materials Chemistry and Physics*, 86 (**2004**) 150.

196. Wang J., Nakamura A.and Takeda M., "Structural properties of the fluorite- and pyrochlore-type compounds in the Gd_2O_3–ZrO_2 system $xGdO_{1.5}$–$(1-x)ZrO_2$ with $0.18 \leq x \leq 0.62$" *Solid State Ionics*, 164 (**2003**) 185.

197. Wang X. P., Cheng Z. J.and Fang Q. F., "Influence of potassium doping on the oxygen-ion diffusion and ionic conduction in the La2Mo2O9 oxide-ion conductors" *Solid State Ionics*, 176 (**2005**) 761.

198. Weller M., Khelfaoui F., Kilo M., Taylor M. A., Argirusis C.and Borchardt G., "Defects and phase transitions in yttria- and scandia-doped zirconia" *Solid State Ionics*, 175 (**2004**) 329.

199. West A. R., "Solid State Chemistry and its Applications" Wiley India, (**1984**).

200. Wilde P. J.and Catlow C. R. A., "Defects and diffusion in pyrochlore structured oxides" *Solid State Ionics*, 112 (**1998**) 173.

201. Wu C. K. A. M. D. F. K. S. N. A. K. C. S. M. Y. X. J., "X-ray diffraction measurements of the c-axis Debye-Waller factors of $YBa_2Cu_3O_7$ and $HgBa_2CaCu_2O_6$" *Physical Review B*, 67 (**2003**) 092508.

202. Wuensch B. J., Eberman K. W., Heremans C., Ku E. M., Onnerud P., Yeo E. M. E., Haile S. M., Stalick J. K.and Jorgensen J. D., "Connection between oxygen-ion conductivity of pyrochlore fuel-cell materials and structural change with composition and temperature" *Solid State Ionics*, 129 (**2000**) 111.

203. Xia X.-L., Gao S., Liu Z.-G.and Ouyang J.-H., "The influence of pentavalent Nb substitution for Zr on electrical property of oxide-ion conductor Gd2Zr2O7" *Electrochimica Acta*, 55 (**2010**) 5301.

204. Xia X.-L., Liu Z.-G., Ouyang J.-H., Gao S.and Liu X.-M., "Effect of Ce substitution for Zr on electrical property of fluorite-type Gd2Zr2O7" *Solid State Sciences*, 13 (**2011**) 1328.

205. Xia X.-L., Ouyang J.-H.and Liu Z.-G., "Influence of CaO on structure and electrical conductivity of pyrochlore-type $Sm_2Zr_2O_7$" *Journal of Power Sources*, 189 (**2009**) 888.

206. Xia X.-L., Ouyang J.-H.and Liu Z.-G., "Influence of CaO on structure and electrical conductivity of pyrochlore-type $Sm_2Zr_2O_7$" *Journal of Power Sources*, 189 (**2009**) 888.

207. Xia X.-L., Ouyang J.-H.and Liu Z.-G., "Electrical Properties of Gadolinium–Europium Zirconate Ceramics" *Journal of American Ceramic Society*, 93 (**2010**) 1074.

208. Xia X. L., Liu Z. G., Ouyang J. H.and Zheng Y., "Preparation, Structural Characterization, and Enhanced Electrical Conductivity of Pyrochlore-type $(Sm_{1-x}Eu_x)_2Zr_2O_7$ Ceramics" *Fuel Cells*, 12 (**2012**) 624.

209. Xiao-Liang Xia J.-H. O., Zhan-Guo Liu, and Sa Li, "Effect of MgO on the Electrical Conductivity of the Pyrochlore-Type $Sm_2Zr_2O_7$" *Science of Advanced Materials*, 2 (**2010**) 497.

210. Yahiro H., Eguchi K.and Arai H., "Electrical properties and reducibilities of ceria-rare earth oxide systems and their application to solid oxide fuel cell" *Solid State Ionics*, 36 (**1989**) 71.

211. Yamamoto O., Arati Y., Takeda Y., Imanishi N., Mizutani Y., Kawai M.and Nakamura Y., "Electrical conductivity of stabilized zirconia with ytterbia and scandia" *Solid State Ionics*, 79 (**1995**) 137.

212. Yamamura H., Nishino H., Kakinuma K.and Nomura K., "Crystal Phase and Electrical Conductivity in the Pyrochlore-Type Composition Systems, $Ln_2Ce_2O_7$ (Ln=La, Nd, Sm, Eu, Gd, Y and Yb)" *Journal of the Ceramic Society of Japan*, 111 (**2003**) 902.

213. Yaremchenko A. A., Kharton V. V., Naumovich E. N., Shestakov D. I., Chukharev V. F., Kovalevsky A. V., Shaula A. L., Patrakeev M. V., Frade J. R.and Marques F. M. B., "Mixed conductivity, stability and thermomechanical properties of Ni-doped $La(Ga,Mg)O_{3-\delta}$" *Solid State Ionics*, 177 (**2006**) 549.

214. Yashiro K., Suzuki T., Kaimai A., Matsumoto H., Nigara Y., Kawada T., Mizusaki J., Sfeir J.and Van herle J., "Electrical properties and defect structure of niobia-doped ceria" *Solid State Ionics*, 175 (**2004**) 341.

215. Yasuda I., Matsuzaki Y., Yamakawa T.and Koyama T., "Electrical conductivity and mechanical properties of alumina-dispersed doped lanthanum gallates" *Solid State Ionics*, 135 (**2000**) 381.

216. Yoshida H.and Inagaki T., "Effects of additives on the sintering properties of samaria-doped ceria" *Journal of Alloys and Compounds*, 408–412 (**2006**) 632.

217. Zhan-Guo L., Jia-Hu O., Yu Z.and Xiao-Liang X., "Preparation and microstructural characterization of $(Nd_{1-x}Gd_x)_2(Ce_{1-x}Zr_x)_2O_7$ solid solutions" *Ceramics International*, 35 (**2009**) 2387.

218. Zhang F. X., Lian J., Becker U., Ewing R. C., Hu J.and Saxena S. K., "High-pressure structural changes in the $Gd_2Zr_2O_7$ pyrochlore" *Physical Review B*, 76 (**2007**) 214104.

219. Zhang F. X., Manoun B.and Saxena S. K., "Pressure-induced order–disorder transitions in pyrochlore $RE_2Ti_2O_7$ (RE=Y, Gd)" *Materials Letters*, 60 (**2006**) 2773.

220. Zhang F. X., Manoun B., Saxena S. K.and Zha C. S., "Structure change of pyrochlore $Sm_2Ti_2O_7$ at high pressures" *Applied Physics Letters*, 86 (**2005**) 181906.

221. Zhou N., Chen G., Zhang H. J.and Zhou C., "Synthesis and transport properties of La_2NiO_4" *Physica B: Condensed Matter*, 404 (**2009**) 4150.